

NASA Contractor Report 4147

Turbofan Forced Mixer Lobe Flow Modeling

I—Experimental and Analytical Assessment

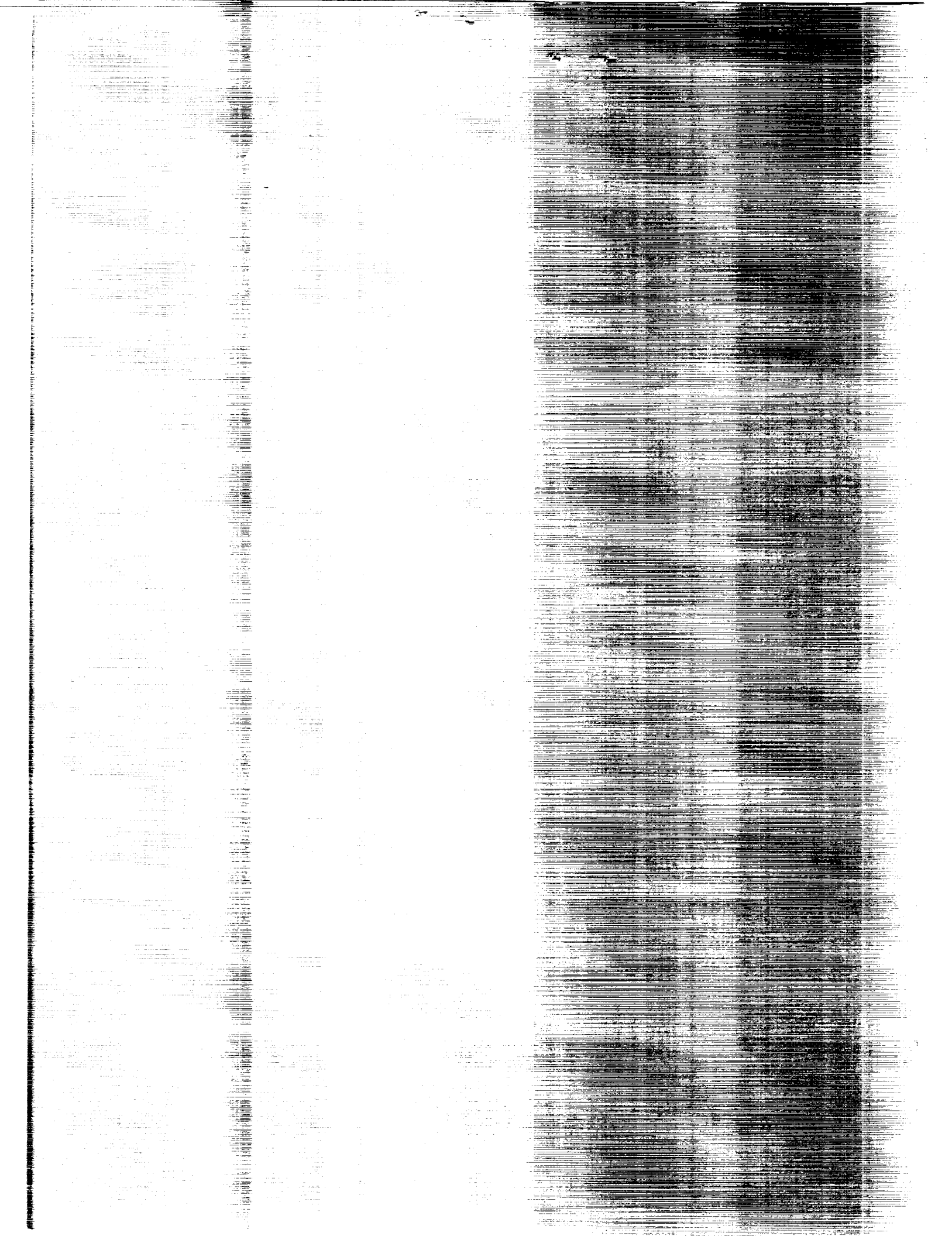
T. Barber, R. W. Paterson,
and S. A. Skebe

CONTRACT NAS3-23039
OCTOBER 1988

(NASA-CR-4147-1) TURBOFAN FORCED MIXER
LOBE FLOW MODELING. 1: EXPERIMENTAL AND
ANALYTICAL ASSESSMENT Final Report (Pratt
and Whitney Aircraft) 155 p CSCL 01A

NO 4-147-1

H1/02 Unclass
0183673



NASA Contractor Report 4147

Turbofan Forced Mixer Lobe Flow Modeling

I—Experimental and Analytical Assessment

T. Barber, R. W. Paterson,
and S. A. Skebe
*United Technologies Corporation
Pratt & Whitney Engineering Division
East Hartford, Connecticut*

Prepared for
Lewis Research Center
under Contract NAS3-23039



National Aeronautics
and Space Administration

Scientific and Technical
Information Division

1988



FOREWORD

The overall objective of this NASA program has been to develop and implement several computer programs suitable for the design of lobe forced mixer nozzles. The analyses are based on linear or small disturbance formulations. The analyses were applied to several mixer lobe shapes to predict the downstream vorticity generated by different lobe shapes. Data was taken in a simplified planar mixer model tunnel to calibrate and evaluate the analysis. Any discrepancies between measured secondary flows emanating downstream of the lobes and predicted vorticity by the analysis is fully reviewed and explained. The lobe analysis are combined with an existing 3D viscous calculation to help assess and explain measured lobed data.

The program also investigated technology required to design forced mixer geometries for augmentor engines that can provide for performance requirements of future strategic aircraft. For this purpose, available mixer design correlations were used to design several preliminary mixer concepts for application in a exhaust system. Based on preliminary performance estimates, two mixer configurations were selected for further testing and analysis.

The results of the program are summarized in three volumes, all under the global title, "Turbofan Forced Mixer Lobe Flow Modeling". The first volume is entitled "Part I - Experimental and Analytical Assessment" summarizes the basic analysis and experimental results as well as focuses on the physics of the lobe flow field construed from each phase. The second volume is entitled "Part II - Three Dimensional Inviscid Mixer Analysis (FLOMIX)". The third and last volume is entitled "Part III - Application to Augmentor Engines".

PRECEDING PAGE BLANK NOT FILMED

ACKNOWLEDGEMENT

The authors wish to acknowledge helpful discussions with Allan Bishop (NASA), Walter M. Presz, Jr. (Western New England College) and Michael J. Werle (UTRC) relative to the formulation and conduct of the study. Earl M. Murman (MIT) and George L. Muller (P&W) provided guidance and assistance in the formulation of the analytical and numerical FLOWMIX procedure. Roy K. Amiet (UTRC) developed the planar analysis, PLANMIX. Appreciation is also expressed to Olof L. Anderson (UTRC), Steve Zysman (P&W) and Bruce L. Morin (UTRC) for analytical and experimental assistance, respectively, Edward M. Greitzer (MIT) for reviewing the report and Thomas A. Wynosky who served as the Pratt & Whitney Program Manager.

TABLE OF CONTENTS

SECTION	TITLE	Page
	FOREWORD	iii
	ACKNOWLEDGMENT	iv
	NOMENCLATURE	vii
I.	SUMMARY	1
II.	INTRODUCTION	3
III.	FORCED MIXER ANALYSIS	7
	A. General Concepts	7
	B. Planar Analysis	10
	C. Axisymmetric Analysis	11
	D. Applications	14
IV.	DESCRIPTION OF EXPERIMENT	29
	A. Experimental Arrangement	29
	1. Mixer Lobe Cascade Facility	29
	2. Mixer Lobe Models	30
	B. Instrumentation	36
	1. Laser Doppler Velocimetry	36
	2. Total and Static Pressures	38
	3. Flow Visualization	39
	4. Boundary Layer Definition	39
	5. Experimental Technique	39
	5. Data Analysis	42
V.	RESULTS AND DISCUSSION	44
	A. Experimental Observations	44
	1. Data Presentation	44
	2. General Observations	45
	3. Mixer Lobe Flow Visualization	46
	4. Approximate Analysis	51
	5. Low Penetration Sinusoidal Mixer	52
	6. High Penetration Sinusoidal Mixer	62
	7. Advanced High Penetration Mixer	73
	B. Mixer Flow Analysis	86
	C. Mixer Flow Field Model	92
	1. Circulations Calculations	92
	2. Circulation and Mixing	97
VI.	SUMMARY OF RESULTS	99
VII.	CONCLUSIONS	101
	REFERENCES	103

TABLE OF CONTENTS (Continued)

SECTION	TITLE	Page
	APPENDICES	105
A.	Viscous Marching Analysis	106
B.	Lobed Mixer Coordinates	109
C.	Code Input Files	113
D.	Data Bases	116
E.	Approximate Analysis	143

NOMENCLATURE

C_p	Pressure coefficient
P	Static pressure
P_e	Penetration, $A_{p_{rim}}/A_{duct}$
h	Half height or amplitude of mixer lobe
L	Half span width or half wave/length of mixer lobe
L_m	Length of mixer from cross-over to exit plane
R_m	Mean radius of mixer lobe
U	Free stream velocity component in axial direction
U_{REF}	Axial velocity at lobe exit
u	Perturbation velocity component in axial direction
v	Perturbation velocity component in transverse direction
w	Perturbation velocity component in spanwise direction
x, y, z	Axial, transverse, spanwise Cartesian coordinates
x, r, θ	Cylindrical Cartesian coordinates
X	Mixer width

ω	Mixer lobe frequency
β^2	Compressibility factor
Γ	Circulation at lobe trailing edge
ϵ	Lobe geometrical turning angle, $\tan^{-1}(h/L_m)$
θ	Spanwise or azimuthal angle
λ_k	kth Fourier component of lobe surface
ϕ	Perturbation velocity potential

Subscripts

o	Total or stagnation property
∞	Free stream property

I. SUMMARY

This report describes a joint analytical and experimental investigation of three-dimensional flowfield development within the lobe region of turbofan forced mixer nozzles. The study represents a continuation of an effort initiated by NASA and UTRC in 1977 to develop computational procedures for predicting forced mixer nozzle mixing characteristics, thereby providing an alternative to the empirical testing approach characteristic of the mixer development process. The initial phase of that effort demonstrated that axial vortex fields established at the lobe exit were responsible for the rapid mixing observed in such nozzles and that when this secondary flow circulation was used as a starting condition at the lobe exit plane, downstream nozzle mixing could be predicted accurately. The objective of the current study was to develop an analytical and experimental method for predicting the lobe exit flowfield, thereby providing, in conjunction with the mixing analysis, the capability to compute engine flows from mixer nozzle inlet to exit.

In the present analytical approach, a linearized inviscid aerodynamic theory was used for representing the axial and secondary flows within the three-dimensional convoluted mixer lobes and three-dimensional boundary layer analysis was applied thereafter to account for viscous effects. The experimental phase of the program employed three planar mixer lobe models having different waveform shapes and lobe heights for which detailed measurements were made of the three-dimensional velocity field and total

pressure field at the lobe exit plane. Velocity data was obtained using Laser Doppler Velocimetry (LDV) and total pressure probing and hot wire anemometry were employed to define exit plane total pressure and boundary layer development. Comparison of data and analysis was performed to assess analytical model prediction accuracy.

As a result of this study both a planar mixer geometry inverse analysis (PLANMIX) and a more general (planar or axisymmetric) direct analysis have been developed. Exit plane circulation and boundary layer characteristics, computed from these codes and the three-dimensional boundary layer analysis, were shown to compare favorably with experimental results. Additional analysis was performed to identify the primary non-dimensional parameters which influence the strength of the axial vortices shed from the lobe trailing edge. A principal conclusion resulting from this study is that the global mixer lobe flowfield is inviscid and can be predicted from an inviscid analysis and Kutta condition.

II. INTRODUCTION

The overall research problem addressed in this study was the development of an analytical method for predicting three-dimensional flow development within the convoluted lobes of forced mixer nozzles installed in modern commercial turbofan engines. The design of these forced mixer lobes has been traditionally accomplished by using experimental correlations to relate mixer performance to a variety of geometrical parameters. This process is typically an iterative one, relying heavily on experimental verification. While this process has been reasonably successful, little insight has been gained as to the driving flow mechanisms involved and how to design the lobe surfaces so as to optimize the mixing process. The formulation of an analytical procedure is critical to the development of improved mixer designs for use in such engines and in the numerous additional applications of mixers which have been recently identified.

Turbofan engine mixer technology is well established as a means for reducing aircraft jet noise while at the same time achieving a measurable thrust improvement. In addition to reducing noise by rapidly mixing out the high axial velocity primary stream fluid with the lower velocity secondary stream, the mixer reduces peak nozzle exit plane temperature, which is an important consideration for certain engine applications. Recent research (Ref. 1) conducted at Western New England College and UTRC under NASA sponsorship has shown mixer lobes can dramatically improve the performance of ejectors such as

suggested for use in advanced exhaust systems. Other applications of mixer lobe axial vorticity flow control have been also identified (Ref. 2,3). These involve airfoil stall and separation alleviation. Initial efforts at analytically investigating the flow in mixer nozzles were performed in conjunction with "benchmark" experiments (Ref. 4,5) that obtained a detailed description of the flow within a model turbofan forced mixer nozzle. Laser Doppler Velocimetry (LDV) was employed to define the three-dimensional velocity field between the lobe exit plane and the nozzle exit. These experiments have determined that the mixing process is dominated by the secondary flow generated within the lobe region of the flow. Anderson et al. (Ref. 6,7) have proposed several sources for the secondary flow and lumped them together under a "generic" vorticity label. This vorticity source has been analytically simulated in a viscous marching analysis and has reproduced the observed flow mixing patterns and magnitudes.

Whereas previous research studies conducted at UTRC and NASA Lewis Research Center have shown that three-dimensional viscous computational procedures can be employed to calculate the nozzle mixing downstream of the mixer lobe exit plane, no analytical method existed at the outset of the present study for predicting the lobe exit plane flow field. Furthermore, these prior studies showed that the success of the mixing calculation in predicting the experimental nozzle mixing data was critically dependent upon the correct definition of the secondary flow circulation existing at the exit of each mixer lobe segment. Similar studies were conducted during the present program using the PEPsi-M Parabolized Navier Stokes code and applying it to the data

cited in reference 2. These results substantiate the earlier results of other researchers and indicate the magnitude of the secondary flow induced circulation field is directly related to the lobe shape. The highlights of this study are presented in Appendix A. As a result of this research, it was clear that the major problem remaining in the construction of an overall prediction and design analysis system for turbofan engine forced mixers was the prediction of the flow field development within the three-dimensional convoluted lobes.

The outstanding issues to be resolved in this research program were: how is the secondary flow field generated over the lobe surface, is this process also largely inviscidly dominated and can a simplified analytical procedure be constructed to predict the lobe exit plane flow field for a wide class of convoluted geometries? This report, as Part I of a three part series, addresses these issues by developing an inviscid numerical procedure for predicting the flow over the lobe and thereby generating the necessary exit plane secondary flowfield. The accuracy of the analytical model is then assessed with benchmark data bases generated in the present program for selected mixer geometries. A specific focus of this study was to use information gained from the joint analytical and experimental research to design an advanced configuration which produces higher levels of axial vorticity and circulation. Testing of this configuration and corresponding code predictions assisted in the formulation of recommendations relative to future research directions in the area of mixer technology. Finally, this report constructs a model of the flow mechanism within the lobe region and in the interface region between the lobe and the downstream mixing duct.

The approach was a combined analytical and experimental effort. The analytical approaches developed herein are based on linear inviscid theory. Two computer codes, PLANMIX and FLOMIX, were developed. The viscous flow development over the lobes was then determined using an ex post facto three-dimensional boundary layer analysis. Lobe testing was also conducted to investigate the lobe flow field and to provide data for assessing the analyses. An experimental data base was generated; LDV techniques defined the three-dimensional velocity field and pitot probes defined total pressure distributions at the lobe exit plane. Lobe circulation levels and exit plane boundary layer characteristics were developed from this data. An approximate analysis was developed for identifying scaling parameters for lobe circulation and to assess waveform geometry effects on circulation.

The major conclusion of this study is that the linear inviscid analyses are able to predict the lobe exit plane circulation with the coupled boundary layer analysis, thereby predicting the shear layer development on the lobe surface. For the three specific lobe models tested, these predictions were found to be in reasonable agreement with experiment. Additional analyses identified the primary parameter affecting the exit plane circulation for straight-ramped lobes as the ratio of the lobe amplitude squared to lobe length. From this result, it is concluded that the steepest ramp angle that can be achieved without separation maximizes the induced circulation. Furthermore, it was also concluded from studying the effect of mixer waveform on circulation that parallel-sided configurations are inherently superior to nonparallel configurations such as sinusoidal or triangular. Experimental data

confirmed these predictions regarding both lobe amplitude and waveform. It was found that mixer lobe performance can be adversely affected by boundary layer buildup in the interior peak or trough region of the lobes, thereby reducing their effective lobe amplitude and consequently the circulation shed into the wake.

The analytical and experimental phases of this study have resulted in an improved understanding of the mechanisms driving the lobe flowfield and has produced a validated code for integration into an overall mixer nozzle design analysis.

III. FORCED MIXER ANALYSIS

A. General Concepts

The development of an analysis to predict the flow over a mixer lobe is inherently an extremely complex problem. The flow field is fully three-dimensional, may have different energy levels between the mixing streams and can be dominated by viscous dissipation effects. A complete numerical solution of the Navier-Stokes equations still represents a major challenge, both in grid generation and in resolving the thin shear layers over the lobe surface. A more tractable approach, however, considers a zonal treatment, wherein local regions are analyzed using simplified procedures. The analytical approach pursued in this study has been built on the results of Anderson et al. by exploring the source of "generic" vorticity and modeling it within the

basic conservation laws. The "flap" vorticity concept, schematically shown in Figure 1, models the lobe as a periodic system of cambered airfoils. Applying to each airfoil a Kutta condition at the trailing edge determines the inviscid lift distribution and sets up the observed trailing edge secondary flow field. The effects of viscosity are then accounted for using an ex post facto three-dimensional boundary layer analysis.

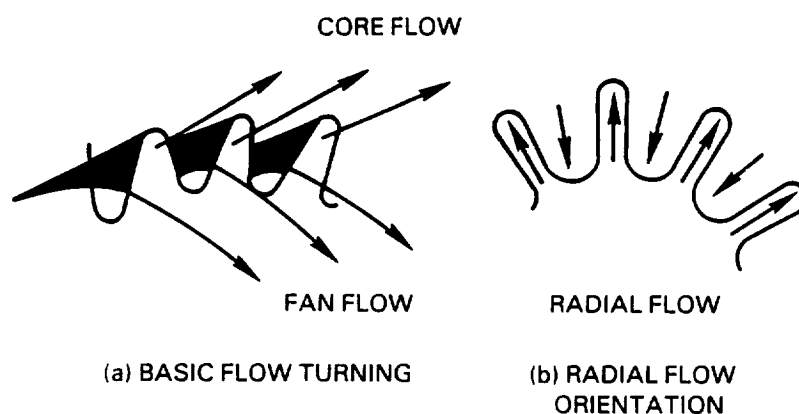
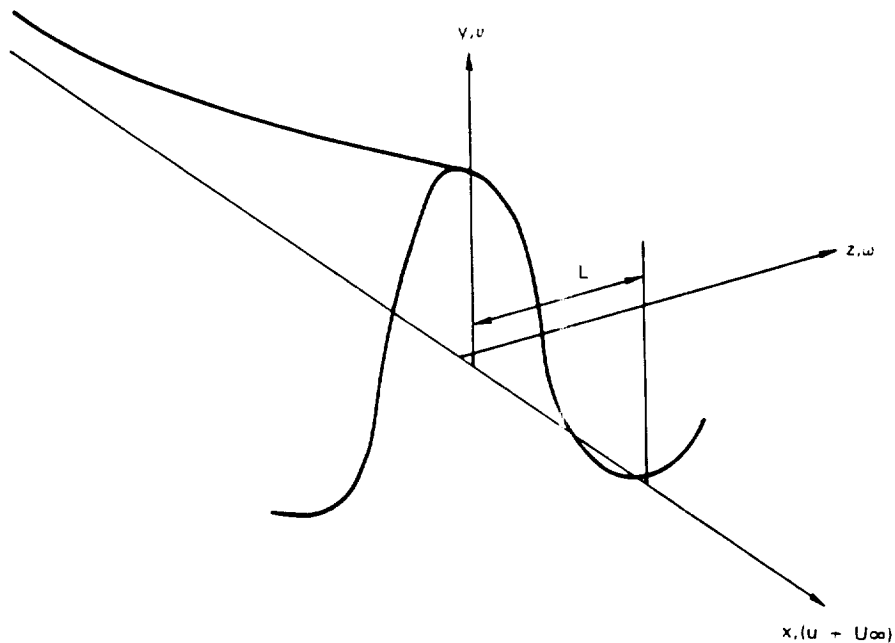


Figure 1 Secondary Flow Generation, Turning (Flap) Vorticity Model

Two different inviscid analytical approaches have been formulated and used in this study. Each procedure assumes the local flow to be irrotational and both apply local linearizations to simplify application of the tangency boundary condition from the convoluted mixer lobe surface to some mean surface representation. The first is a planar indirect analysis called PLANMIX that uncouples the spanwise dependence by assuming a sinusoidal waveform lobe shape. The latter analysis is a planar and axisymmetric direct analysis called FLOMIX which is capable of treating arbitrary lobe geometries and mixing of streams with unequal total pressures and total temperatures. The simpler PLANMIX code was used to validate the more complex FLOMIX code. Complete

documentation of each analysis can be found in References 8-11, but a brief description is provided below. Specific applications of the programs are also presented and these configurations are subsequently examined in the experimental portion of this document.

In the following design, analysis and data sections of this report, an (x,y,z) Cartesian coordinate system oriented with the x axis in the primary flow direction, the y axis in the transverse or vertical direction and the z axis in the spanwise or lateral direction. The coordinate origin is centered along the lobe crest ($z=0$) and vertically at the half height ($y=0$). All coordinates have been normalized by L , the lobe half-wave length. The corresponding velocity components are $(u + U_\infty)$, v , w where u , v , w are velocity perturbation components from the free stream flow. The velocity components, as presently in the text, will be normalized by the free stream velocity U_∞ .



A. Planar Analysis

The planar potential analysis (Ref. 8), called PLANMIX, is an inverse procedure constructed to assist in the design of idealized lobes for a planar low speed test facility. The analysis assumes the flow is both incompressible and irrotational. A flow solution in terms of the velocity potential can be determined from Laplace's equation. The PLANMIX analysis idealizes the mixer lobe by unwrapping it so that the planform forms a corrugated flat plate in the $y=0$ plane. The linearization assumption furthermore implies that the lobe height is small compared to all other length scales in the problem.

In the present case, a further restriction is imposed by assuming the lobe surface is a sinusoidal cross-sectional shape, thereby removing the spanwise indeterminacy. Solutions to Laplace's equation can always be obtained from superposition of singularities, i.e., point sources (monopoles), doublets, vortices. For an incompressible flow, a doublet distribution of specified strength along the flat plate will uniquely define the lobe height and therefore its shape. The surface height of a lobe $h(x,z)$ can be determined from the following expression:

$$h(x,z) = \cos(\alpha z) \int_{-\infty}^x \frac{v(\xi, 0, 0)}{U_\infty} d\xi \quad (1)$$

where v_s is the transverse component of the perturbation velocity defined in terms of the dipole loading function

$$f(x) = R (P |Lm-x|)^{1/2} \exp(-P |Lm-x|) \quad (2)$$

α is the frequency of the mixer lobe, U_∞ is the free stream velocity, x and z are the axial and spanwise distance, respectively, P , the axial scaling length and R , the loading amplitude. Because of the linearity of the problem, proportional increases in R result in a proportionally higher mixer lobe. The choice of loading function is somewhat arbitrary, however, its strength was chosen to be zero at the lobe trailing edge ($x=0$.) to satisfy the Kutta condition. The loading function choice was based on linear airfoil theory and exhibits the expected square root decay.

C. Axisymmetric Analysis

In contrast to the above planar inverse analysis, the FLOMIX axisymmetric analysis (Ref. 9-11) solves for the flow over a given lobe contour. It also removes many of the geometrical and flow modeling restrictions previously imposed in order to more closely model the actual environment of a forced mixer found in current generation gas turbine installations. More specifically, the mixer lobe geometry is not limited to sinusoidal cross-sections, the lobe flow field analysis includes the effects of the adjacent centerbody and fan nozzle walls shown in Figure 2, and the effects of power addition and compressibility are also simulated. A potential flow model is still applicable if the inlet flows can be considered as two separate irrotational regions divided by a vortex sheet. In such an analysis, the wake must be dynamically tracked and two separate velocity potentials considered.

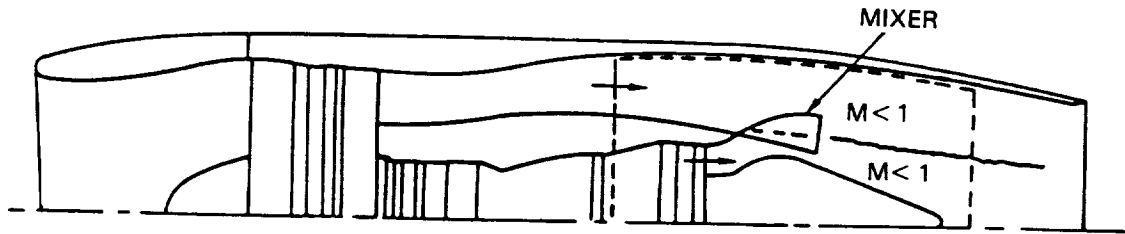


Figure 2 Schematic Cutaway View of Forced Mixer Installation in a Turbofan Engine

The FLOMIX is a control volume analysis developed in cylindrical Cartesian coordinates, aligned to the engine centerline. A novel procedure is followed by solving the flux balanced equations by locating the intersections of the geometry with the regular rectangular mesh. This procedure is schematically shown in Figure 3. Small disturbance approximations are applied to linearize compressibility effects, i.e., the mass flux vector is approximated by:

$$\bar{\rho} \bar{v} = \left(1. + \beta^2 \frac{\phi}{x} \right) \bar{i}_x + \frac{\phi}{r} \bar{i}_r + \frac{1}{r} \phi_\theta \bar{i}_\theta \quad (3a)$$

$$\beta^2 = 1. - M_\infty^2 \quad , \quad (3b)$$

and the convoluted lobe surface is approximated by an axisymmetric surface of mean radius $R_m(x)$. This latter linearization permits one to uncouple the spanwise dependence (θ) through a Fourier modal analysis

$$\phi(x, r, \theta) = \sum_{k=1}^{NH} g_k(x, r) h_k(\theta) \quad (4)$$

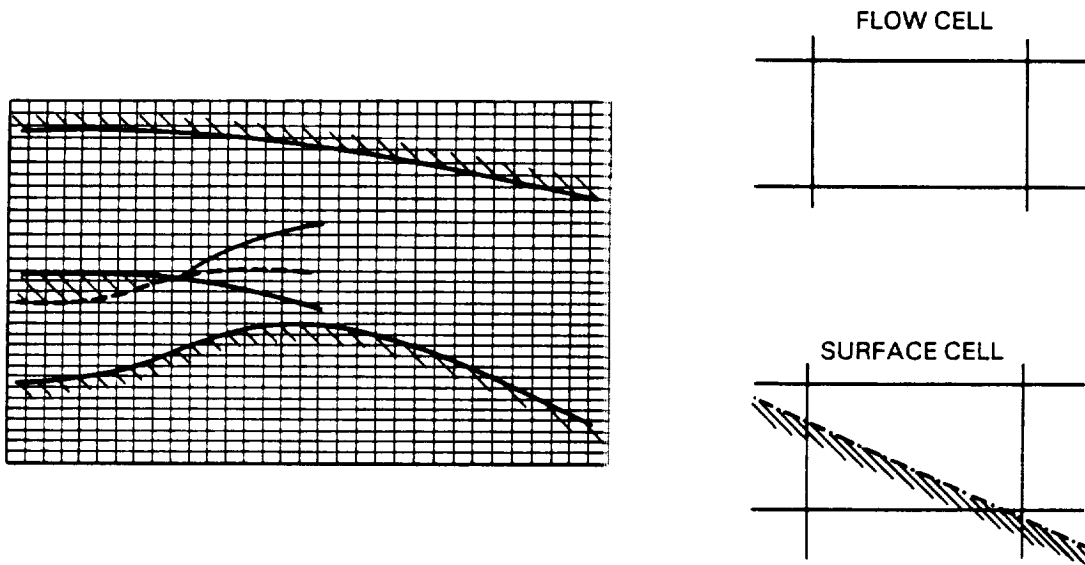


Figure 3 Mixer Geometry Definition on a Cylindrical Cartesian Mesh

The solution is now determined in terms of several axisymmetric potentials $g_k(x,r)$ with a Kutta condition and a flow tangency boundary condition imposed for each k th mode. The tangency condition can be shown to be equivalent to an effective flux condition applied on the mean surface $R_m(x)$

$$g_{r,k}(x,R_m) = \lambda'_k(x) + \frac{1}{2R_m} \sum_j \sum_n \lambda_n(x) g_j(x,r) [(\delta c) - \delta c] \quad (5)$$

where λ_n , λ'_k are the modal shapes and slopes of the various Fourier modes of the mixer lobe. The leading term in Eq. (5) is the classical two-dimensional contribution, while the latter term is the three-dimensional spanwise term that couples the individual (k) modes. The orientation of λ and R_m are schematically shown in Figure 4. Complete details regarding the solution procedure can be found in (Ref. 9).

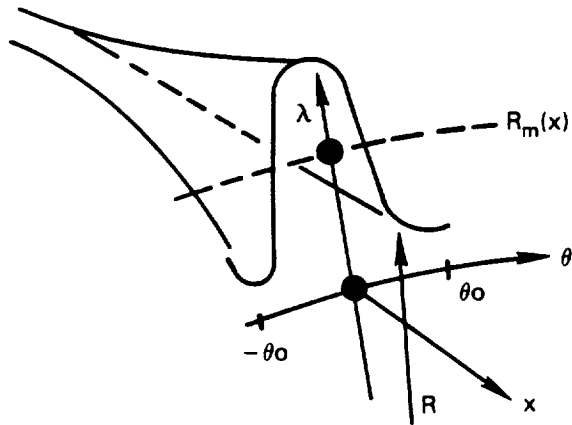


Figure 4 Definition of Lobe Geometrical Parameters for Fourier Analysis

D. Applications

The PLANMIX inverse analysis was used to generate coordinates for two mixer lobe configurations: one, a low penetration design that was consistent with the linearization assumptions used in the analysis and the second, a high penetration design chosen to examine the limits of the model's applicability.

In this case reference to lobe penetration refers to the degree of projection of the core or inner flow into the bypass or outer stream. In classical mixer terminology, this would be termed the flow turning (h/L_m), rather than the penetration Pe which is an area ratio parameter. The code geometrical parameters for the low and high penetration sinusoidal lobes are given below and a side view of both is given in Figure 5.

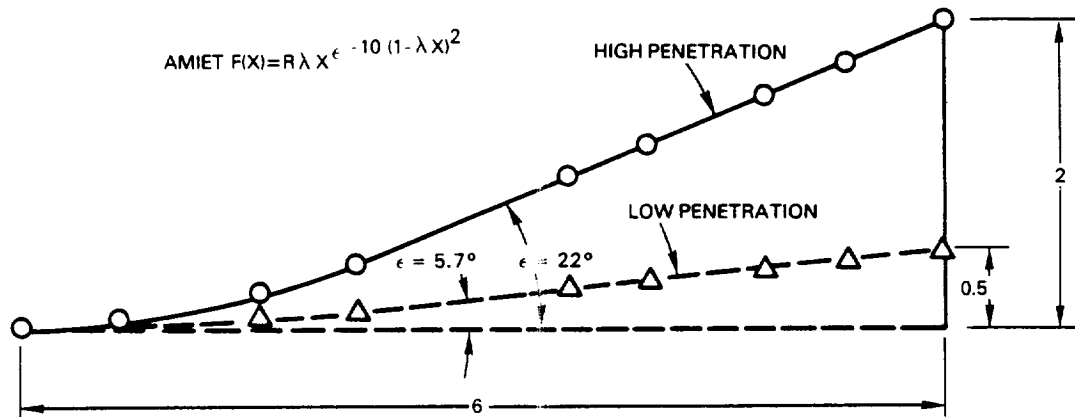


Figure 5 NASA Sinusoidal Mixer Cascade Designs 1 and 2

A complete tabulation of their coordinates is given in Appendix B. A plot of the solutions for these mixer lobes, expressed in terms of axial distribution of the linearized pressure coefficient ($C_{pL} = -2u/U_\infty$), is shown in Figures 6(a) and 6(b). The axial pressure gradient is produced by the surface curvature at the break from the planar surface. The return to free stream, $C_{pL}=0.0$, is driven by the trailing edge Kutta condition. The spanwise gradient inviscidly drives the flow from the crest ($\theta' = 0.$) to the trough ($\theta' = 1.0$), where θ' is the reduced spanwise coordinate $\theta' = z / L = \theta/\theta_0$. If the flow solution was displayed in terms of the actual C_p , the lower order contributions of v and w would result in a nonzero value of C_p at the lobe trailing edge.

	Low Penetration Lobe	High Penetration Lobe
h/L_m	0.1	0.4
h	0.500	2.000
P	0.215	0.215
α	π	π
R	0.02209	$0.8839 = 4 (.02209)$

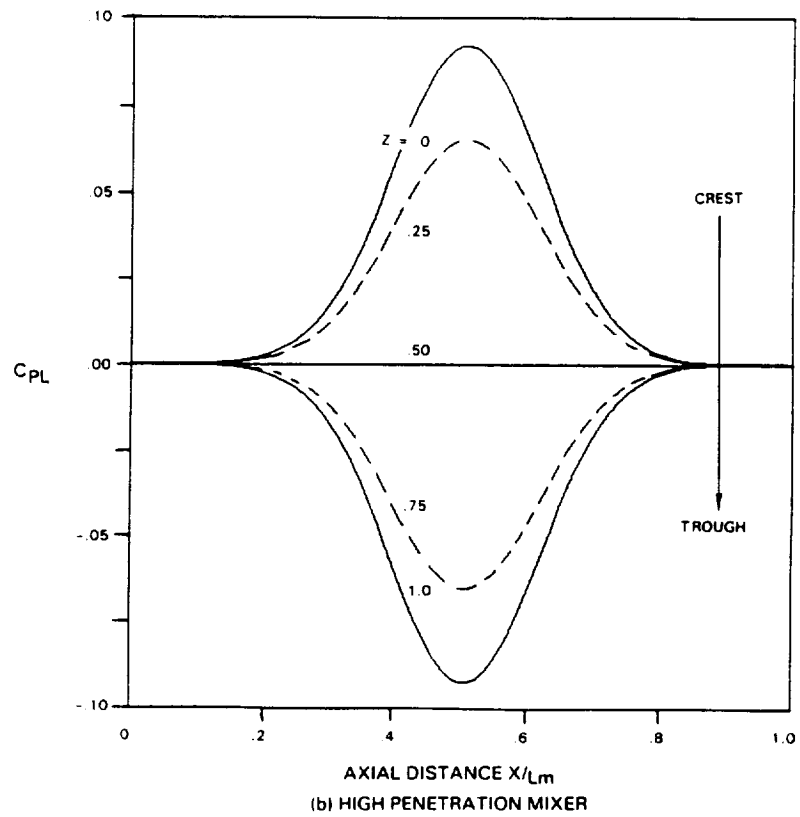
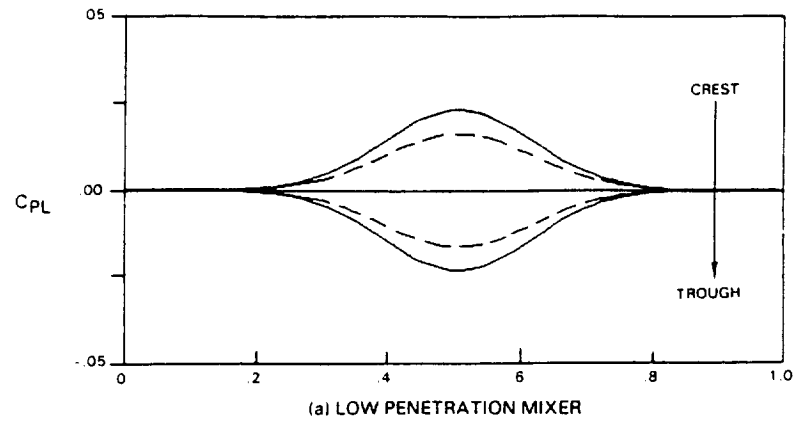


Figure 6 PLANMIX Calculated Pressure Coefficient on Mixer Lobe Surface

A calibration check of the FLOMIX analysis was made by calculating the high penetration mixer lobe using the coordinates obtained from the PLANMIX inverse analysis. The FLOMIX program can be used to simulate a planar configuration by modifying the lobe coordinates so that the mean radius R_m in the axisymmetric mode is sufficiently large ($R_m \gg 0$). The fan nozzle and centerbody walls were assumed planar and sufficiently displaced so that no wall interaction effects were present. FLOMIX perturbation velocity component calculations, shown in Figures 7a, b, and c, are compared to the PLANMIX results. The two solutions are essentially identical. Further validation of the FLOMIX code are presented in References 5 and 6, where calculations for the lobed mixer for the Energy Efficient Engine (E3) in a powered environment are compared to experimental data (Ref. 12). Considerable agreement was obtained although this case pushed the limits of the small disturbance theory.

The validated FLOMIX program was used to design an advanced high penetration lobed mixer, taking advantage of the experimental configuration base that was obtained in the E3 program. The mixer cross-sectional contours, formed by radii and circular arc segments, tended to be less peaked than the sinusoidal type lobe section. A variation on one of the better performing designs was adapted from an axisymmetric to a planar format. Several key geometrical parameters were preserved in this adaptation in order to be consistent with the empirical design procedure used in the original axisymmetric design. Referring to the nomenclature in Figure 8, the specific procedure that was followed is:

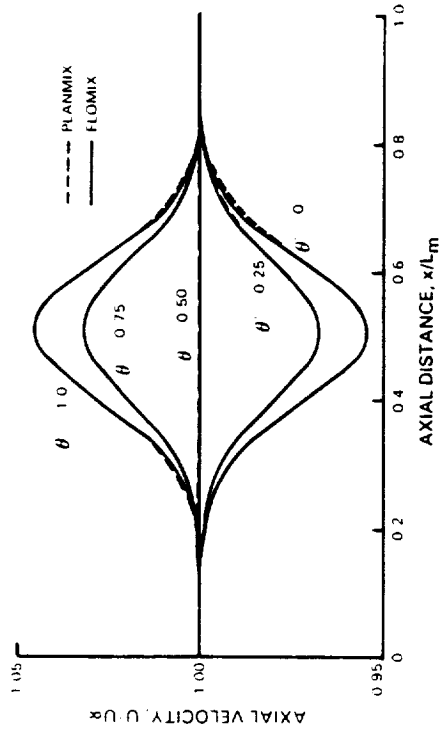


Figure 7a Comparison Calculations of Axial Velocity for a Symmetric High Penetration Mixer in a Planar Duct

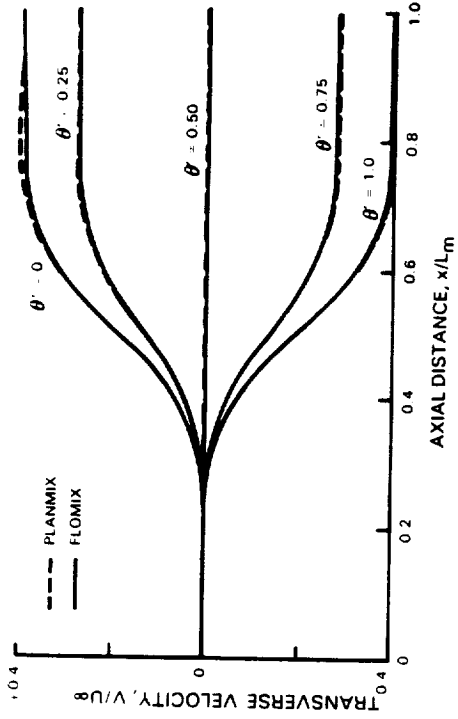


Figure 7b Comparison Calculations of Transverse Velocity for a Symmetric High Penetration Mixer in a Planar Duct

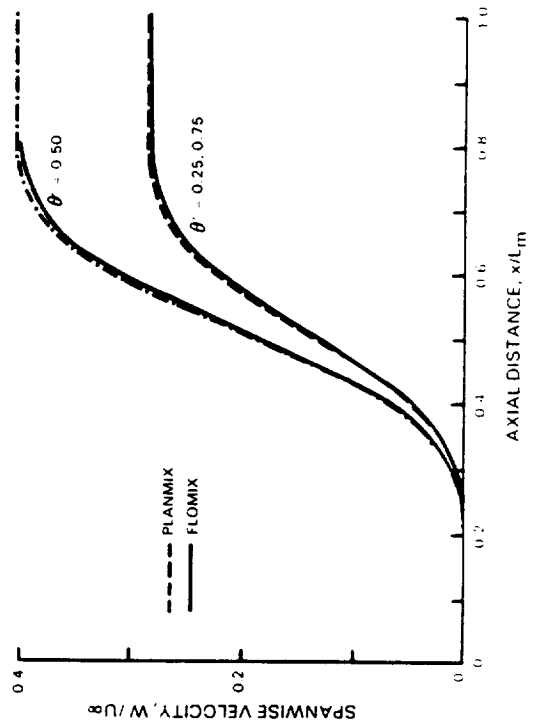


Figure 7c Comparison Calculations of Spanwise Velocity for a Symmetric High Penetration Mixer in a Planar Duct

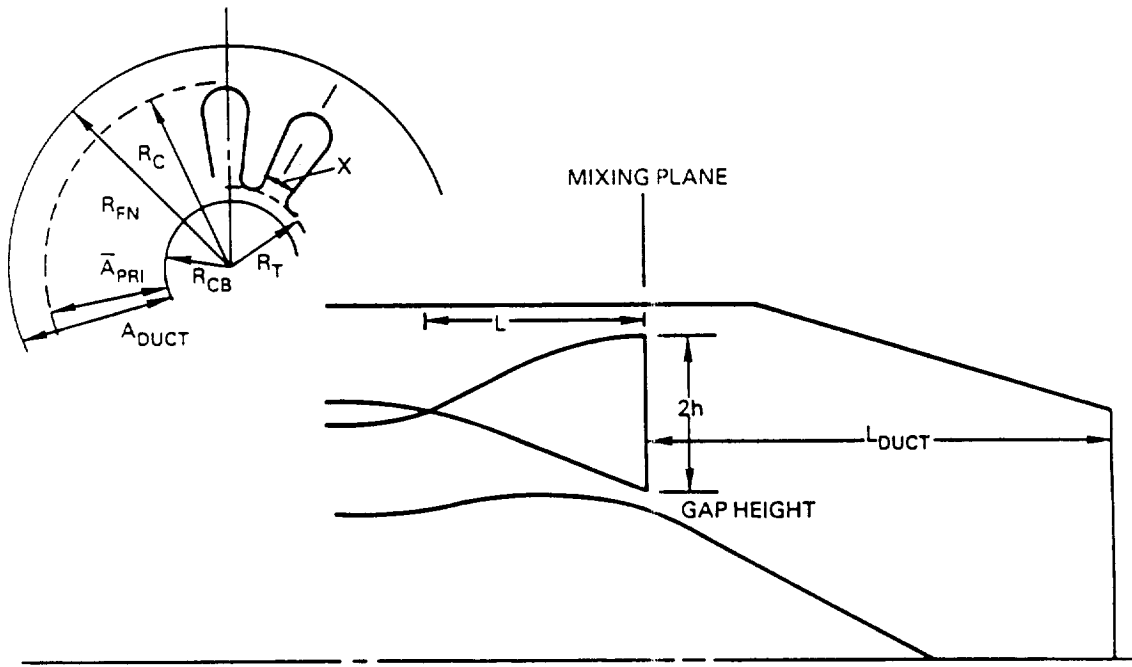


Figure 8 Mixer Performance Parameter Nomenclature

- 1) Increase R_m and the number of lobes proportionately so that $R_m/L_m \ll 1$ produces a planar surface with the same lobe width X , i.e.,

$$X = 2\pi (R_m/N_{lobes})$$

- 2) Maintaining the lobe turning angle, (h/L_m) , implicitly maintains the lobe aspect ratio

$$AR = X/h = 2\pi (R_m/N_{lobes}) h$$

- 3) The lobe penetration, $Pe = A_{pri}/A_{duct}$ is implicitly preserved by holding the primary and bypass flow areas constant,

$$A_{noz} - A_{Rm} = \text{constant} \longrightarrow R_{noz}$$

$$A_{Rm} - A_{clbdy} = \text{constant} \longrightarrow R_{clbdy}$$

Calculations for this planar advanced high penetration lobed mixer design were made using the FLOMIX code. Calculations were also made for this configuration using the three-dimensional VSAERO panel code (Refs. 13 and 14). In this latter calculation, no geometrical assumptions are made in the analysis and its limitations to nonpowered applications or irrotational flows is appropriate for the planar experiments in this contract. The paneling breakup model used for the planar duct is shown in Figure 9, while the details of the lobe paneling is shown in Figure 10. The lobe surface, after the break point, is treated as a zero thickness surface of source panels. Figures 11 and 12, show predicted surface pressure coefficient comparisons for the two codes at

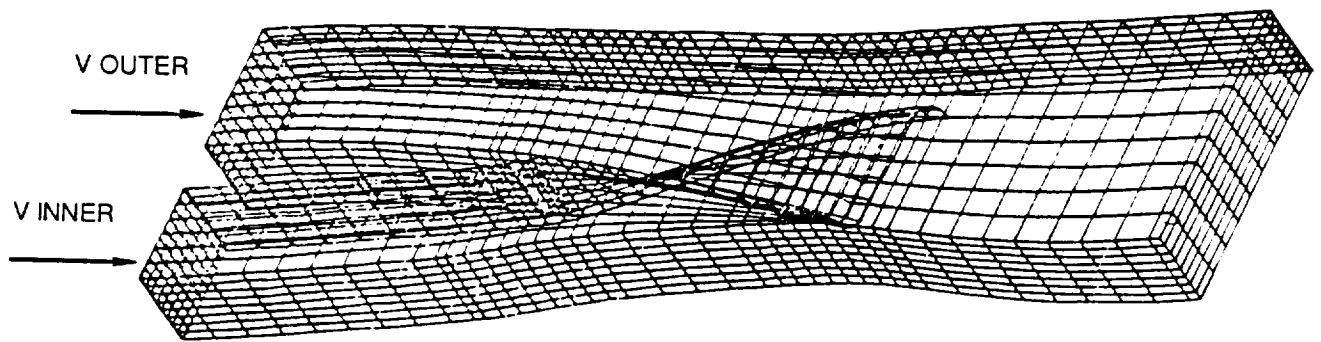


Figure 9 VSAERO Panelling Model of Advanced High Penetration Lobed Mixer with Close Coupled Duct Walls

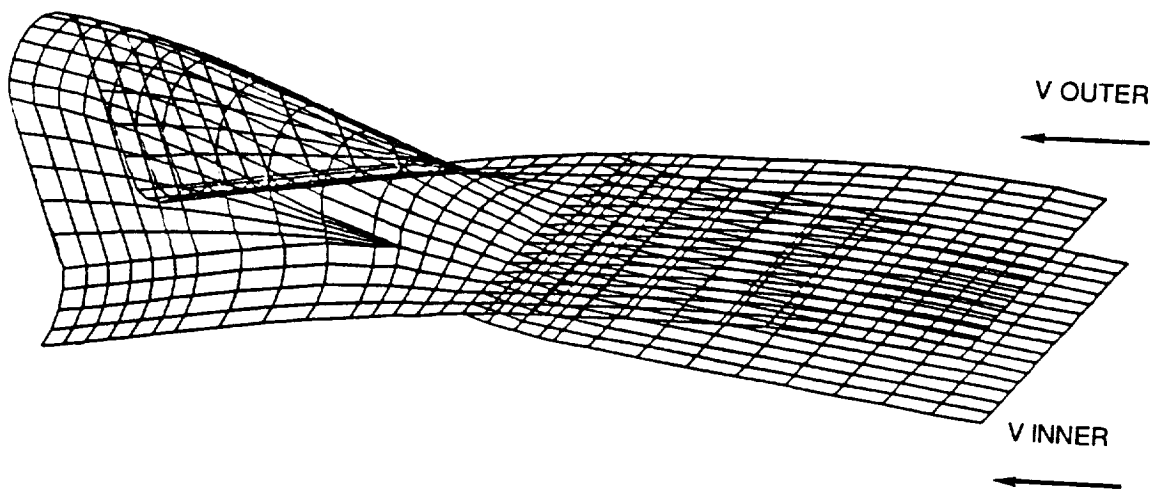


Figure 10 VSAERO Panelling Model of Advanced High Penetration Mixer Lobe Contour

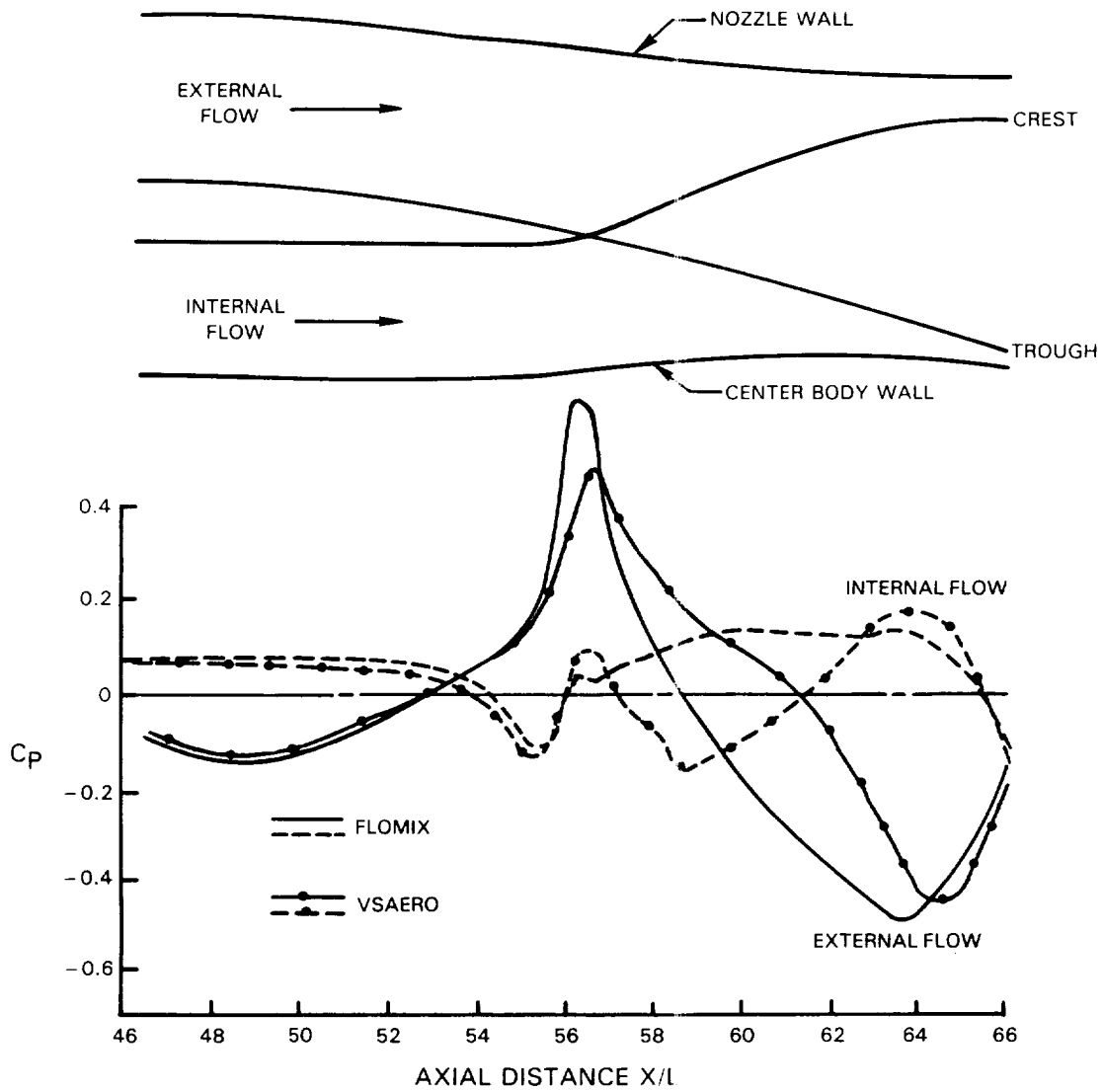


Figure 11 Comparison Calculations of the Surface Pressure Coefficient for the Advanced High Penetration Mixer Lobe Crest ($\theta = 0$)

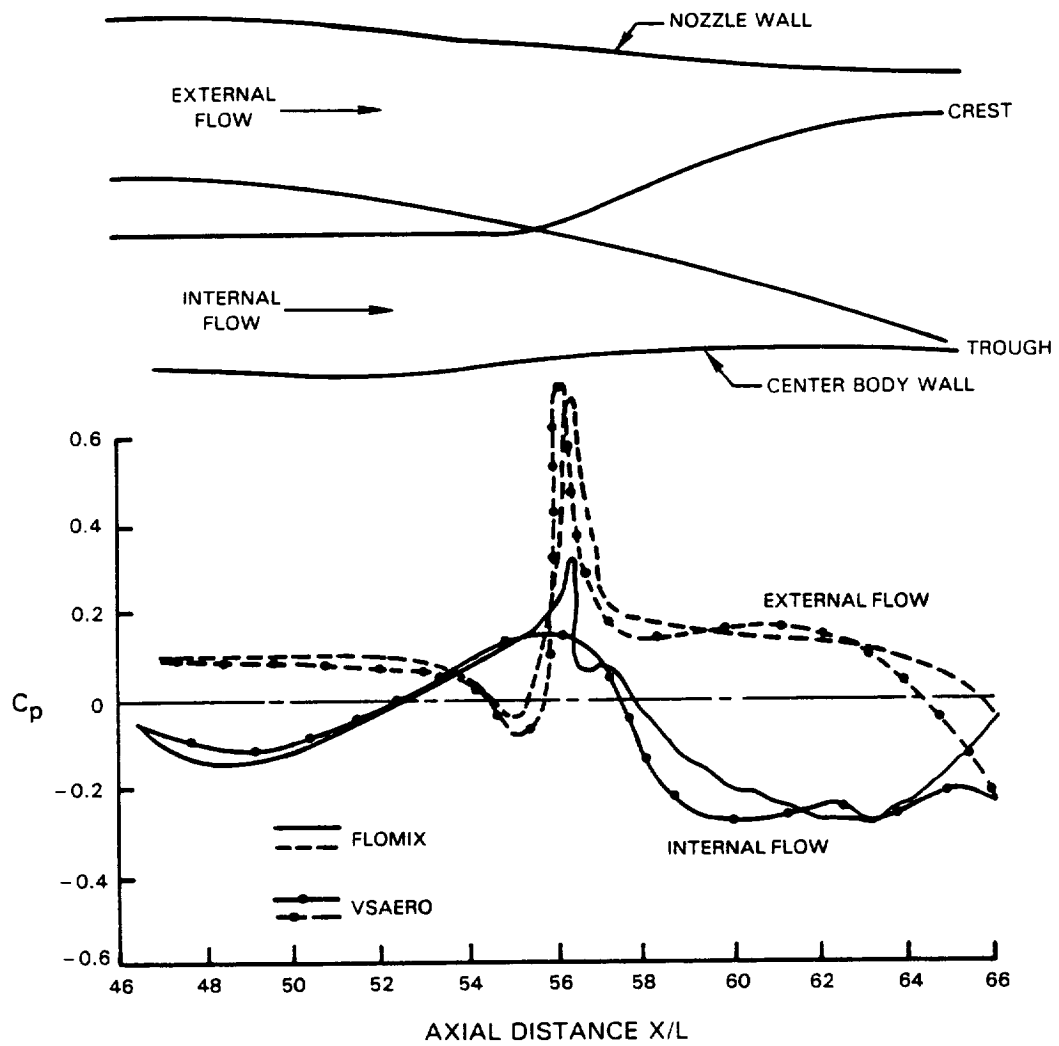


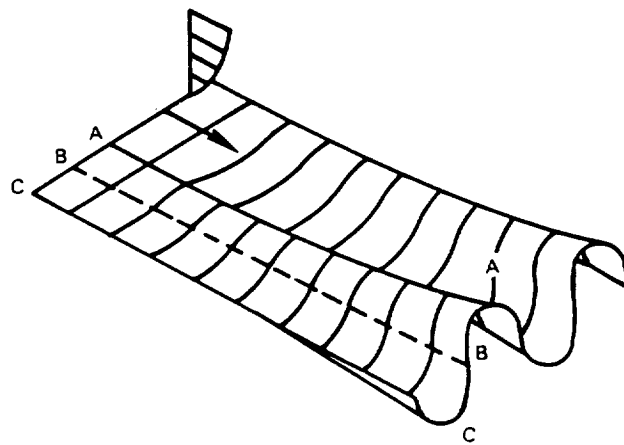
Figure 12 Comparison Calculations of the Surface Pressure Coefficient for the Advanced High Penetration Mixer Lobe Trough ($\theta' = 1$)

the crest and trough planes. The degree of agreement is quite good considering the substantial differences in the formulations and the high degree of penetration. One should again note the dramatic influence of the lobe surface curvature at the break point ($x = 55.$) on the pressure coefficient.

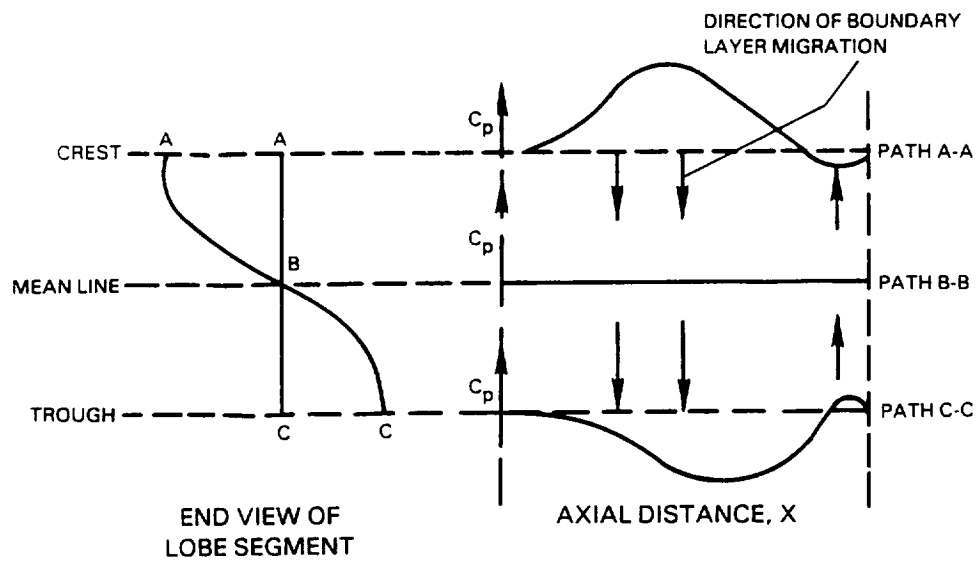
Two different linearized analytical formulations were used to design generically different lobe cross-sectional contours. The codes were first validated independently against data and for the same configurations. In the experimental phase of the program, the three lobe mixer designs will be used to:

- o validate the linearization approach for low and high penetration lobes,
- o examine effect of lobe shape on the secondary flow,
- o examine the effect of closely spaced (duct) walls on the secondary flow.

In addition, the analytical predictions for the three lobe designs were examined to deduce some observations about the nature of the inviscid flow. In all cases, the results shown in Figures 6, 7(b) and 11 indicate that the induced pressure gradient is heavily driven by the surface curvature field. Furthermore, this gradient sets up a spanwise pressure gradient that drives the flow from the lobe crest and into the lobe trough. This process is shown qualitatively in Figure 13. In part (a) of the figure, three paths from inlet to exit of the lobe are shown. Path A-A is along the upper surface or lobe



(a)



(b)

Figure 13 Lateral Pressure Field Established by Lobe Contour

crest. Path C-C is along the lobe trough and Path B-B is along the mean line between the crest and trough (R_m). The left portion of Figure 13 (b) shows a geometric view of the three paths relative to the mean planar surface as viewed from downstream while the right portion displays the qualitative static pressure distributions, as inferred from the inviscid flow calculations. The existence of the initial compression region on the lobe crest is clearly seen in Figures 6, 7b and 11. The existence of a second compression zone near the lobe trailing edge but along the lobe trough can be proposed and related to the lobe curvature in the trailing edge region. This can be graphically seen in the three-dimensional color displays of the surface pressure coefficient calculated using the VSAERO code. Figures 14 and 15 display the solution on the upper or bypass surface while Figure 16 displays the inner or core flow result. The color bar has been set so that the bottom purple bar refers to high pressure and the upper red bar to low pressure. The initial flow off the lobe crest is demonstrated in the flow from blue to red. The previously postulated second compression zone is seen in the subsequent flow from red back to green. These results, therefore, indicate that the inviscid flow field, driven by the Kutta condition applied at the lobe trailing edge, pushed the flow off the lobe crest and into the trough, thereby setting up a circulation pattern that will drive the downstream mixing process.

ORIGINAL PAGE IS
OF POOR QUALITY

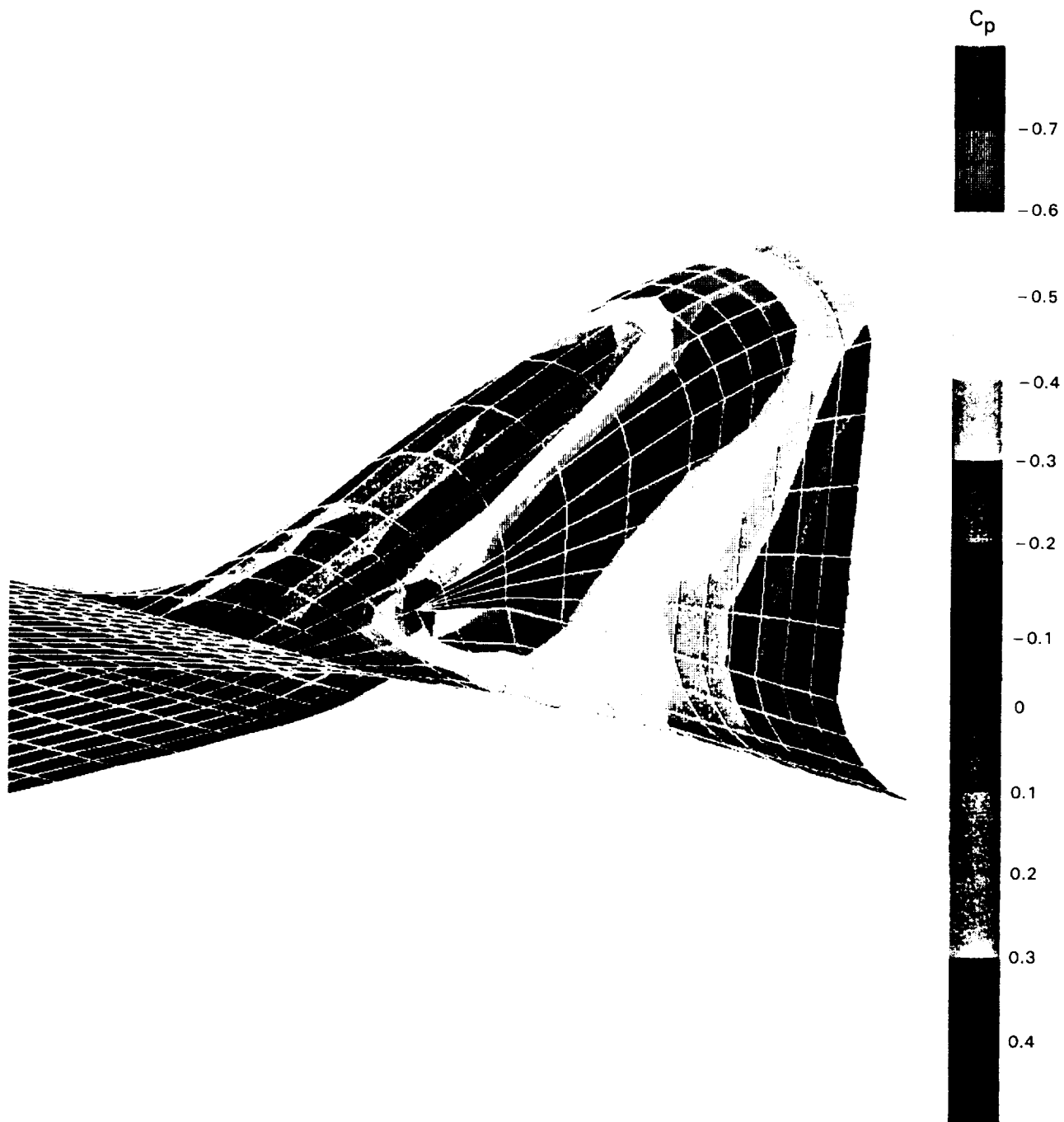


Figure 14 VSAERO Display of Pressure Coefficient on Outer Surface of Advanced High Penetration Mixer

ORIGINAL PAGE IS
OF POOR QUALITY

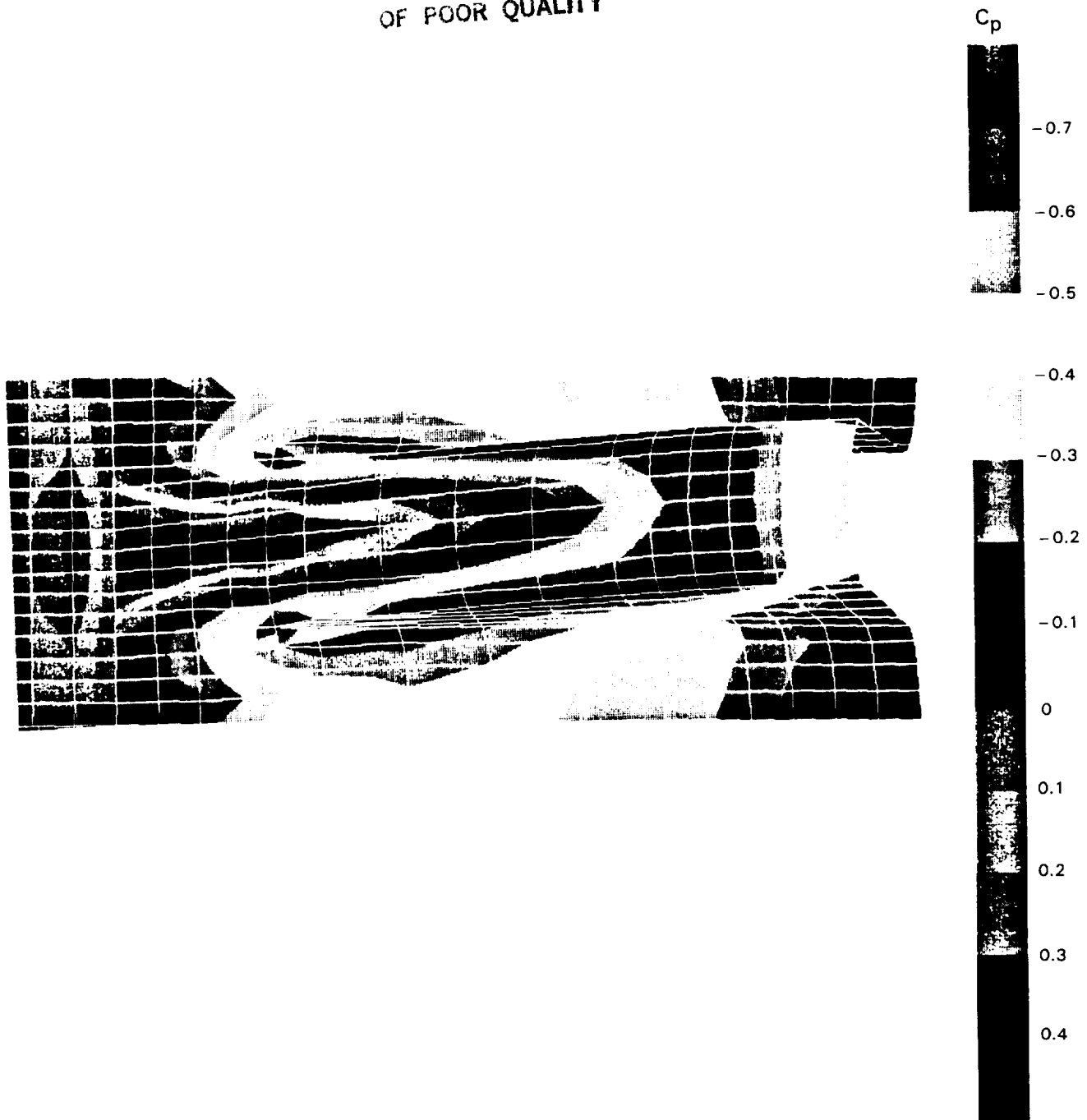


Figure 15 VSAERO Display of Pressure Coefficient on Outer Surface of Advanced High Penetration Mixer

ORIGINAL PAGE IS
OF POOR QUALITY

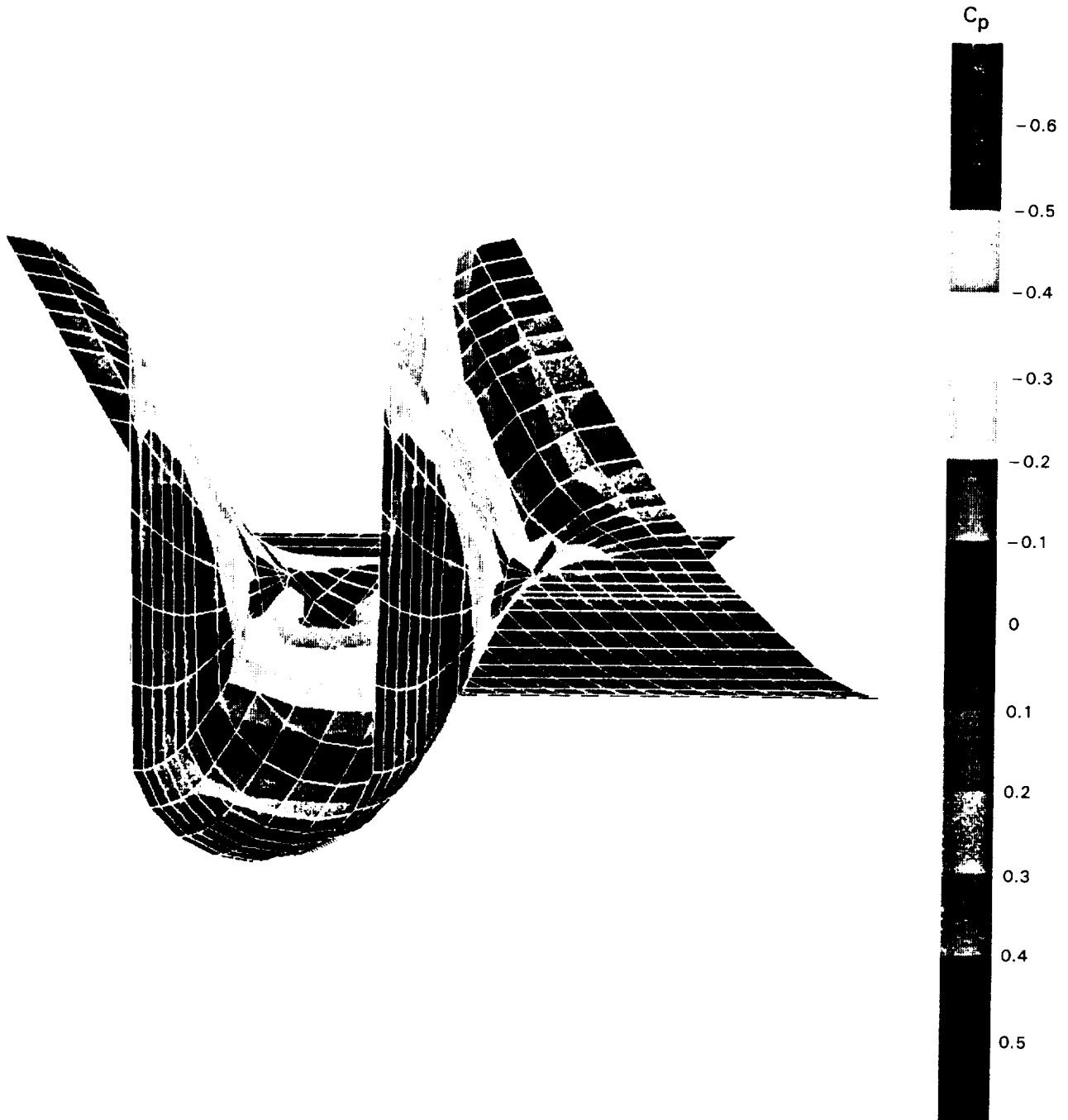


Figure 16 VSAERO Display of Pressure Coefficient on Inner Surface of Advanced High Penetration Mixer

IV. DESCRIPTION OF EXPERIMENT

A. Experimental Arrangement

1. Mixer Lobe Cascade Facility

The experiments were conducted in the UTRC Mixer Lobe Cascade Facility shown schematically in Figure 17. This facility is primarily of plexiglass construction, with air circulated by a low pressure/high volume centrifugal fan. The fan supplies air flow at slightly above atmospheric conditions to a settling chamber containing screens and honeycomb to reduce velocity nonuniformities. The flow then enters a 5.6 area ratio contraction, passes through a 20.32 x 21.59 cm (8 x 8.5 in.) rectangular test section, and is returned by ducting to the fan inlet. Tunnel temperature is equilibrated by discharging a portion of the fan-warmed air flow from the return ducting and replacing it with cooler atmospheric air drawn in through a separate fan inlet port. The settling chamber and connected contraction and test sections are vibrationally isolated from the rest of the tunnel to enable precise positional measurements to be made in the test section flow.

All models were stationed a short distance downstream of the contraction section. Empty tunnel flow uniformity at this station, as documented by laser velocimeter measurements was approximately one-quarter percent of U_∞ . Test section velocity and total temperature were nominally 37 m/s (120 f/s) and 319°K (575°R) respectively, with both dependent to some degree on atmospheric conditions.

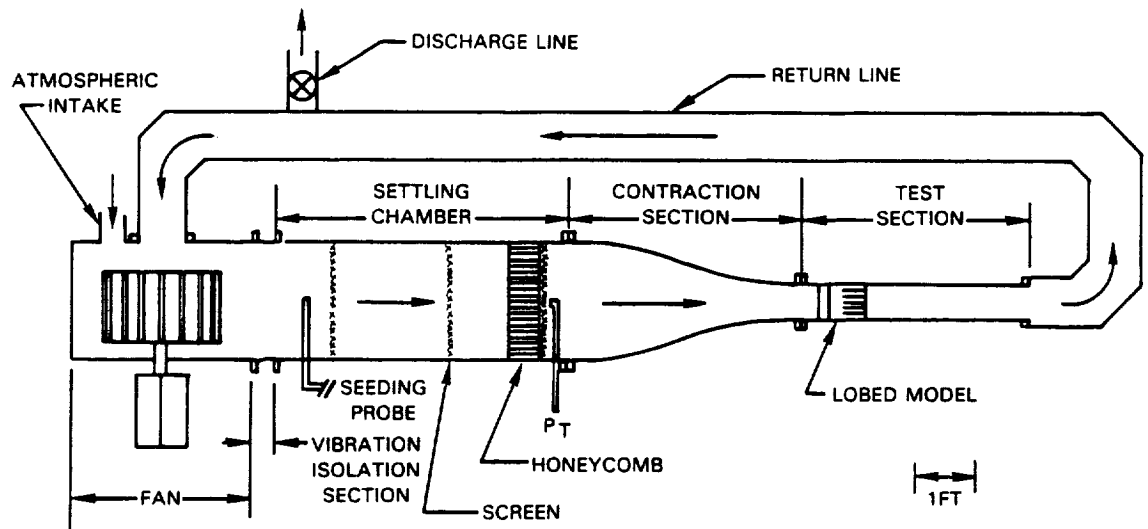


Figure 17 UTRC Mixer Lobe Cascade Facility

2. Mixer Lobe Models

Three mixer lobe models were designed and fabricated for this experimental program, two being of sinusoidal geometry and a third being an advanced design having parallel sidewalls and rounded peaks and troughs. Each model's contour, spanning the 20.32 cm (8.00 in.) wide test section, developed gradually from an initially two-dimensional surface into a three-dimensional lobed shape. All of the models were constructed of a molded fiberglass/epoxy resin composite contour attached to either an aluminum or steel leading edge. The sinusoidal geometry provided the simplest relevant mixer shape to model analytically. Exit plane contours for the two sinusoidal mixers are shown in Figure 18. The low amplitude model is termed the "Low Penetration Sinusoidal Mixer" whereas the second model, having a factor of four larger amplitude, is termed the "High Penetration Sinusoidal Mixer". A photograph of the low penetration model in the Mixer Lobe Cascade Facility is shown in part (a) of Figure 19.

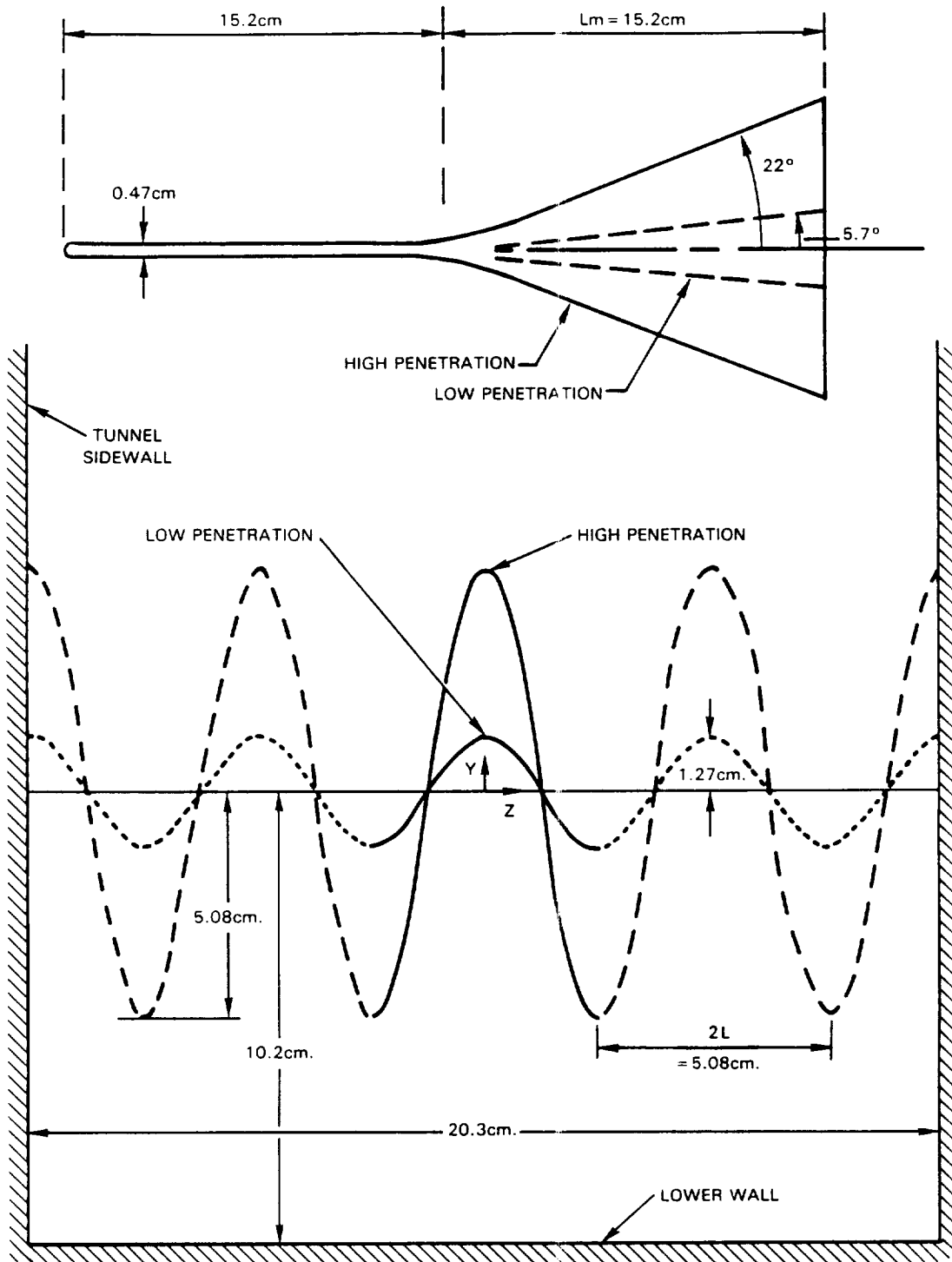
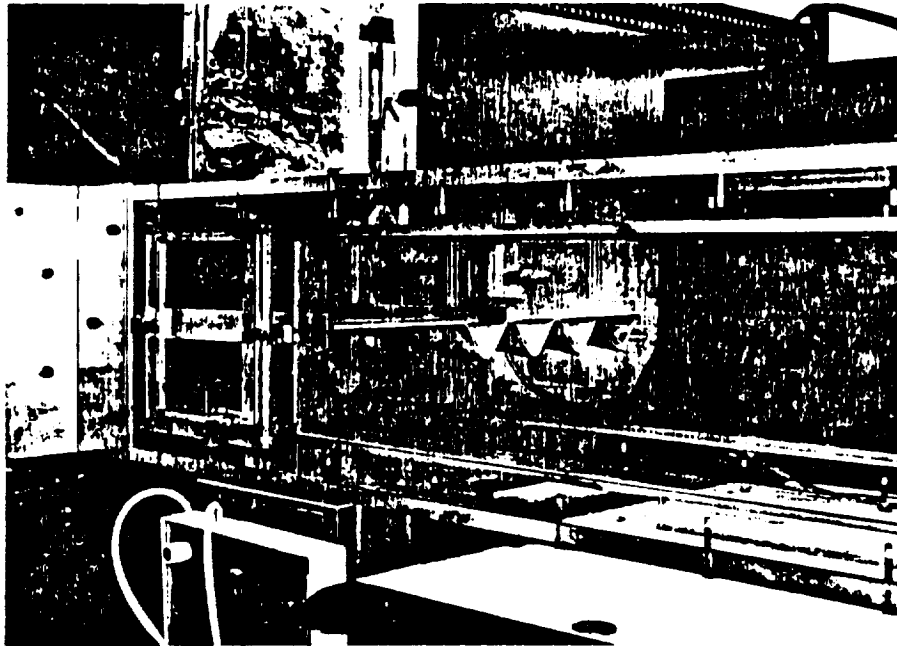
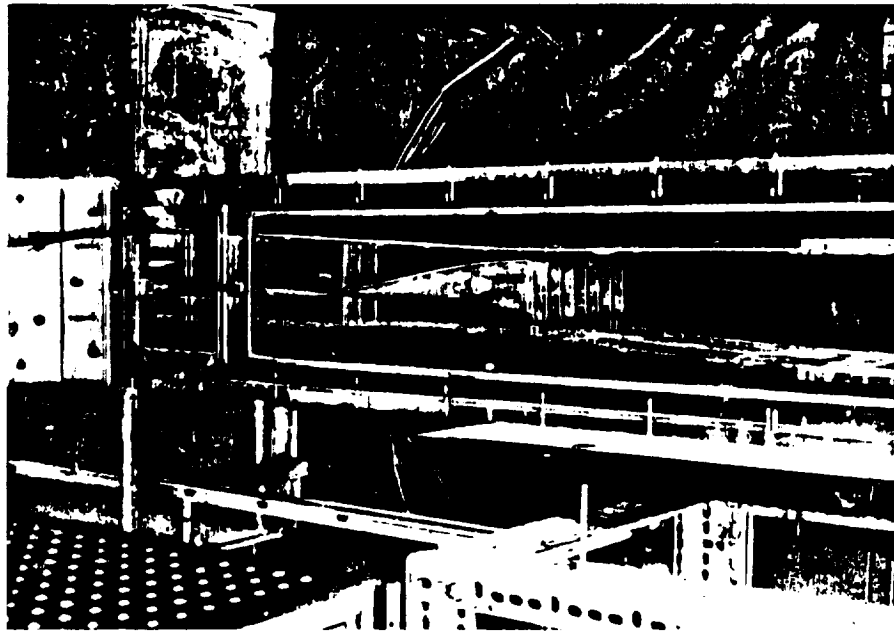


Figure 18 Low and High Penetration Sinusoidal Mixer Exit Plane Contours

ORIGINAL PAGE IS
OF POOR QUALITY



(a) LOW PENETRATION SINUSOIDAL PLANAR MIXER



(b) ADVANCED HIGH PENETRATION PLANAR MIXER

Figure 19 Planar Lobed Mixers Installed in the UTRC Wind Tunnel

The models transitioned in cross-section from a surface that was initially flat to one that was a sinusoid and whose maximum amplitude steadily increased with downstream distance. At the exit plane the mean sinusoidal lobe amplitude for the low penetration mixer was 1.27 cm (0.5 in.) and for the high penetration mixer 5.08 cm (2.0 in.). Starting from one test section wall at maximum amplitude, the contours of both models reached the opposite wall after four cycles (5.08 cm. (2.0 in.) wavelength) had been completed. Both models had the same overall length of 25.4 cm. (10 in.) and shared a common forward section to which their individual molded contours were attached. This forward section consisted of a 0.47 cm (0.188 in.) thick steel flat plate that was bracket-mounted to the test section's side walls. The plate had a rounded leading edge that was followed a short distance downstream by boundary layer trips on its upper and lower surfaces. The molded contours were mounted at the plate's trailing edge by tongue-and-groove attachment, with the trailing surface of the plate having a 5 degree bevel to make a smooth transition to the 0.10 cm (0.04 in.) thick contoured lobe surface. The downstream end of the model's molded contour was supported at the base of its outer lobes by a pair of 0.08 cm (0.032 in.) diameter rods mounted to the test section floor.

The third model, referred to as the "Advanced High Penetration Mixer" was designed to simulate, two-dimensionally, the flow field of an axisymmetric mixer lobe configuration for advanced aircraft turbofan engines. In addition to the mixer lobe contour, it was necessary for the model to include sufficient portions of the engine plug, shroud, and the turbine casing wall separating the primary and fan flows in order for flow through the lobes to be properly simulated. Therefore, the model consisted of three main components;

the lobe body, shroud, and plug. Each of these components spanned the test section and were secured to the tunnel surfaces to maintain their correct relative spacings. The exit plane contour and cross-section for this model shown in Figure 19(b) and Figure 20 is a photograph of the model installed in the lobe cascade facility. The model had the same 5.08 cm. wavelength as the sinusoidal lobes but had parallel sidewalls capped by half circles. Relative to the upstream flat plate centerline ($y=0$), the lobes were unsymmetrical in that the exit plane height of the upwardly directed lobe was 2.94 cm. (lobe interior dimension) and that of the downwardly directed lobe, 3.10 cm. The peak-to-peak amplitude of the mixer was therefore 6.04 cm., intermediate between the 2.54 cm. and 10.16 peak-to-peak amplitudes of the two sinusoidal models. In addition to having differing amplitude up and down lobes, the slope of the lobe peaks in the axial direction differed. As discussed relative to the transverse velocity components subsequently, the bottom lobe sloped at a steeper angle. Also, the trailing edge region of the upper lobe tapered to a shallow angle.

The lobe body was made up of an aluminum forebody and an attached fiberglass/epoxy resin composite contour, with an overall length of 56.24 cm (22.14 in.). Leading edge shape of the forebody was that of a 4-to-1 ellipse. This shape was blended smoothly with the attached fiberglass/epoxy resin composite contour, which modeled the two-dimensional primary and fan flow walls and transitioned into a three-dimensional lobed surface. The two-dimensional forward portion of the model was bolted to the test section sidewalls, while the rear of the model was supported by a pair of spacers attached to the plug surface and lobe trailing edge. Seams formed by the adjoining model and test section sidewalls were sealed by a fillet of silicon adhesive in order to isolate upper and lower surfaces of the model.

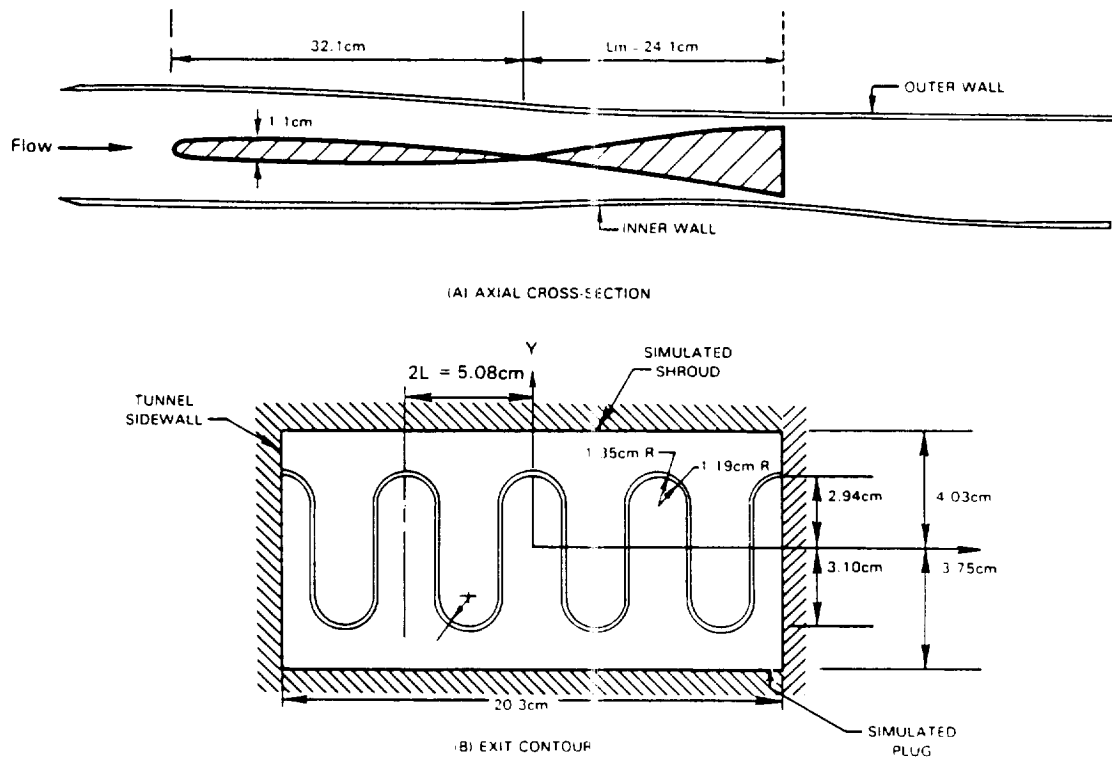


Figure 20 Advanced High Penetration Mixer Section and Exit Plane Contour

The shroud and plug surfaces were each formed by a pair of 0.95 cm (0.375 in.) thick contoured aluminum rails supporting a 0.32 cm (0.125 in.) thick plexiglass sheet across the test section width. Each of the rails had one edge flattened for bolting to the test section ceiling or floor, while the other edge was machined so that the attached plexiglass sheet would assume the appropriate axial surface contour at the correct relative spacing from the lobe body. The shroud and plug surfaces extended upstream to the test section

inlet so as to provide uniform flow to the model, with the remaining test section inlet flow diverted beneath these surfaces. Downstream of the lobe body the shroud and plug contours were extended as straight walls for a distance of some four times their wall spacing. The straight walls were approximately parallel, being set at a slight relative angle to account for wall boundary layer growth and thereby maintain a constant pressure condition downstream of the lobe model.

B. Instrumentation

Quantitative measurements made during the experimental tests included Laser Doppler Velocimetry (LDV), flow total pressures, wall static pressures, inlet boundary layer documentation and positional information. Qualitative understanding of the flowfield was also obtained by means of surface oil flow visualization.

1. Laser Doppler Velocimetry

A commercially available 2W argon-ion laser system was used for making flow velocity measurements in the tunnel test section, with the laser system mounted on a manually controlled three-axis traverse table and interfaced with a computer for data processing and storage. The system, similar to that employed in the previous mixer nozzle study (Reference 4) was configured in a dual beam ("fringe") mode using 0.5145 micron wavelength light, with collecting optics typically positioned for forward scatter. By means of heterodyne detection of the Doppler shift in the light collected from the

intersection of incident beams during seed particle passage, instantaneous flow velocity was obtained for that component which was in the plane of and perpendicular to the bisector of the incident beams. Bragg shifting was used to eliminate directional ambiguity. Axial and spanwise velocity components were taken by passage of the light beam through the test section's glass sidewalls, while the vertical velocity component was measured by reflecting the beams down through a glass window mounted in the test ceiling and operating the laser system in a back-scatter mode.

Flow seeding for the sinusoidal lobe tests was by means of aluminum oxide particles having a nominal diameter of 0.3 micron, which were fluidized in a low pressure seeder and injected into the closed loop tunnel downstream of the test section. Seeding for the advanced model test was accomplished by atomizing corn oil, having a nominal diameter of 1.0 micron, and injecting it into the flow upstream of the settling chamber through a seeder probe designed to minimize flow disturbance.

The collection optics signal was sent to a counter-type signal processor. Operated in its continuous mode, the processor measured the time for a particle to cross 8 fringes and then transferred this information to the computer. Typically, 1000 such measurements were taken per data point in order to calculate a mean value and standard deviation of the velocity component. Data point locations were established based on choosing a point on the model as a coordinate origin and recording relative distances from this origin as provided by calibrated potentiometer outputs on the laser system traverse table.

2. Total and Static Pressures

Total pressure measurements made during this test program included detailed planar surveys downstream of each model, boundary layer traverses at selected model locations, and continuous tunnel operation monitoring. Total pressure in all cases was sensed by a dedicated transducer whose calibration was checked prior to and following each test run. Types of probes used included a kiel head probe for the planer surveys and a flattened impact probe for the boundary layer traverses. The probe support exited the test section through a sidewall slot and was mounted to and moved by a computer controlled two-axis traversing unit. Tunnel total pressure was measured with a pitot-static probe mounted in the upstream end of the test section floor during the sinusoidal lobe tests and with a kiel probe located downstream of the last flow straightening screen in the settling chamber for the advanced mixer tests.

During the sinusoidal lobe tests, the test section static pressure was obtained with a floor mounted pitot-static probe in the upstream end of the test section. In addition, the common forward section of the two sinusoidal lobe models had a pair of static taps on both upper and lower surfaces to assist in aligning the model with the incoming stream. For the advanced penetration model tests, forty-six static pressure taps were provided at locations distributed over the model surface and wind tunnel walls.

3. Flow Visualization

A variety of standard flow visualization techniques were applied to gain understanding of the flow about the lobe models. These included tuft and smoke motion and oil film surface patterns. Fluorescing dye was mixed with the oil prior to surface application in order improve surface pattern clarity.

4. Boundary Layer Definition

Hot wire anemometry was employed to define the boundary layer approaching the lobe region of the models. Surveys were taken on the upper and lower surfaces in the leading edge region.

5. Experimental Technique

Test preparation involved installation of a model in the tunnel test section, calibration of measurement equipment, and preliminary measurements in the flowfield to verify correct model placement. The sinusoidal models were initially positioned to be aligned with the tunnel centerline horizontal plane. Preliminary tests were then performed, by measuring static pressures via taps in the models' common forward section, and the model's pitch angle adjusted, if necessary, to achieve a proper zero flow angle alignment. In the case of the advanced penetration model, its three components were designed to maintain fixed relative spacings, with the entire assembly mounted horizontally

in the test section such that the tunnel centerline bisected the initial lobe station. A preliminary test was similarly performed for this model by sampling all static pressure tap locations to insure that proper component alignment and spacing had been met. All model edges in contact with the test section sidewalls were sealed to prevent leakage between upper and lower surfaces.

Equipment preparation primarily involved the laser system, including alignment of the laser table, adjustment of the laser optics, activation of the data acquisition software, locating the positional origin of the model, and fine tuning the signal processor and seeding supply to obtain a satisfactory signal-to-noise ratio and data rate. A double check was made to verify that the LDV measured velocity values were correct. The first consisted of determining the velocity at a given radius on a wheel rotating at a constant rate with the LDV and comparing that result with the algebraically computed value. The second method was to compare the LDV measured velocity at a point in the test section flow with the value computed from a pitot-static probe measurement at the same point. Good agreement was realized with both methods.

For test runs in which a total pressure survey or boundary layer traverse was to be taken, preparation included alignment of the traverse mechanism, locating the positional origin, and check-out of the computer controlled traverse unit, data acquisition software, and pressure transducer calibration.

Prior to taking data, the tunnel was operated for a sufficient length of time to produce quasi-equilibrium test section conditions. Following this, the barometric pressure, laser optics information, and signal conditioner settings were recorded and a final correction made in the positional origin to account for tunnel growth.

The test procedure for acquiring LDV data was to record the barometric pressure, laser optics information, and signal conditioner settings into the computer, then position the probe volume at either the maximum or minimum of the Y-axis survey plane, activate the seeding system, execute the LDV data acquisition program to acquire 1000 valid samples of the velocity component at that location, stop the seeding system, review the velocity histogram following completion of the on-line processing to insure that the data point is acceptable, instruct the computer to store this result along with the test section total pressure and total temperature, and finally manually control probe volume movement to the next Y-axis location. The seeding system was again started, and the same acquisition steps repeated until a complete vertical (Y-axis) traverse of approximately 30 different point locations had been acquired. This resulting collection of data points was designated as a 'run'. The laser probe volume would then be moved to the next spanwise (Z-axis) position and the entire procedure repeated until traverses at required spanwise locations had been completed. These steps were again repeated twice more to obtain the remaining two components of velocity.

Acquisition of total pressure survey data was facilitated by computer control of both probe movement and data acquisition and reduction. After having manually positioned the total probe at a starting location in the survey grid, the computer software program was initiated to sample the probe pressure and test section pressure and temperature, compute and output test parameters, store the data, move the probe to the next designated grid location, and repeat these steps until array completion. Boundary layer traverse data was obtained in a similar manner, but with manual control of probe movement based on operator selection of appropriate traverse data point locations.

Flow visualization tests were performed by forming a solution of medium-weight gear oil and a florescent pigment, applying this mixture as small dots randomly spaced on the model surface, operating the tunnel for a period sufficient to allow the dots to spread and thin under the action of aerodynamic forces, opening the test section, and photographing the patterns under ultra-violet illumination.

6. Data Analysis

Data reduction was performed by on-line computers for this test program, with a mini-computer used for the LDV and a personal computer (PC) for the total pressure measurements. Software programs were written for each to meet specific test requirements.

For the LDV test phase, data was sent to the computer via the signal processor. The processor transmitted a number identifying the amount of time taken for a flow seed particle to travel a known distance through the laser probe volume. From previously input parameter constants related to the laser optics, geometric alignment, and beam properties, the program could compute this distance and hence a flow velocity. In order to achieve an accurate velocity measurement, 1000 samples were taken and stored for each point location. The program calculated a velocity value for each sample and computed a mean and variance of the sample population. A histogram was generated by dividing the total range of possible velocities, as determined by the filter settings of the signal processor, into 100 equal ranges or 'bins' and then assigning each of the sample velocities to its appropriate bin. The bin containing the most samples was located by the program, adjacent bins above and below this central bin sequentially tested until sampleless bins were found, and a mean and variance computed for this resulting sample subset. The operator could choose a subset of this reduced population, if upon examining the histogram it was found that the distribution was skewed appreciably from the expected Gaussian distribution. In that case, a mean and variance would be computed for this new subset. The mean and variance was stored along with probe location and tunnel condition information for each data point.

Model reference velocity, U_{∞} , was computed from Bernoulli's equation, using the test section pitot-static probe pressures for the sinusoidal lobe models and the test section total pressure together with an average of the plug and shroud upstream static tap pressures for the advanced penetration model.

The total pressure survey data was processed by calculating a normalized total pressure for each of the survey data points. Boundary layer calculations were based on the assumption of constant static pressure across the layer.

V. RESULTS AND DISCUSSION

A. Experimental Observations

1. Data Presentation

This section of the report presents three-dimensional mean velocity and total pressure measurements acquired just downstream of the mixer lobe exit plane for the three mixer configurations considered in this study: Model 1- Low Penetration Sinusoidal Mixer, Model 2 - High Penetration Sinusoidal Mixer and Model 3 - Advanced High Penetration Mixer. Geometrical characteristics of these three mixer configurations are described in the section, "Description of the Experiment".

Data are presented at a location downstream of the trailing edge, $\bar{x} = x - x_{TE}$, as a function of spanwise (lateral) position, z , and transverse position, y . The coordinate system was previously shown in the sketch on page 9. These coordinates represent physical values normalized by the lobe half-wavelength of $L = 2.54$ cm. All other lengths such as boundary layer parameters are presented in this normalized format. Tables D.1.1-3, D.2.1-3 and D.3.1-3 provide Laser Doppler Velocimetry (LDV) measured axial, transverse

and spanwise mean velocity components ($U_\infty + u, v, w$) for the three configurations, respectively. Tables D.1.4 and D.2.4 present exit station total pressure measurements for the sinusoidal mixers in terms of a normalized total pressure, \bar{P}_T . As defined in the List of Symbols, \bar{P}_T represents the measured total pressure referenced to the upstream reference static pressure, p_∞ and normalized by the reference dynamic pressure, q_∞ . Table D.3.4 presents total pressure results for the advanced mixer in terms of the ratio of measured to upstream total pressure. The following discussion of results begins with the Model 1 low penetration mixer and proceeds through the remaining two models.

The axial component is given as a fraction of the upstream reference velocity, U_∞ . Secondary flow components v and w are presented in a non-dimensional form with the upstream reference velocity, U_∞ , as the normalizing quantity.

2. General Observations

Axial velocity and total pressure measurements at the exit plane of the two sinusoidal waveform mixers indicated significant viscous retardation effects occurred within the lobe region. Low momentum fluid tended to be concentrated in the peak region within the lobe interior. Similar measurements acquired with the advanced high penetration mixer showed much thinner lobe boundary layers with inviscid flow extending well into the rounded lobe peak region.

Transverse velocity measurements at the exit plane of all three models showed significant cross-stream flows on the order of 10 to 30 percent of the lobe exit axial velocity. Magnitudes were largest for the high penetration sinusoidal model which also had the largest lobe amplitude (or equivalently, largest ramp angle). Transverse velocity magnitudes diminished in the interior lobe peak region of the sinusoidal models whereas the advanced mixer displayed near ideal velocity levels well into the lobe peak.

Spanwise velocity component magnitudes at the lobe exit plane were substantially smaller than the transverse component for all three models. The combined transverse - spanwise secondary flowfield was characterized by two counter-rotating axial vortices located within each spanwise wavelength of the periodic models. The circulation associated with each axial vortex was found to be dominated by the contribution from the transverse velocity field.

Surface flow visualization of the lobes showed skewing of the near surface flow toward the lobe peak and trough regions. The degree of skewing was greatest for the two high penetration models. The direction of lateral boundary layer fluid migration was in agreement with the direction of lateral pressure gradients predicted by the analyses.

3. Mixer Lobe Flow Visualization

Surface flow visualization patterns for all three models considered in this study were qualitatively similar and in agreement with expectations based on the analytically predicted lobe surface pressure distributions given in

Section III and shown schematically in Figure 13. These distributions are reviewed briefly here. As shown in Figure 6, both sinusoidal mixers display an initial pressure rise (dp/dx) along the crest line ($z=0$), followed by a maximum and decline back to freestream pressure. The pressure distributions are similar, as would be expected for geometrically similar designs, but four times larger for the high penetration model because of the amplitude ratio of four. The trough line ($z=1$) distribution is similar but of opposite sign and the mid-lobe position ($z=.5$) shows no deviation from freestream static pressure. As shown by the contours, a pressure gradient (dp/dz) exists from crest-to-trough and is a maximum at an axial position midway through in the lobe and between $z=.25$ and $.75$. This spanwise region coincides with the region of steepest spanwise slope of the cosine function describing the contour ($y = h \cos \pi z$).

A photograph of the two sinusoidal mixer models is provided in Figure 21. Surface flow visualization for the low penetration model displayed a weak spanwise flow from crest to trough in response to the above described pressure gradient. Surface flow visualization for the high penetration model, given in Figure 22, was much more dramatic, displaying a downwardly skewed near surface flow from crest to trough. This surface flow is particularly evident midway through the model on the steep sides of the lobe, as expected based on the above. Also evident is skewing of the approach boundary layer at the entrance to the lobe region. Surface streaks aligned with a trough ($z=1$) run directly aft down the trough centerline. Streaks aligned between trough and crest ($z=0$) are rapidly turned laterally toward trough centerline. These results indicate

LOW PENETRATION

HIGH PENETRATION

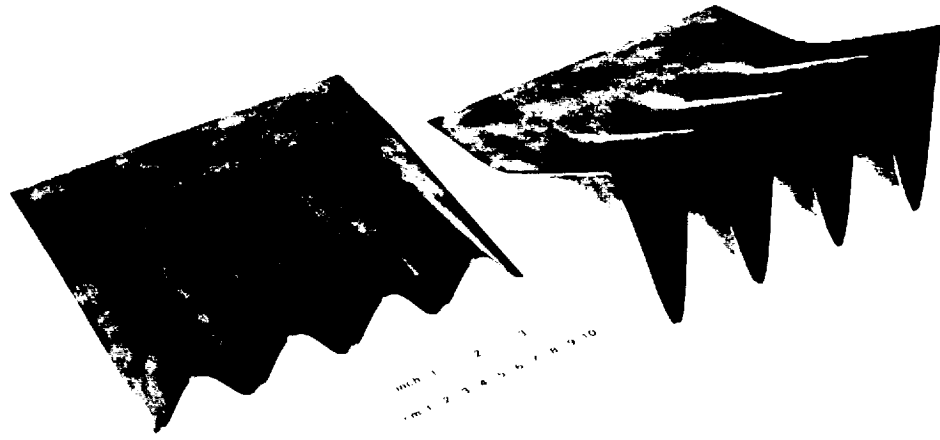


Figure 21 Sinusoidal Mixer Models

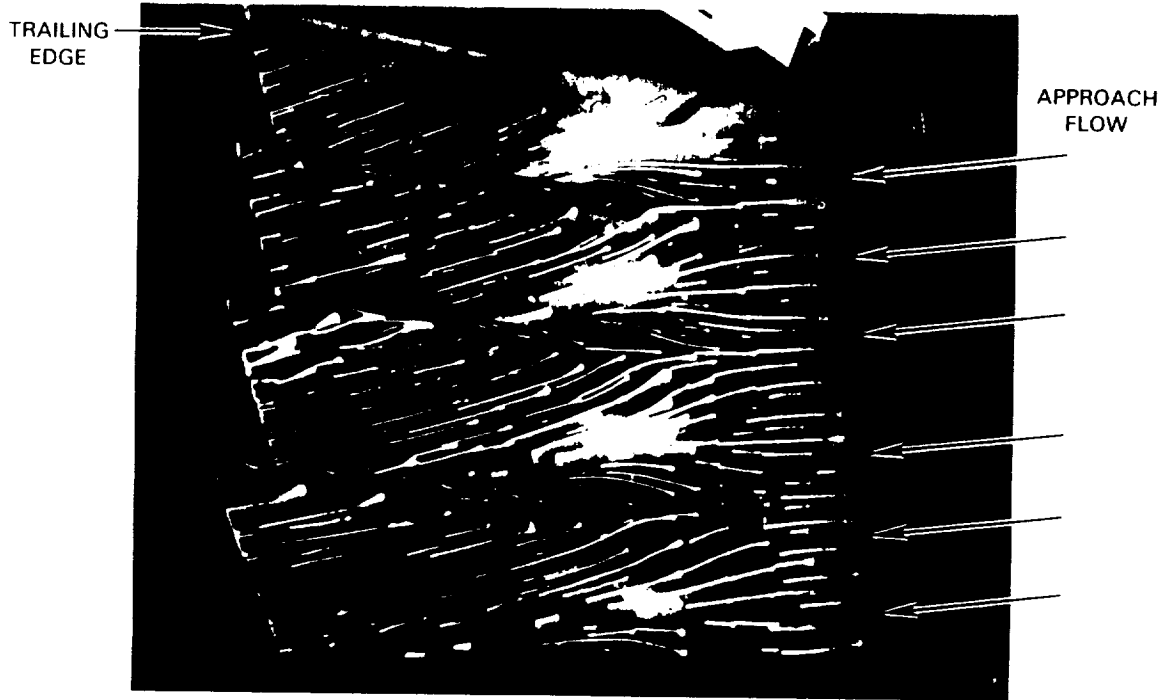


Figure 22 Flow Visualization Study of Surface Streamline Pattern on High Penetration Planar Mixer

that the low momentum boundary layer fluid approaching the model should gather in the trough thereby producing blockage in the bottom of the trough at mixer exit. This blockage is confirmed later when axial velocity and total pressure data are examined.

Analytical predictions of pressure distributions for the advanced mixer are shown in Figures 11 and 12 and in Figures 14-16. For this discussion we shall concentrate on flow patterns as viewed from the top of the model for which the crest pressure distribution is given by the Figure 11 curve labeled "external flow". The curve displays a rapid rise (flow deceleration) at Station 56 which is the beginning of the lobe region. This is followed by a decline (acceleration) to Station 64 and final return to freestream static pressure at mixer exit, Station 66. The trough pressure distribution is given by the Figure 12 curve labeled "internal flow". The curve displays the same character as the crest distribution except magnitudes are lower. The net effect, when the curves are overlaid, is that a pressure gradient from crest to trough exists over the length of the model except for a weak gradient from trough to crest near the trailing edge. The maximum gradient exists at the lobe entrance (Station 56). The above described pressure pattern is sketched in Figure 13.

Advanced penetration model flow visualization shown in Figure 23 displays the spanwise skewing from crest to trough expected based on the above pressure distributions. Particularly evident is the strong curvature of surface traces on the lobe crest midway through the mixer. One would infer from these pictures that significant thinning of the crest boundary layer would occur at the expense of trough boundary layer thickening. As discussed below, boundary layer measurements obtained at mixer exit confirmed these expectations.

TRAILING EDGE IS
OF POOR QUALITY

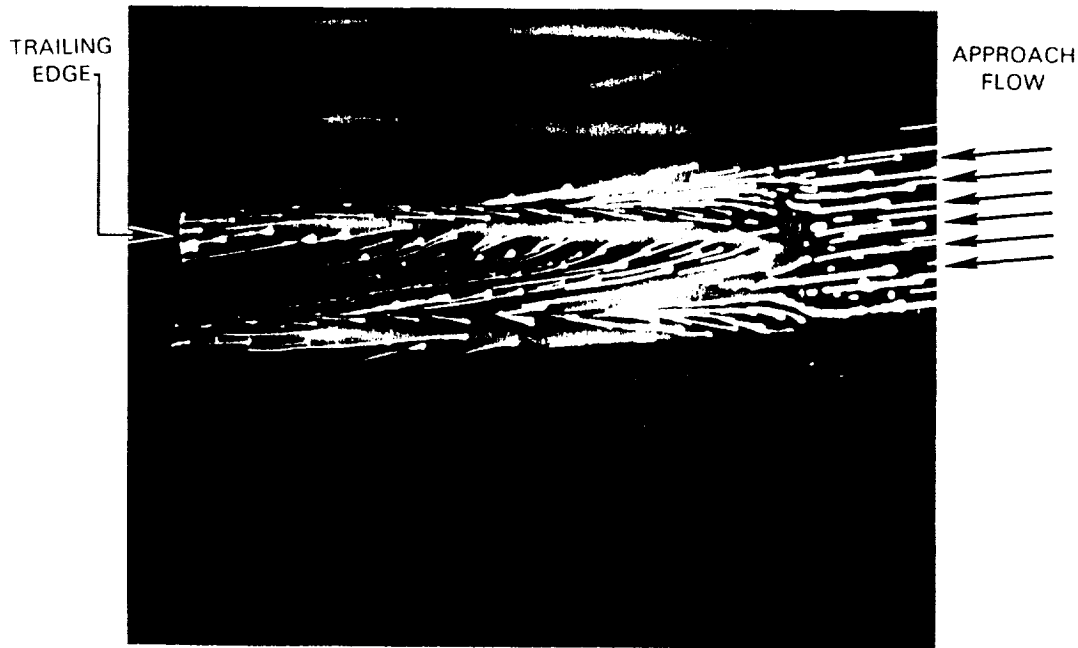


Figure 23 Flow Visualization Study of Surface Streamline Pattern on Advanced High Penetration Mixer

In summary, flow visualization studies showed strong three-dimensional boundary layer effects for the high penetration mixer models as a result of the lobe-induced surface pressure field. The process of boundary layer growth under varying streamwise pressure gradients and spanwise skewing by virtue of varying spanwise pressure gradients requires the use of computational procedures to establish exit plane characteristics. As will be shown, prediction of exit plane displacement thickness distributions is needed to obtain accurate estimates of the circulation and vorticity field shed from mixer trailing edge.

4. Approximate Analysis

An approximate one-dimensional, inviscid analysis based on flow continuity has been applied to arrive at conclusions regarding scaling and geometry effects on the mixer lobe exit plane transverse velocity field and circulation. Using this analysis, calculations for sinusoidal and parallel-sided lobe geometries employed in the present experimental study are given in Appendix E and the results applied in the following sections to assist interpretation of the experimental data. The analysis treats only straight-ramped, planar lobe configurations such as the two sinusoidal mixers and one lobe of the advanced high penetration mixer.

The basis for the analysis is that the increasing axial mass flux within a lobe, above a line $y = \text{constant}$, caused by lobe growth in the axial direction, is made up by an equal transverse mass flux. Thus if v and U_∞ are the transverse and axial velocities, respectively, and dA_H/dx and dA_V/dx are the rates of change of areas in the horizontal and vertical planes, respectively, then:

$$V \frac{dA_H}{dx} = U_\infty \frac{dA_V}{dx} \quad (6)$$

As shown in Appendix E, this expression permits determination of v as function of x and y for a prescribed finite amplitude mixer $y=f(x,z)$ and by integration about a contour at the exit plane, an estimate of mixer exit circulation, Γ . These inviscid results, by virtue of the one-dimensional assumption, are necessarily approximate, however, they prove useful in the following discussion of mixer geometry and viscous effects.

5. Low Penetration Sinusoidal Mixer

Approach Boundary Layer Documentation - Hot wire anemometry was employed to define the characteristics of the boundary layer approaching the lobe region of the test model. A survey was taken in the transverse direction on tunnel centerline at an axial position 4.33 from the leading edge of the model. This position corresponds to the transition location between the upstream flat plate approach section and the downstream three-dimensional contoured lobe region. Measured boundary layer characteristics (Table D.4) at this location (normalized by 2.54 cm) were: displacement thickness, $\delta^* = 0.024$, momentum thickness, $\theta = 0.017$, 99% boundary layer thickness, $\delta = 0.145$, and shape factor, $H = 1.41$. The measured boundary layer thickness of 0.145 was close to the value of 0.127 calculated for a zero pressure gradient turbulent boundary layer growing from the plate leading edge.

The measured shape factor was in good agreement (approximately 3% lower) with the value which applies to zero pressure gradient boundary layers at the test momentum thickness Reynolds number of $Re_\theta = 970$ (Reference 15). From these measurements it is concluded that normal turbulent boundary layer flow approach conditions were obtained.

Axial Velocity Field - At the mixer exit station located just downstream of the mixer trailing edge ($\bar{x} = 0.36$), the velocity field is categorized by regions of inviscid (near reference velocity) flow and viscously affected (retarded) flow. As shown in the contour plot of Figure 24, inviscid flow exists at distances removed from the lobe exit surface and retarded flow

occurs near the outside lobe surface and within the bulk of the interior portion of the lobe peak. Specifically, the $U/U_\infty = 0.99$ contour demonstrates that measureable viscous retardation effects within the lobe extend from the lobe peak ($z = 0, y = 0.5$) to the mixer centerline ($y = 0$).

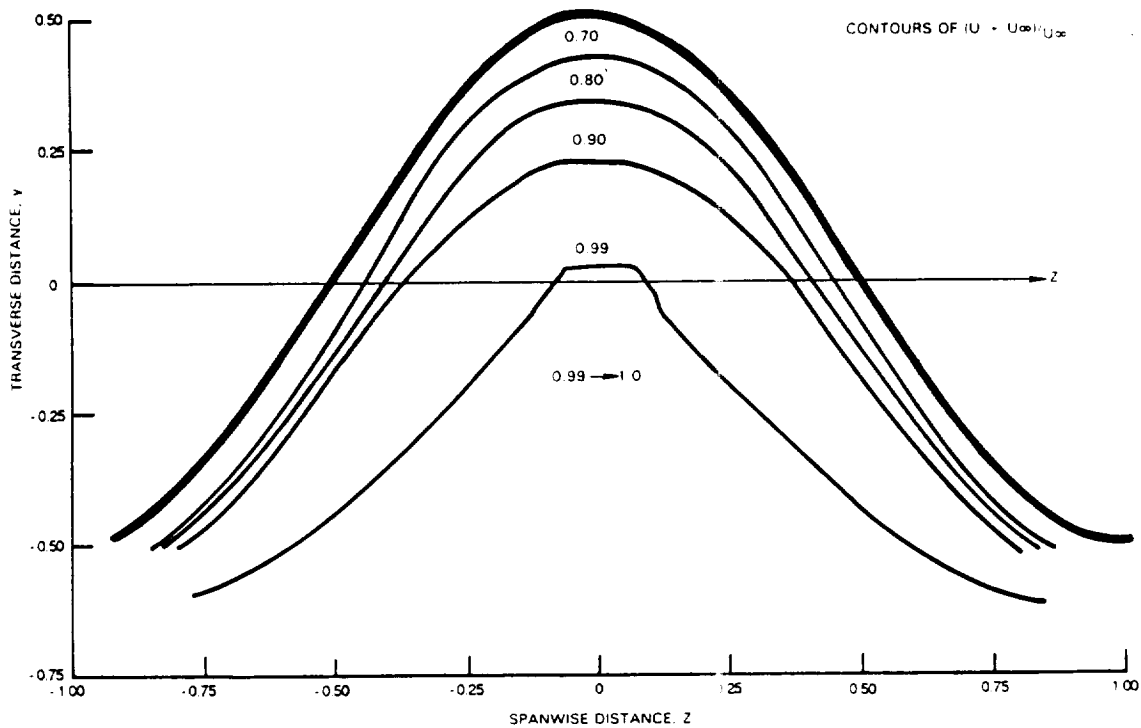


Figure 24 Contour Plot of Axial Velocity Field at Trailing Edge of Low Penetration Sinusoidal Mixer

More specifically, Table D.4 shows that within the interior of the lobe, ζ^* and δ were 0.087 and 0.48, respectively, as measured along the line $z = 0$ relative to the lobe peak ($y = 0.5$). The δ^* measurement can be interpreted as a blockage in the lobe interior peak region which effectively reduced the nominal (geometric) lobe penetration from 0.5 to 0.41, or to 83% of its nominal value. The deleterious effect of this blockage on transverse velocity component magnitude is discussed subsequently.

As indicated by Table D.4, the boundary layer in the outer flow above the lobe peak along the same $z = 0$ line was approximately a factor of three smaller than that measured within the lobe ($\delta = 0.15$ as opposed to $\delta = 0.48$). This significantly lower value is consistent with the previous discussion of flow visualization results and lateral pressure gradients. In the outer flow, the boundary layer along the peak surface is driven sideways and downward toward the trough by the imposed inviscid pressure gradient field and consequently thinned. The opposite effect occurs within the lobe interior where pressure gradients cause boundary layer fluid migration toward the peak region. Viscous retardation in the peak region is further aggravated by the narrowing of the sinusoidal lobe waveform with increased distance, y . Fluid migration and peak narrowing cause merging of the viscous layers from both sides of the lobe on the lobe centerline ($z = 0$). The following section presents related exit plane total pressure results.

Total Pressure Field - Normalized total pressure contours given in Figure 25 confirm the previously presented axial velocity results regarding the existence of significant viscous effects within the interior of the lobe and near the lobe surface. Using the 0.99 contour as an indicator of the dividing line between inviscid and viscous regions, it is seen that viscous effects extend throughout the region bounded by the lobe surface and the mixer centerline ($y = 0$). Low total pressures in the peak of the lobe indicate that viscous effects dominate this region, thereby contributing to blockage.

In summary, both axial velocity component and total pressure data indicate significant viscous retardation effects for this model. Subsequent sections will discuss implications of these findings relative to the magnitude of the transverse velocity component, lobe exit plane circulation and preferred mixer lobe geometries.

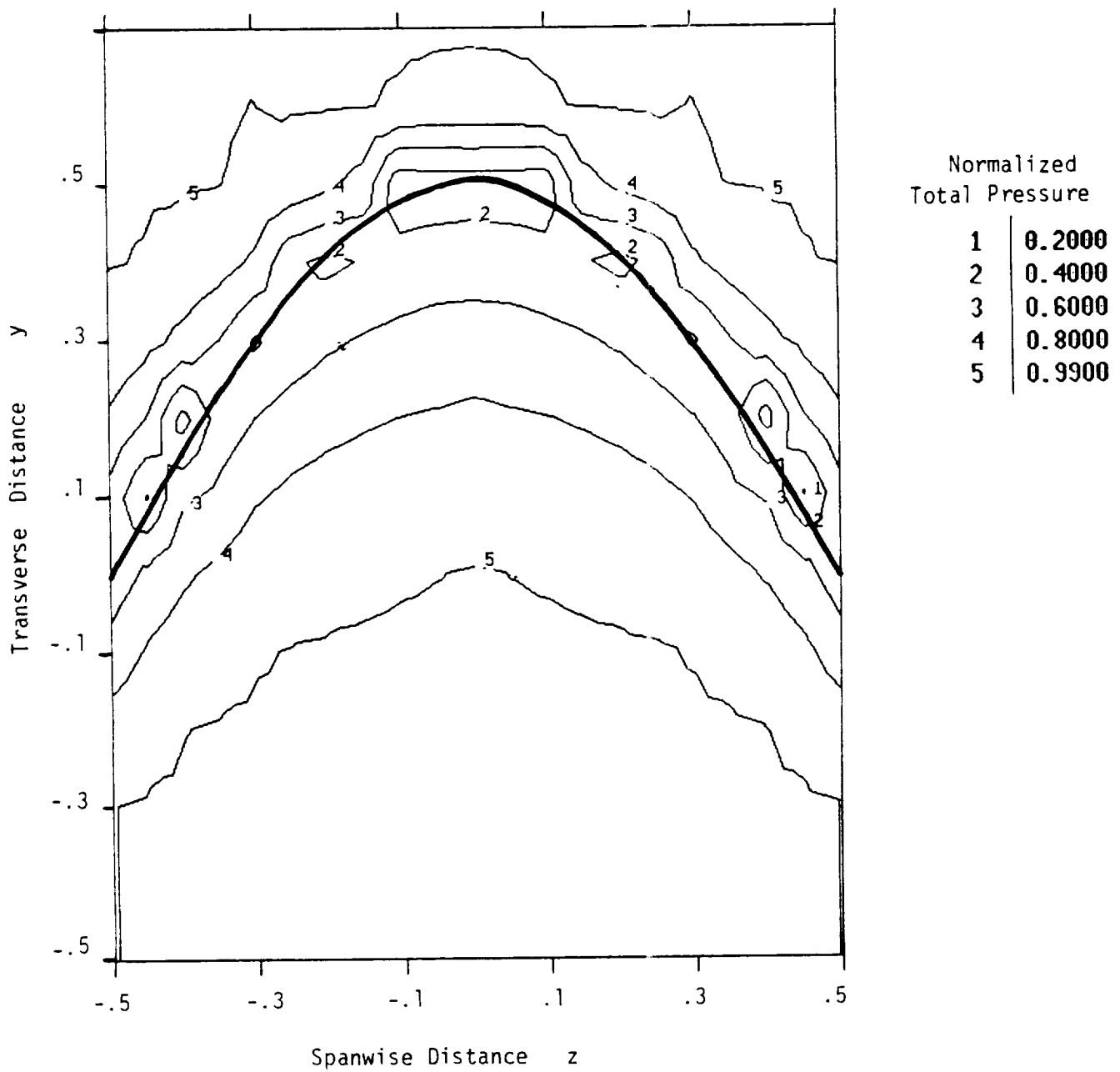


Figure 25 Contour Plot of Normalized Total Pressure Field at Lobe Trailing Edge of Low Penetration Lobed Mixer

Transverse Velocity Field - At the mixer exit station the transverse velocity component data indicate a general cross-stream (vertical) flow as would be anticipated in response to the vertical penetration of the lobe contour into the stream. Considering the symmetrical lobe segment extending from $z = 0$ to $z = .5$, velocities are upward within the interior of the lobe ($y < 0.5 \cos \pi z$) and generally downward outside the lobe ($y > 0.5 \cos \pi z$). As shown in the contour plot of Figure 26 and Table D.1.2, the greatest transverse velocity components (those in the range from 7 to 8.7% of U_∞) are directed upward and occur within the upper half ($y \geq 0$) of the interior of the lobe. Values of this magnitude extend across the lobe (from $z = 0$ to $z = .4$) with lower values obtained near the lobe surface at all values of z . Contained within this contour is a smaller region in the central portion of the half-lobe where maximum values in the range from 8 to 8.7% of U_∞ are obtained. Outside these contours, values decay to negligible levels as distance from the lobe surface increases.

Examination of the transverse velocity component magnitude variation with y provides insight into overall lobe flowfield development and for this purpose the $z = 0$ line centered on the lobe peak has been selected. As shown in Figure 27, a maximum value for v of 8.5 % U_∞ is obtained inside the peak at a y value of 0.3. Values decrease gradually with increasing distance from the lobe peak with finite values of several percent obtained below the mixer ($y < 0.5$). The rate of decay of the component in the opposite direction ($y > 0.3$) is much more rapid with near zero values achieved at $y \geq 0.6$.

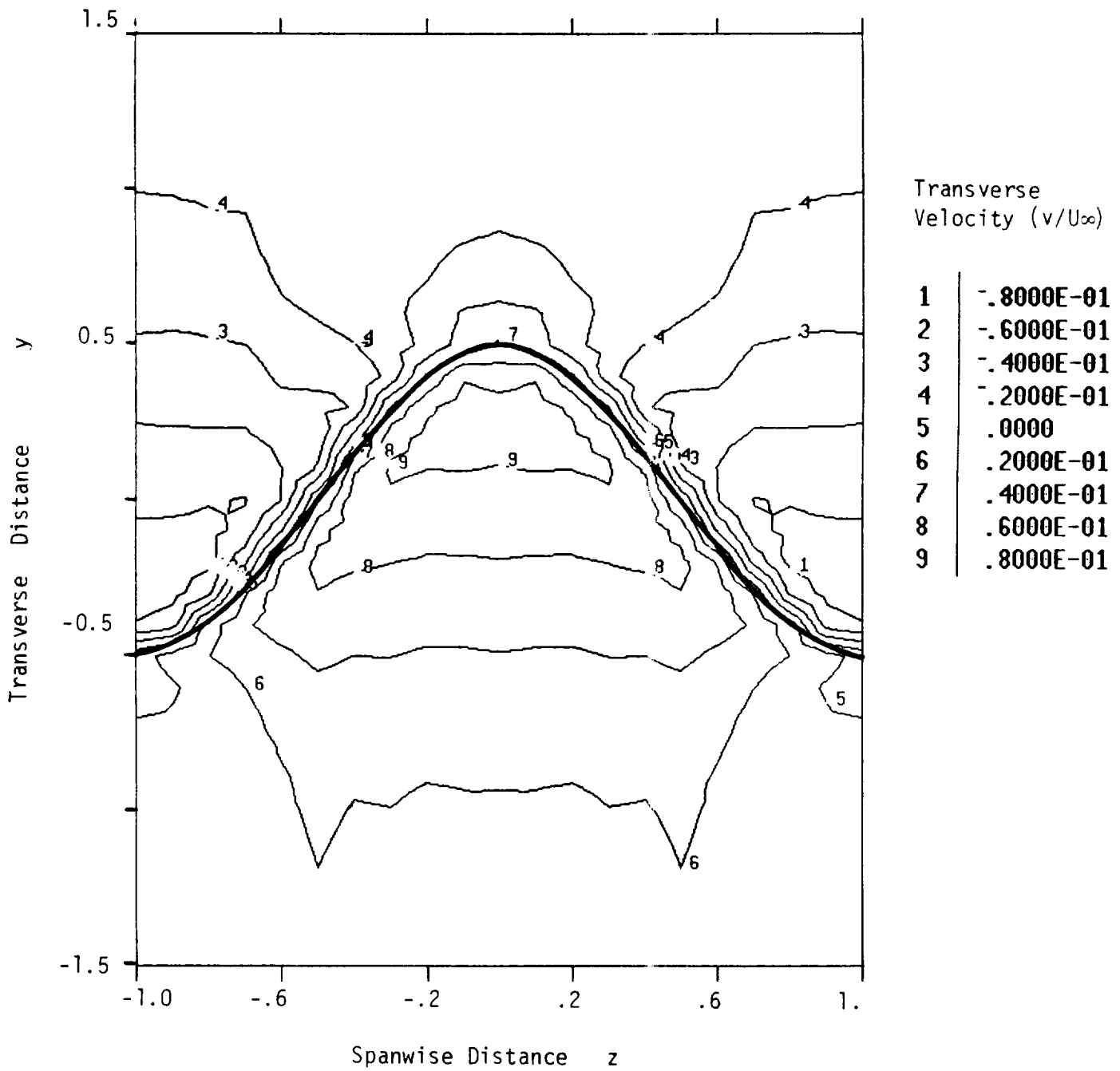


Figure 26 Contour Plot of Transverse Velocity Field at Trailing Edge of Low Penetration Lobed Mixer

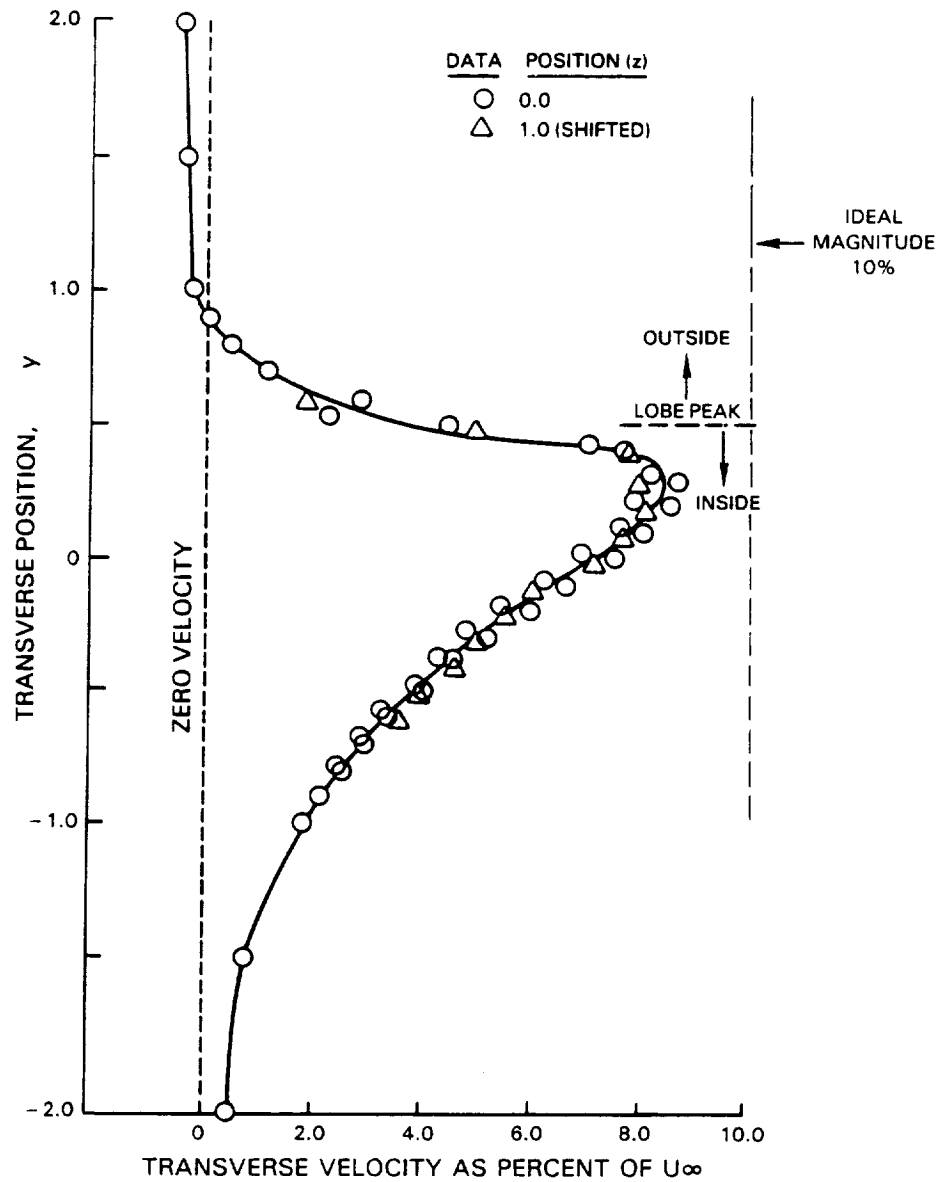


Figure 27 Low Penetration Mixer, Transverse Velocity Component ($v/U_\infty \times 100$)

Also shown in Figure 27 is the degree of symmetry achieved in the experiment. Circular and triangular symbols show results obtained at $z = 0$ and $z = 1$, respectively. The $z=1$ velocity and position data have been changed in sign to permit them to be overlaid onto the $z=0$ data. For this symmetrical model, data at these two locations should be identical. This symmetry is observed to be true within the error band estimated to be less than one percent of the reference velocity. Of particular importance is that the vertical component did not achieve its ideal maximum value based on lobe geometry. For an inviscid flow and straight-ramped lobes such as considered here, the velocity vector at the lobe peak should be parallel to ramp slope. Based on the lobe peak ramp angle (turning angle) of $\epsilon = 5.7^\circ$ and an axial velocity equal to the upstream reference velocity, U_∞ , the ideal transverse component magnitude at the mixer exit should be $U_\infty \tan \epsilon$ or $0.1 U_\infty$. As a percentage of this ideal value, the maximum magnitude achieved was only 85%. This degradation is attributed to boundary layer blockage in the lobe peak region which effectively reduced lobe penetration. It is important to note that this value of 85% is in close agreement with the 83% effective lobe penetration calculated in the previous section from boundary layer displacement thickness.

Other comparisons to inviscid behavior can be made. Following the calculation procedure described in the above section, "Approximate Analysis", it is shown in Appendix E that transverse velocity magnitude should be given by:

$$v = U \tan \epsilon \sqrt{\frac{1 - (y/h)^2}{\text{arc cos } (y/h)}} \quad (6)$$

where h is the sinusoidal amplitude (one-half peak-to-peak), or 0.5 for the low penetration model. This relation is shown as a dashed line in Figure 27 and as noted above, the maximum value of $0.1 U_\infty$ is not achieved at $y = 0.5$. The predicted decay with increasing distance from the lobe peak is observed in the data, but contrary to analysis, non-zero components are measured at values of y less than 0.5.

In summary, the transverse velocity component measurements for the low penetration sinusoidal mixer follow overall expected trends based on inviscid analysis. Maximum values, however, are only 85% of ideal and this is attributed to blockage in the lobe peak region caused by boundary layer convection and growth within the lobes.

Spanwise Velocity Field - As in the case of the transverse component, the spanwise velocity field at the mixer exit station displays cross-stream motions in response to the penetration of the lobe contour into the stream. In contrast with the transverse components, the spanwise component magnitudes are small, reaching values of only several percent U_∞ in the vicinity of the lobe surface. This general behavior is displayed in Figure 28 where spanwise component vectors are plotted in terms of percent U_∞ . Near zero values are obtained along the line $z = 0$ as expected based on symmetry arguments.

It can be inferred that the variation of spanwise component magnitude with y , exterior to the lobe and in the vicinity of the lobe surface, is such that the vector sum of w and v is parallel to the surface tangent. This tangency condition is consistent with the data which shows maximum values outside the lobe peak and decreasing values toward mixer centerline. In summary, spanwise

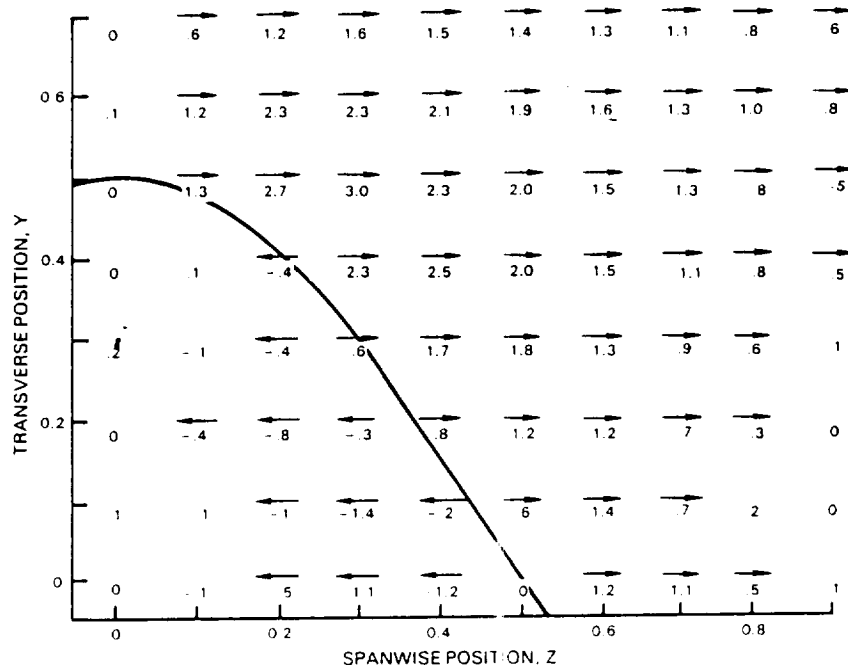


Figure 28 Low Penetration Mixer, Spanwise Velocity Field ($w/U_\infty \times 100$)

velocity measurements indicate that while maximum values can reach levels as high as 34% of the maximum transverse component level, this component of the secondary flow vector field is generally much weaker than the transverse component.

Combined Transverse-Spanwise Velocity Field - Figure 29 is a vector plot of the low penetration model lobe exit secondary velocity field measured at a position just downstream ($\bar{x} = 0.36$) of the lobe trailing edge. The existence of two counter-rotating axial vortices within the single lobe segment is clearly evident. The much higher density of measurements and greater measurement accuracy provide a much improved definition of the lobe-induced circulations relative to the previous mixer study conducted by Paterson (Reference 4), using LDV techniques. The circulation associated with these vortices will be presented in the section, "Circulation Calculations".

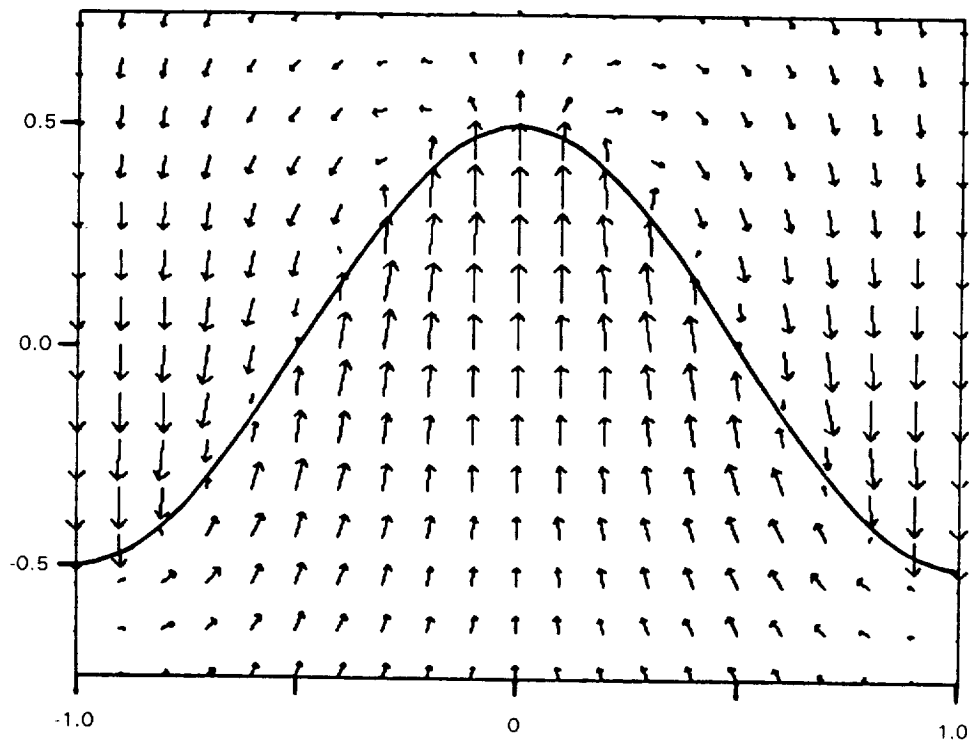


Figure 29 Low Penetration Sinusoidal Mixer Exit Plane Secondary Velocity Field

6. High Penetration Sinusoidal Mixer

Approach Boundary Layer Documentation - Hot wire anemometry was used to define the characteristics of the boundary layer approaching the lobe region of the model. The survey was taken at the same location as that used for the low penetration model, i.e. 4.33 from the leading edge at the junction of the flat plate and lobe regions. Measured boundary layer characteristics at this location are given in Table D.4 and are observed to be about 60% larger than those obtained with the low penetration model. This difference is attributed to a thicker turbulent trip in the leading edge region. The shape factor of 1.39 is reasonable being within 4% of the zero pressure gradient value for this momentum Reynolds number (Reference 15). When compared to the factor of

four increase in lobe height for this model, this 60% larger boundary layer thickness resulted in a thinner relative approach boundary layer for the high penetration model.

Axial Velocity Field - As in the case of the low penetration model, the axial velocity distribution at the mixer exit plane ($\bar{x}=0.36$) displays regions of basically inviscid flow and viscously retarded flow, with the greatest retardation within the peak lobe region and near the mixer surface. Figure 30 shows these results in a contour plot format. A comparison of the two models is shown in Figure 31 where normalized axial velocity is plotted as the abscissa and transverse position normalized by mixer amplitude, h , as ordinate. Two features are evident. First, the boundary layer on the outside surface of the lobe is thinner for the high penetration model. Secondly, the retarded region within the interior of the high penetration mixer (as indicated by $u/U_\infty \leq 0.99$) is confined to the upper half of the lobe. This behavior differs from the low penetration case where the retarded region extended from the lobe peak to mixer centerline ($y=0$). These two features appear to be consistent with the greater skewing (vertical displacement) of lobe surface boundary layers for the high penetration model noted in the previously discussed flow visualization results.

A comparison of boundary layer characteristics for the two mixers along the line $z=0$ is given in Table D.4. High penetration values are a factor 2.5 to 2.9 larger in physical distance but smaller when normalized by lobe amplitude. Interpreting the δ^* measurement as a blockage in the lobe interior peak region, boundary layer buildup reduced the nominal (geometric) lobe penetration from 2.0 to 1.77 or to 88% of its nominal value. As indicated by

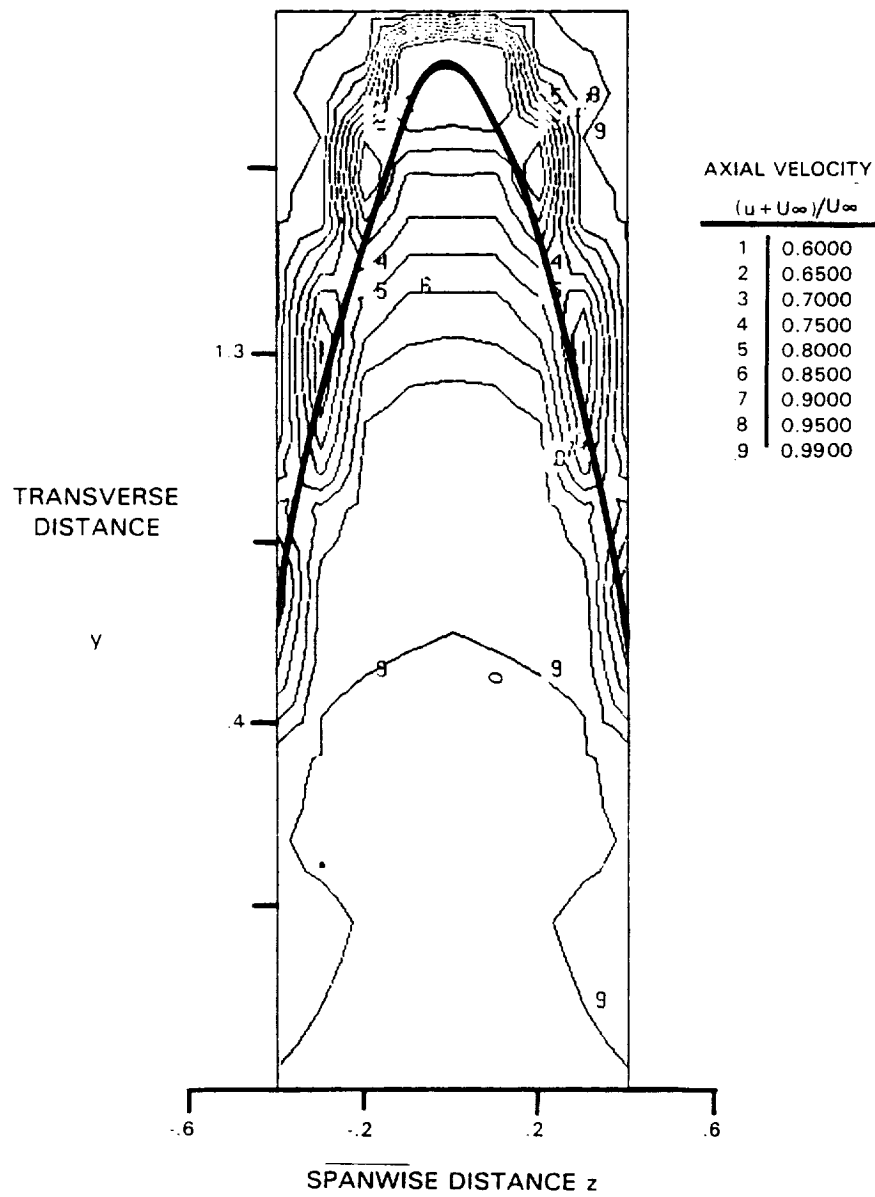


Figure 30 Contour Plot of Axial Velocity Field at Trailing Edge of High Penetration Lobed Mixer

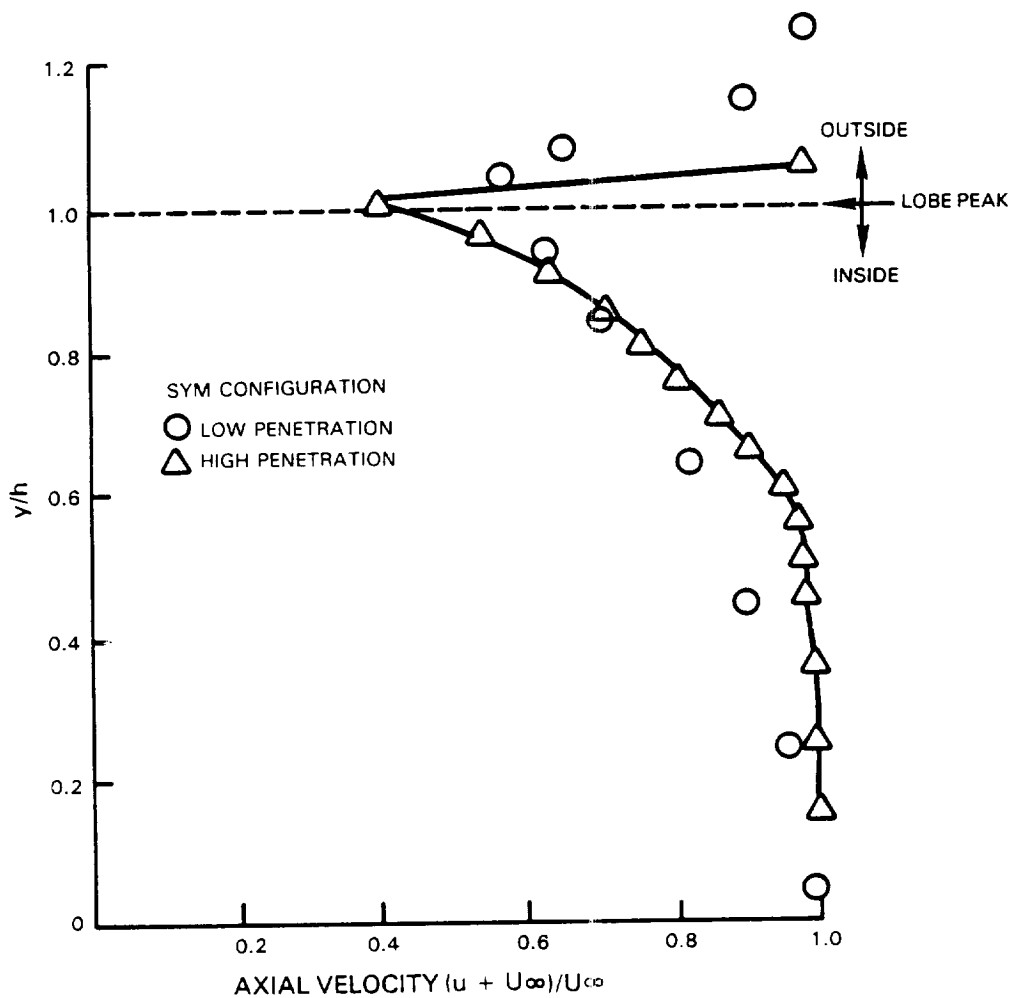


Figure 31 Comparison of Lobe Crest ($z = 0$) Axial Velocity, Components for Low and High Penetration Sinusoidal Mixers

Table D.4, the boundary layer in the outer flow above the lobe peak along the same line, $z=0$, was approximately a factor of twelve smaller than that measured within the lobe. This ratio is four times larger than that of the low penetration model and is believed to reflect higher lateral and transverse pressure gradients associated with the steeper lobe ramp angle. The resultant stronger convection of lobe boundary layer fluid to the peaks and troughs of the high penetration model would be expected to both accelerate thinning of the external surface boundary layer and collection of low axial momentum fluid within the lobe peak region. The following section presents related exit plane total pressure results.

Total Pressure Field - Normalized total pressure contours given in Figure 32 confirm the previously presented axial velocity results which showed low axial velocity fluid was concentrated in the upper half of the interior of the lobe. Specifically, the 0.99 contour intersects lobe centerline ($z=0$) at 60% of the lobe amplitude. This contrasts with low penetration results where viscous effects extended to mixer centerline ($y=0$).

In summary, both axial velocity component and total pressure data indicate significant but similar viscous retardation effects for this model than for the low penetration model when results are normalized by lobe amplitude. These retardation effects are considered in the next section relative to the transverse velocity field development.

Transverse Velocity Field - As expected, transverse velocity components for the high penetration model were substantially larger than for the low penetration model, but displayed the same general character as shown in the contour plot of Figure 33 and Table D.2.2. Considering the symmetrical lobe segment extending from $z=0$ to $z=0.5$, velocities are upward within the interior of the lobe ($y < 2 \cos \pi z$) and generally downward outside the lobe ($y > 2 \cos \pi z$). The greatest transverse velocity components (those in the range from 26 to 33% of U_∞) are directed upward and occur within the upper half ($y \geq 0$) of the interior of the lobe. Values of this magnitude extend across the lobe (from $z=0$ to $z=0.3$) with lower values obtained near the lobe surface at all values of z . Contained within this contour is a smaller region

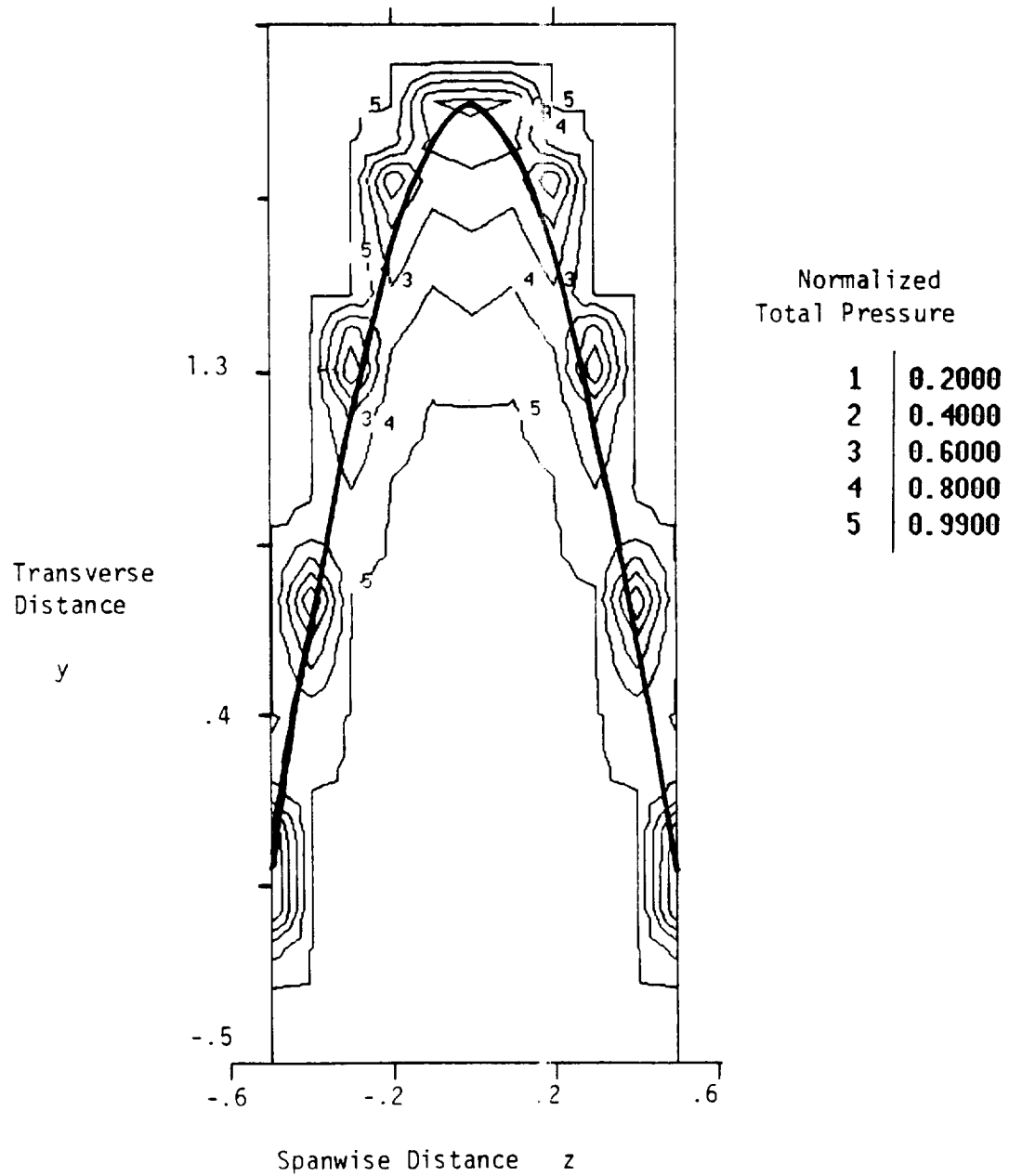


Figure 32 Contour Plot of Normalized Total Pressure Field at Lobe Trailing Edge for High Penetration Loaded Mixer

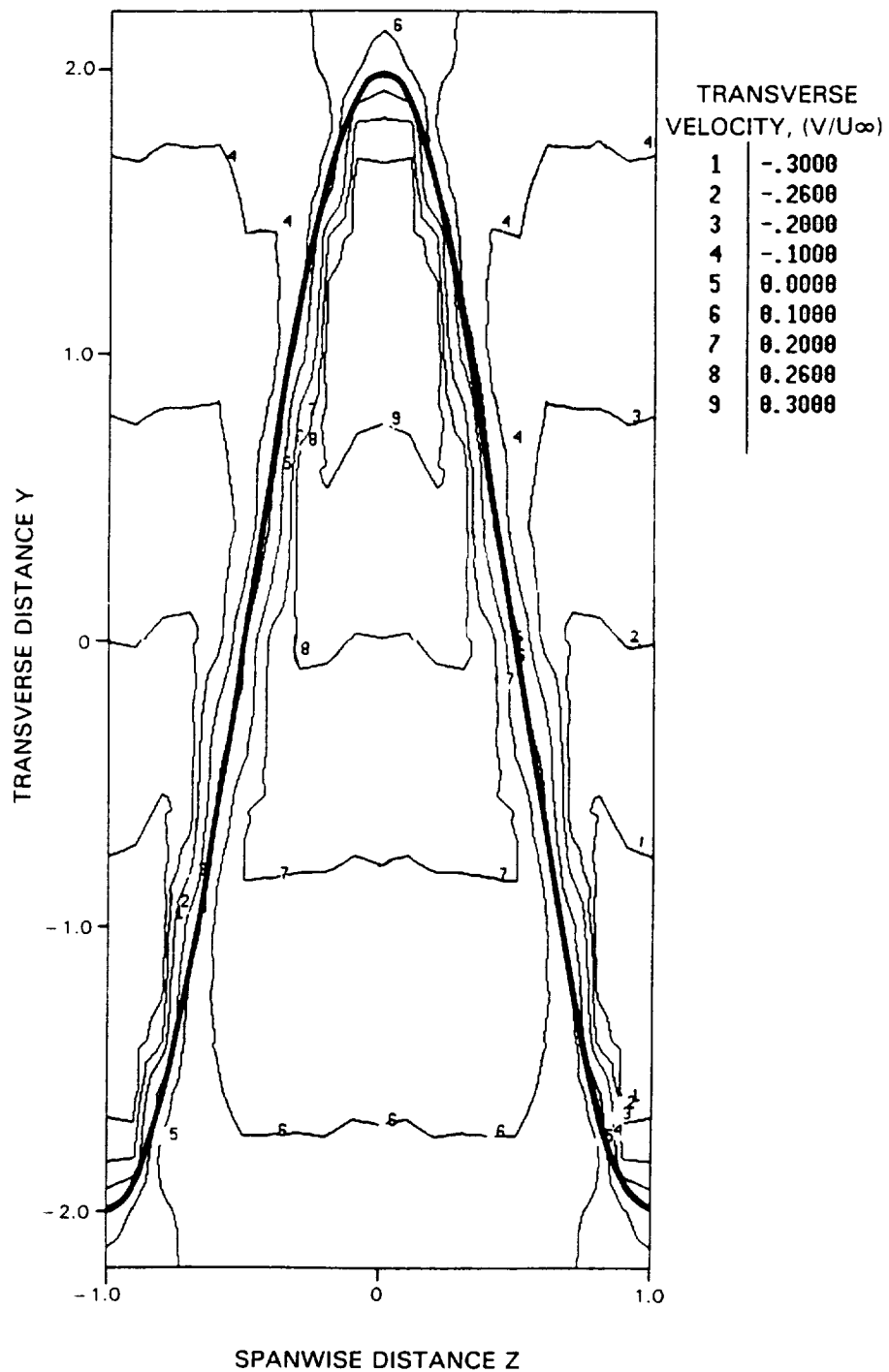


Figure 33 Contour Plot of Transverse Velocity Field at Trailing Edge of High Penetration Lobed Mixer

in the central portion of the half lobe where maximum values in the range from 30 to 33% of U_∞ are obtained. Outside these contours, values decay to negligible levels as distance from the lobe surface increases. The above described behavior is generally similar to that obtained with the low penetration model except that magnitudes are about a factor of four larger, the same ratio as the ratio of high-to-low penetration model amplitude. This is examined in more detail below.

As in the case of the low penetration model, the vertical component did not achieve its ideal maximum value. Based on the lobe peak ramp angle of $\epsilon = 22^\circ$, the ideal transverse component magnitude at the mixer exit would be $U_\infty \tan \epsilon$ or $0.4 U_\infty$. The measured maximum value of $0.33 U_\infty$ represents 83% of ideal. This is close to the 88% effective penetration calculated above based on displacement thickness buildup in the peak region. It is also close to low penetration mixer results where the measured maximum transverse component was 85% of the ideal value. These two data sets therefore provide a consistent explanation of the role of boundary layer blockage in the reduction of exit plane secondary flow velocity magnitude.

Transverse velocity magnitudes for the two mixers along lobe centerline are compared in Figure 34 using $v/U_\infty \tan \epsilon$ as the normalized ordinate and (y/h) as the normalized abscissa, as suggested by the ideal analysis (Equation 7). It is seen that this scaling collapses the low and high penetration data reasonably well. Whereas non-normalized velocities for the two mixers at the same y/h value typically differed by factors on the order of four, the normalized

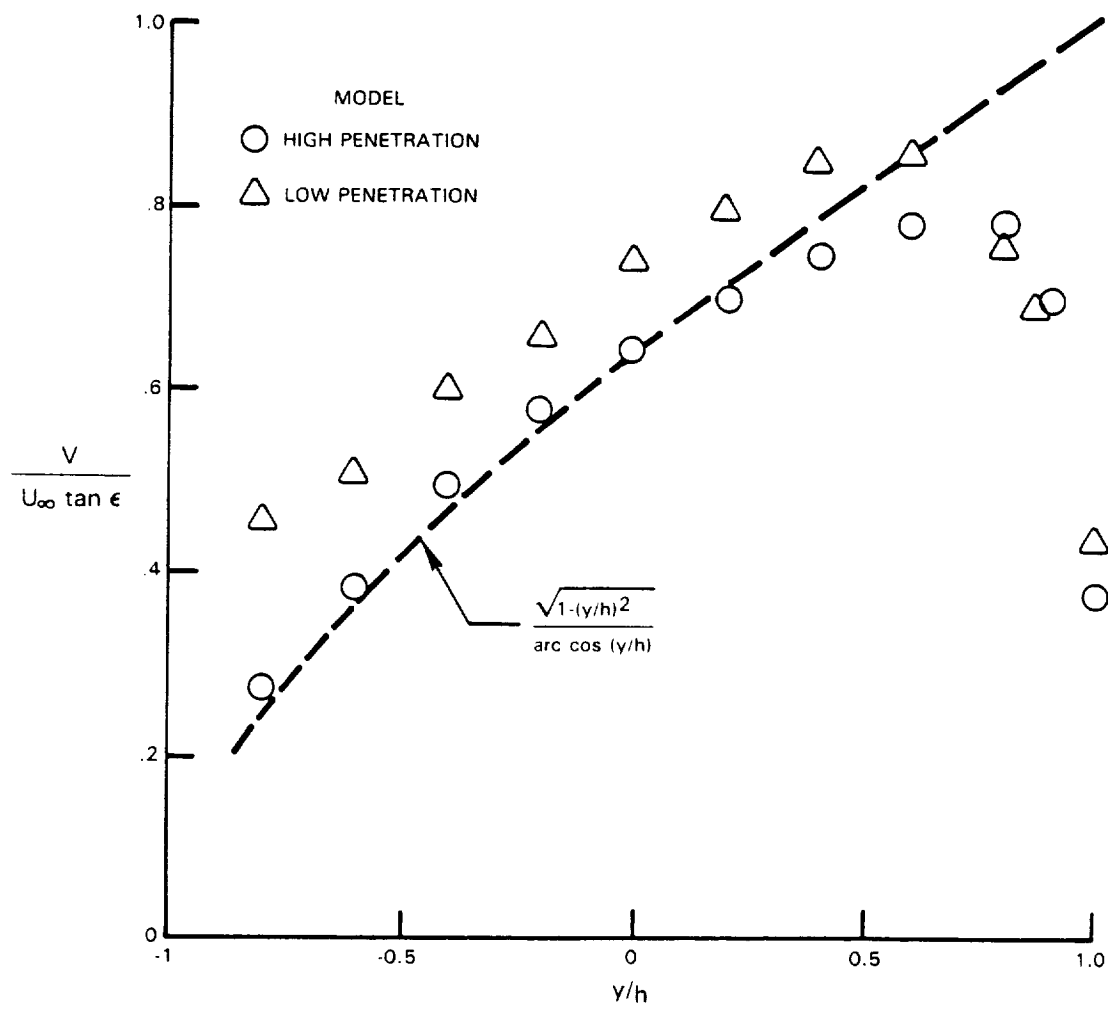


Figure 34 Comparison of High and Low Penetration Sinusoidal Mixer Transverse Velocity Components

results display differences of less than 20% except at low y/h . The dashed line in Figure 34 shows the equation (7) ideal result and this is in reasonable agreement with the data (particularly the high penetration data) except at large y/h where the previously discussed boundary layer blockage effects dominate.

In summary, transverse velocity fields for the two geometrically similar mixers are found also to be similar and with the exception of the viscously dominated lobe peak region, in reasonable agreement with approximate inviscid calculations.

Spanwise Velocity Field - Spanwise velocity components for the high penetration mixer display the same general pattern as the low penetration model. This is shown in Figure 35. Magnitudes are larger for this model, although the maximum value of $10.8\% U_\infty$ was a factor of three smaller than the maximum transverse component of $33\% U_\infty$. It can be seen that the larger values, in the 5 to 10% U_∞ range, occupy only a small region outside the lobe peak. The majority of the lobe region is characterized by spanwise components of a few percent U_∞ .

Based on the linear mixer model analysis, spanwise components should scale directly with lobe height for geometrically similar models. This is found to be approximately true in that the maximum spanwise component for the high penetration model was 3.6 times greater than the maximum value for the low penetration model. Exact correspondence would occur at a ratio of four.

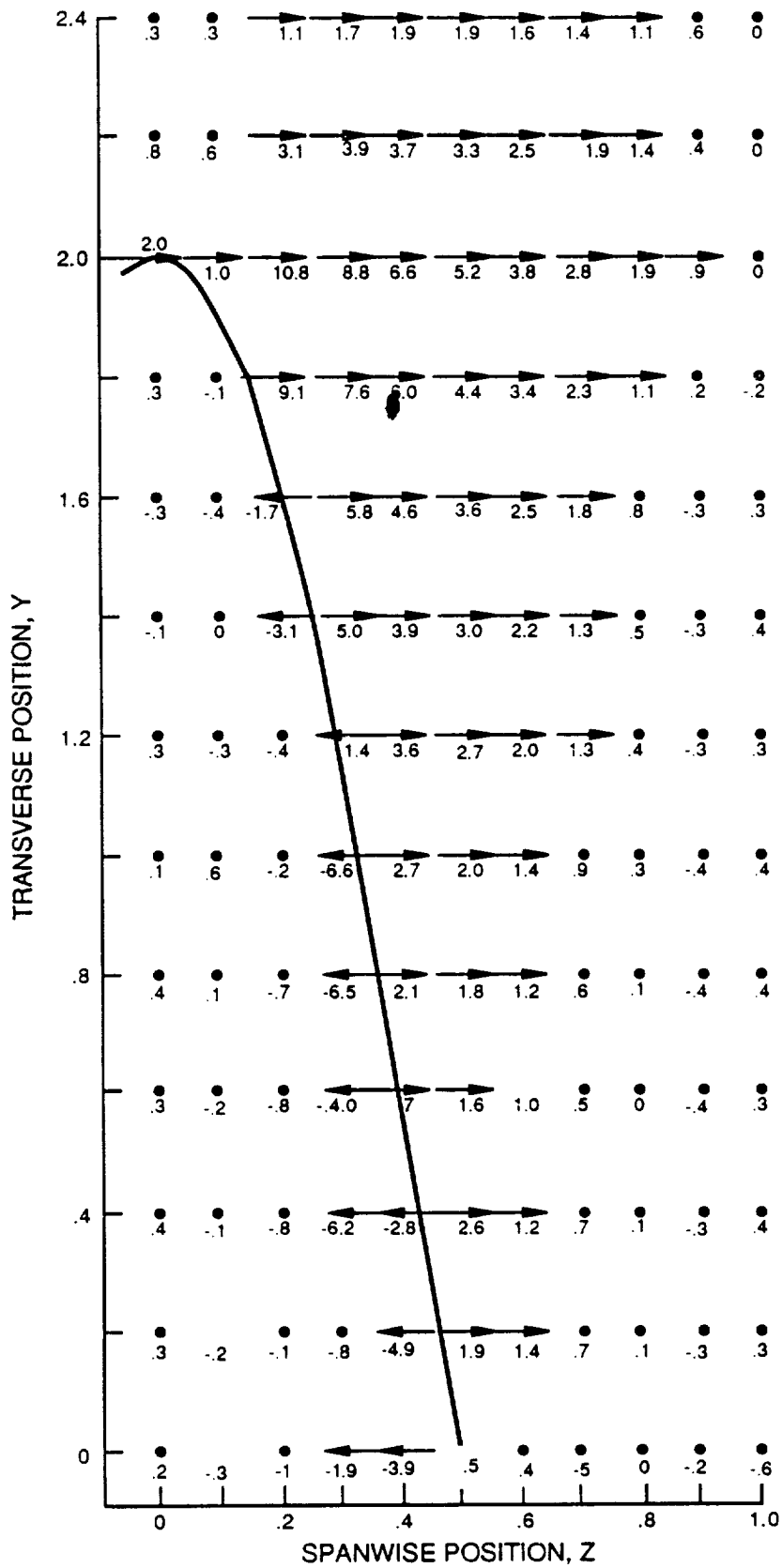


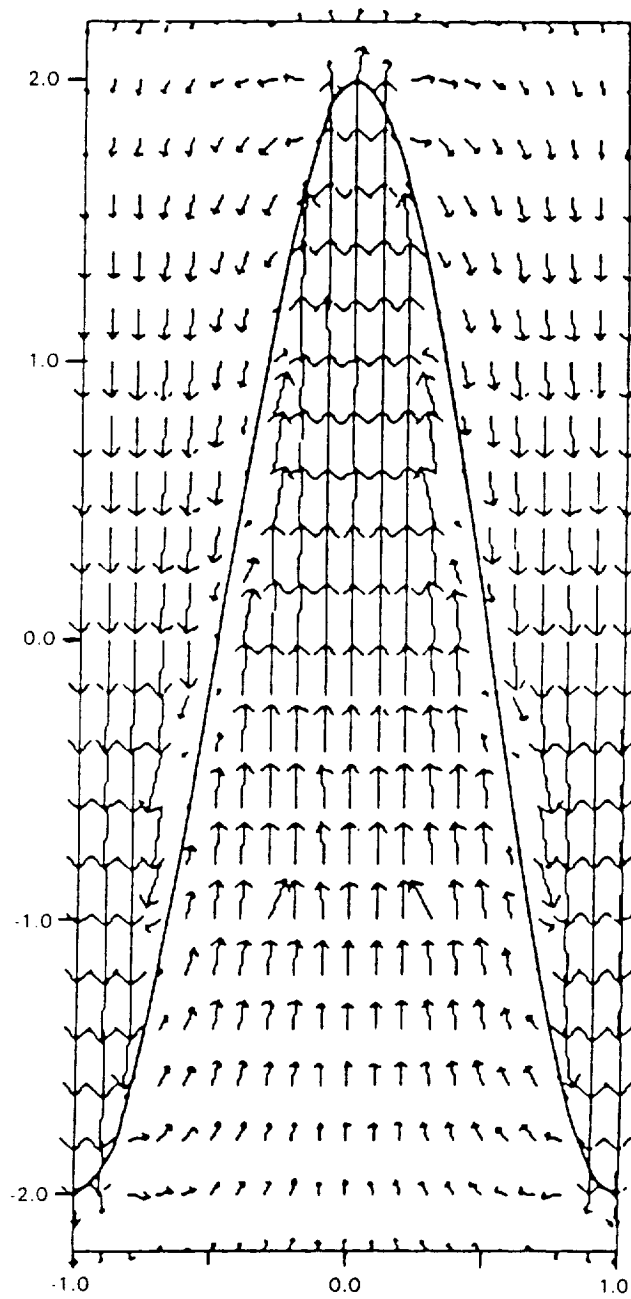
Figure 35 High Penetration Sinusoidal Mixer, Spanwise Velocity Field ($w/U_\infty \times 100$)

The summary conclusion is similar to the low penetration result: the spanwise component of the secondary flow velocity field is much weaker than the transverse component. Magnitudes appear to be governed by the non-parallel lobe surfaces which impose a tangency condition on the sum of the transverse and spanwise vectors. That is, the lobe ramp angle sets the transverse velocity magnitude and the spanwise component adjusts to satisfy the surface tangency condition.

Combined Transverse - Spanwise Velocity Field - The high penetration sinusoidal model lobe exit secondary flow pattern shown in Figure 36 is generally similar to the low penetration pattern previously presented for the same location ($\bar{x}=0.36$) downstream of the trailing edge. This similarity would be expected based on the foregoing sections which demonstrated that velocity magnitudes scale directly with ramp angle for geometrically similar straight-ramped mixers. The resultant vortex circulation is presented in the section, "Circulation Calculations".

7. Advanced High Penetration Mixer

Approach Boundary Layer Documentation - As in the case of the sinusoidal models, hot wire anemometry was used to define the boundary layer approaching the lobe region of the model. The surveys were taken on the upper and lower surfaces at a distance of 4.4 from the leading edge. This is the same distance used for the sinusoidal models but in this case not coincident with the lobe formation location which occurred at a distance of 12.5.



HIGH PENETRATION SINUSOIDAL MIXER

Figure 36 High Penetration Sinusoidal Mixer, Exit Plane Secondary Velocity Field

Measured boundary layer parameters at this location are given in Table D.4 and are observed to be several times smaller than those for the low penetration model which had a similar turbulent trip. This boundary layer reduction is attributed to local flow acceleration in the thick (0.7) leading edge region of the model.

Axial Velocity Field - The advanced high penetration model displayed a larger region of inviscid flow within the interior of the lobes than either of the sinusoidal mixers. This behavior is evident from Figure 37 which shows that the $(u+U_\infty)/(1.49 U_\infty) = 0.99$ contour extends upward to a value of $y=0.81$ at $z=0$ and downward to $y= -0.75$ at $z=1$. (In this comparison, $1.49 U_\infty$ is used for normalization of the axial velocity component since this represents the local freestream velocity in the vicinity of the mixer trailing edge. Flow acceleration from U_∞ to $1.49 U_\infty$ was caused by the convergence of the tunnel walls). Based on lobe peak coordinates of $y=1.16$ and -1.22 at $z=0$ and 1 , respectively, the above 0.99 contour locations correspond to 70% of peak at $z=0$ and 60% of peak at $z=1$. Corresponding 0.99 contours for the low and high penetration models extended only to zero and 50%, respectively.

The proportionately greater inviscid flow region for the advanced mixer resulted in significantly greater effective penetrations. This greater effective penetration is evident from the table below where boundary layer transverse at the lobe exit plane are used to calculate displacement thickness (see Table D.4) along lobe centerlines ($z=0$ and 1). Subtracting this value from the lobe amplitude gives the effective lobe amplitude which can be expressed as a percentage of physical amplitude. This percentage is termed effective penetration.

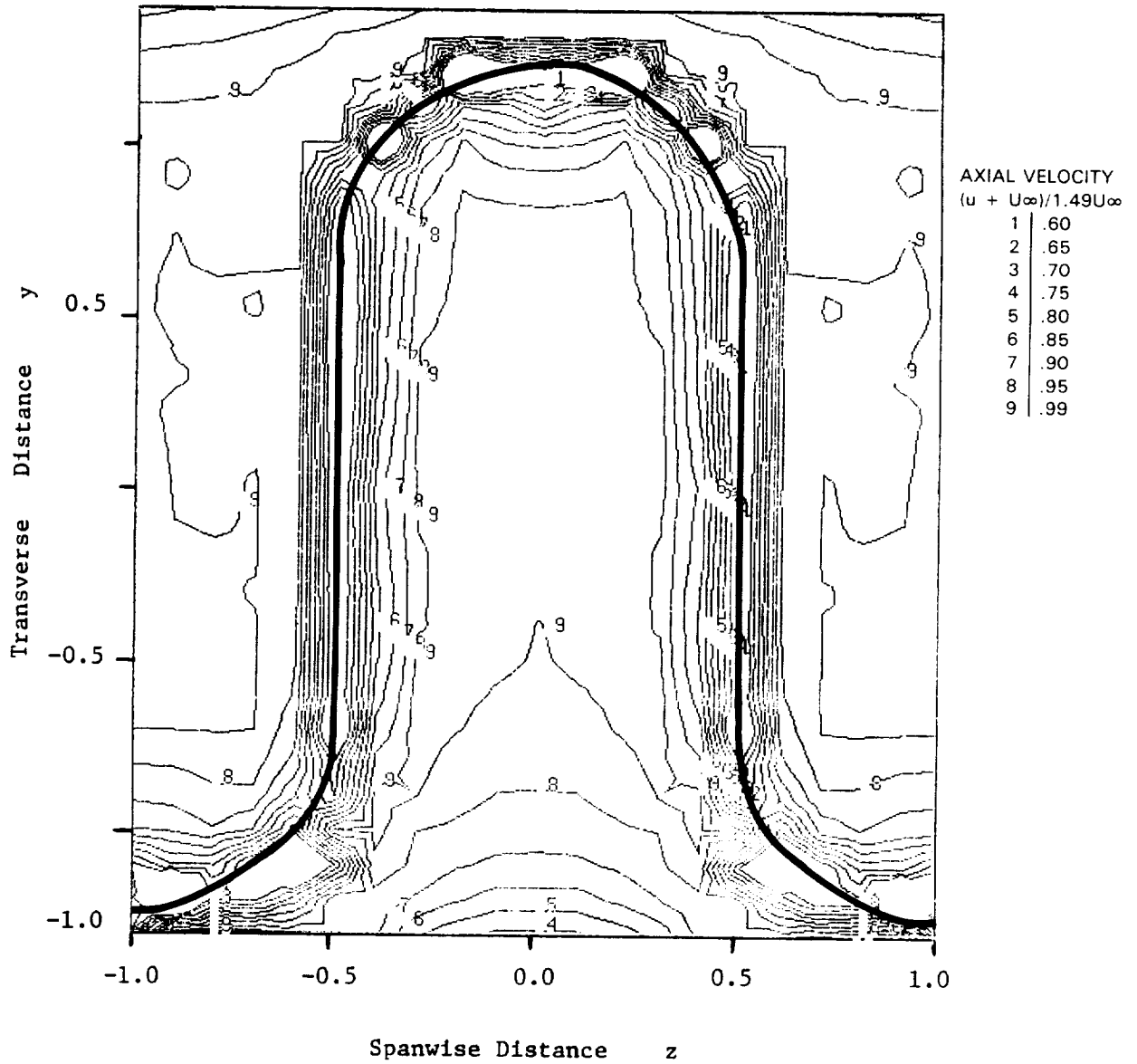


Figure 37 Contour Plot of Axial Velocity at Trailing Edge of Advanced High Penetration Lobed Mixer

Model Location	Low Penetration Sinusoidal	High Penetration Sinusoidal	Advanced High Penetration	
	$z = 0,1$	$z = 0,1$	$z=0$	$z=1$
Effective Penetration $\frac{(h-\delta^*)}{h} \times 100$	83%	88%	97%	95%

Total Pressure Field - Normalized total pressure distributions given in Table D.3.4 confirm the previously presented axial velocity results which showed inviscid flow extended further into the lobe interiors than in the case of the sinusoidal mixers. Complicating factors in these model comparisons is that the advanced mixer was three times longer than the sinusoidal mixers but was subjected to an overall favorable pressure gradient. These two factors have opposite effects on boundary layer growth. Between the axial station where the lobes began to form (Station 56.5) and the trailing edge (Station 66), however, average velocity increased by only 10% based on the tunnel area distribution. This acceleration appears to be too small to account for the significant differences noted above.

A feature not previously discussed is the boundary layer buildup on the parallel sidewalls of the mixer. Tabulated in Table D.4 are boundary layer characteristics obtained from horizontal total pressure transverses at the locations shown in Figure 38. Proceeding from bottom to top of the lobe, transverses labeled "4 IN", "3 IN" and "2 IN" yielded δ^* values of 0.011, 0.019 and 0.026 indicating a general thickening of sidewall boundary layer thickness with increasing y . Traverse "1 IN" at the lobe peak yielded the highest value of 0.041. Similar results apply to the adjacent downward facing lobe.

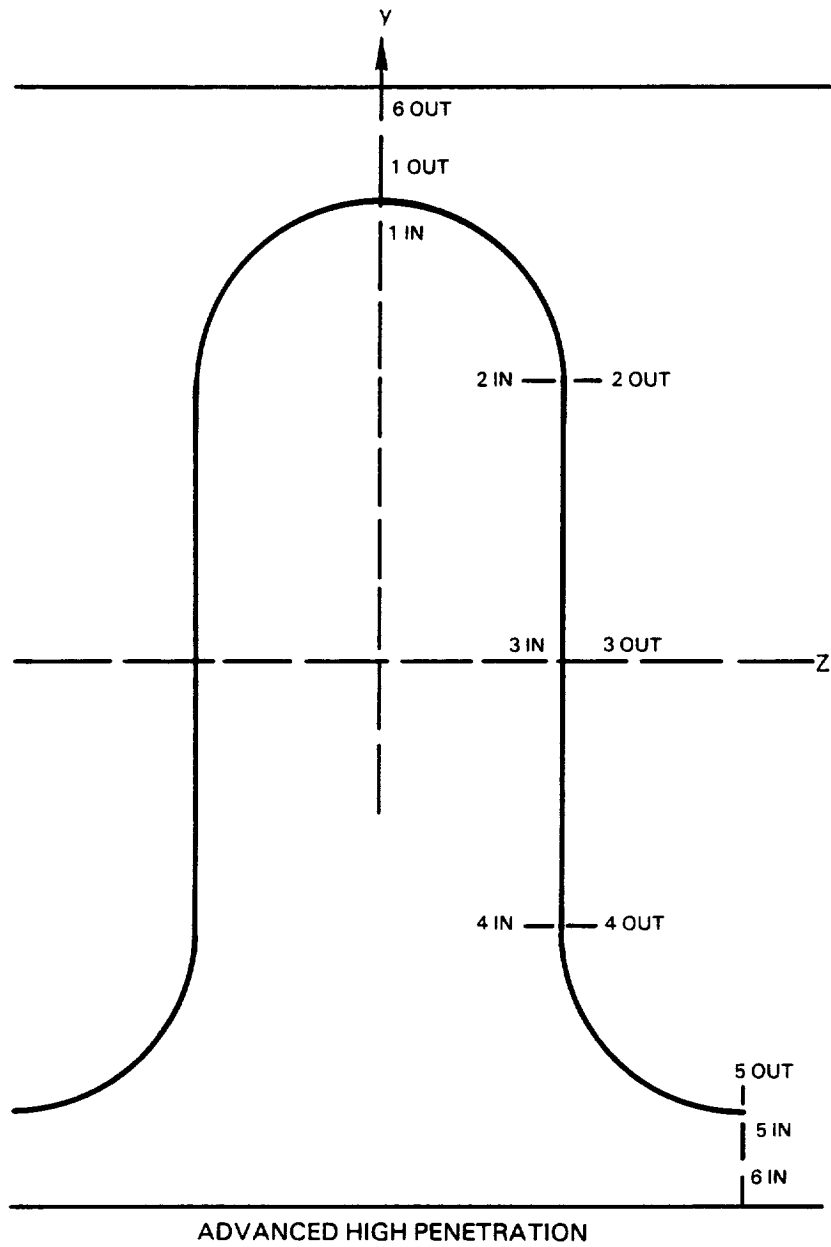


Figure 38 Advanced High Penetration Lobe Trailing Edge Boundary Layer Traverse Locations

This increase of boundary layer thickness with lobe height would be expected based on pressure gradient arguments given earlier. Both sinusoidal mixers displayed the same behavior, however in those cases, sidewall convergence, resulting in reduced lobe width with increasing y , fostered merging of opposite surface boundary layers on lobe centerline ($z=0$). This then contributed to peak region blockage and reduced effective penetration. An advantage of the parallel-sided lobe, therefore, appears to be the constant lobe width which does not contribute to boundary layer merging on lobe centerline. Stated in another manner, low momentum boundary layer fluid, driven to the peak region by inviscidly imposed pressure gradients, can distribute itself over the greater surface area of the rounded, parallel-sided lobe peak (as opposed to the more pointed sinusoidal peak) thereby reducing peak region blockage on lobe centerline ($z=0$).

In summary, axial velocity and total pressure data indicate substantially reduced viscous retardation effects for the advanced high penetration model. This will be shown in the following section to have a favorable effect on the transverse velocity component field.

Transverse Velocity Field - Transverse velocity components for the advanced mixer displayed the same general pattern as the sinusoidal models, as shown in the right portion of Figure 39, but were unsymmetrical due to the unsymmetrical lobe geometry. A significant difference between this model and the previously discussed sinusoidal models is that the transverse component magnitudes achieved near ideal values as discussed below.

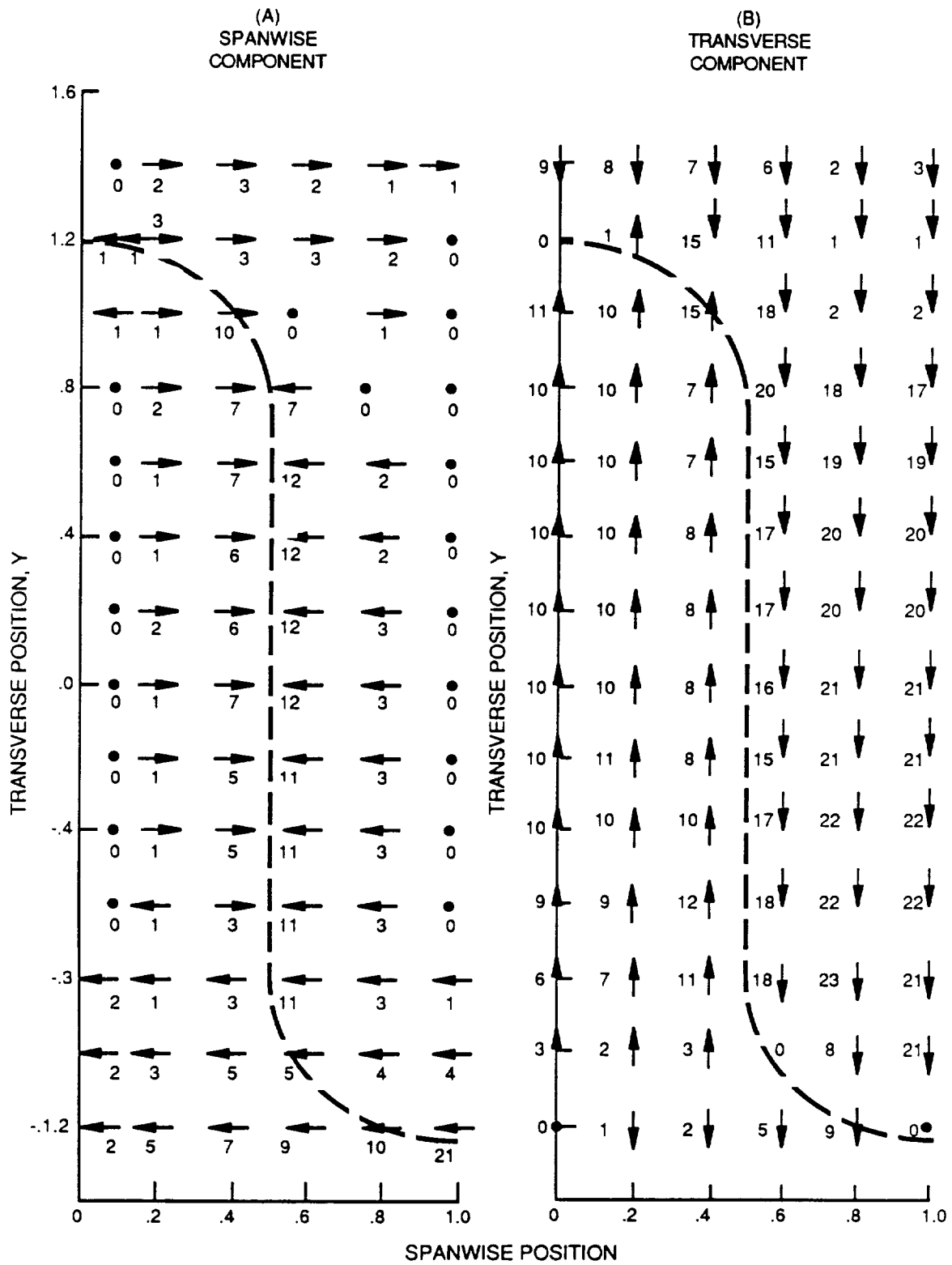


Figure 39 Advanced High Penetration Mixer Transverse and Spanwise Velocity Field

The downward penetrating lobe (trough), shown on the right of the figure was nearly a straight ramp having a constant ramp angle of $\epsilon = 8.2^\circ$ over the last 50% of the lobe length. Following the calculation procedure described in the section titled Approximate Analysis, it is shown in Appendix E that transverse velocity magnitude should be constant within the lobe interior and be given by:

$$v = U_\infty \tan \epsilon \quad (8)$$

Using the above angle and the local axial exit velocity, the ideal transverse component magnitude at the mixer exit would be $(U_\infty \tan \epsilon)(u+U_\infty/U_\infty)$ or 21.5% of U_∞ . As can be seen from Figure 39, the central portion of the trough is characterized by velocities in the 20 to 23% range with 21% being an approximate mean. The transverse component flow in this lobe segment, therefore, effectively achieved ideal values. This is consistent with the 95% effective penetration for this lobe calculated in the last section from axial velocity data. Specifically, $v/U_\infty = (u+U_\infty)/U_\infty (\tan 0.95\epsilon)$ yields a percentage of 20.4% which is close to the experimental mean of 21%.

Consideration of the upward penetrating lobe (peak), shown on the left side of the transverse velocity plot is complicated by a geometrically varying ramp angle and hence a rigorous comparison, similar to the above, is not possible. The following semi-quantitative comparison, however, gives reasonable results. The overall height-to-length ratio for the lobe corresponds to an angle of 7° , however, this value monotonically decreases to a trailing edge value of 1° .

Since a distance is required for the overall flow field to readjust to a change in lobe slope, an intermediate effective ramp angle would be expected. The measured transverse component magnitude of $10\% U$ corresponds to an effective angle of about 3.5° , which is plausible since this is the mean angle over the last 30% of the lobe length (or about 1.2 times the peak-to-trough lobe height). The above suggests that contouring a lobe to yield a small slope at the lobe trailing edge is undesirable. Furthermore, maintaining a near zero slope for several channel heights would be expected to effectively eliminate the transverse component responsible for exit plane circulation and mixing.

Turbofan engine mixer geometries such as that studied by Paterson have a decreasing slope in the trailing edge of the primary stream lobe. This is done to prevent heating due to direct impingement on the tailpipe wall and high expected turning losses. It is clear from the current study in which two lobes of similar overall height-to-length ratio but differing ramp angle schedules (straight verses tapered) were investigated in the same flow environment, that ramp angle tapering has a strong negative influence on transverse component magnitude and hence shed circulation.

One additional observation is useful relative to the data and approximate analysis. The data shown in Figure 39 confirms the analytical result that transverse component magnitude for a parallel-sided lobe is invariant with respect to transverse position, y , within the lobe interior. This will be shown subsequently to be the cause of the higher exit circulation obtained with this lobe relative to the sinusoidal lobes.

In summary, data from the straight-ramped downward penetrating lobe conclusively showed that the advanced mixer produced nearly ideal transverse component magnitudes.

Spanwise Velocity Field - Spanwise velocity components for the advanced mixer were substantially different from the low and high penetration sinusoidal models as shown in the left hand portion of Figure 39. This difference can be attributed to the close proximity of the exit plane measurement station to the trailing edge of this mode ($\bar{x} = 0.05$). The trailing edge geometry was a semicircle with a diameter of 0.06, hence the measurement station was only one trailing edge thickness downstream of the blunt base. As shown in the study by Paterson and Weingold (References 16,17), the near wake of such a trailing edge consists of a closed recirculation bubble having a length of about one trailing edge thickness. In response to the termination of the bubble in the axial direction the flow is directed inward on both sides toward the trailing edge centerline thereby filling in the wake behind the edge. Quantitatively, Reference 16 shows that at one trailing edge thickness downstream of the trailing edge, and one thickness offset from centerline, the inwardly directed velocity component is 9% of the axial velocity. This relative location corresponds closely to the Figure 39 traverse at $z=0.57$ where values ranging from 7 to 11% of U_∞ are observed on right side of the vertical portion of the lobe. Values obtained along transverse lines at $z=0.17$, 0.37 and 0.77 are also consistent with Reference 16 results. From this it is concluded that the spanwise component field between $y=-0.8$ and 0.8 is dominated by this near wake effect. If taken further downstream at the $\bar{x}=0.36$ location used for the previous models, ie. at seven trailing edge thickness downstream, Reference 16 shows these spanwise components would have decayed to levels on the order of one percent.

Excluding this localized near wake effect, the observed lack of significant spanwise flow for this model is consistent with the advanced mixer geometry of parallel-sided lobes. The low and high penetration sinusoidal mixers had non-parallel sides which induced spanwise components because of the boundary condition of no flow through the surface.

The only exceptions to negligible far wake components therefore are in the regions above $y=1$ and below $y=-1$ where measureable vectors to the right and left, respectively, are observed. These motions can be attributed to the vertical growth of the lobes in the downstream direction thereby reducing the area between the lobe peaks and the tunnel wall. The resultant compression forces fluid to the side, much as occurs in turbofan engine mixers in the region between the primary stream lobe peak and the tailpipe wall. This compression effect supports the generation of an axial vortex since it causes a circulation contribution which is additive to the circulation produced by the transverse velocity component. Such compression did not occur in the sinusoidal mixer experiments where the models were effectively unbounded (free of tunnel wall effects).

Combined Transverse - Spanwise Velocity Field - The advanced mixer exit secondary flow pattern is presented in Figure 40. As previously discussed relative to the spanwise velocity component field, this plot contains highly localized near wake spanwise velocity perturbations associated with the blunt trailing edge of the model. These components would have been negligible at the $\bar{x}=0.36$ location employed for the other mixer models and should therefore be

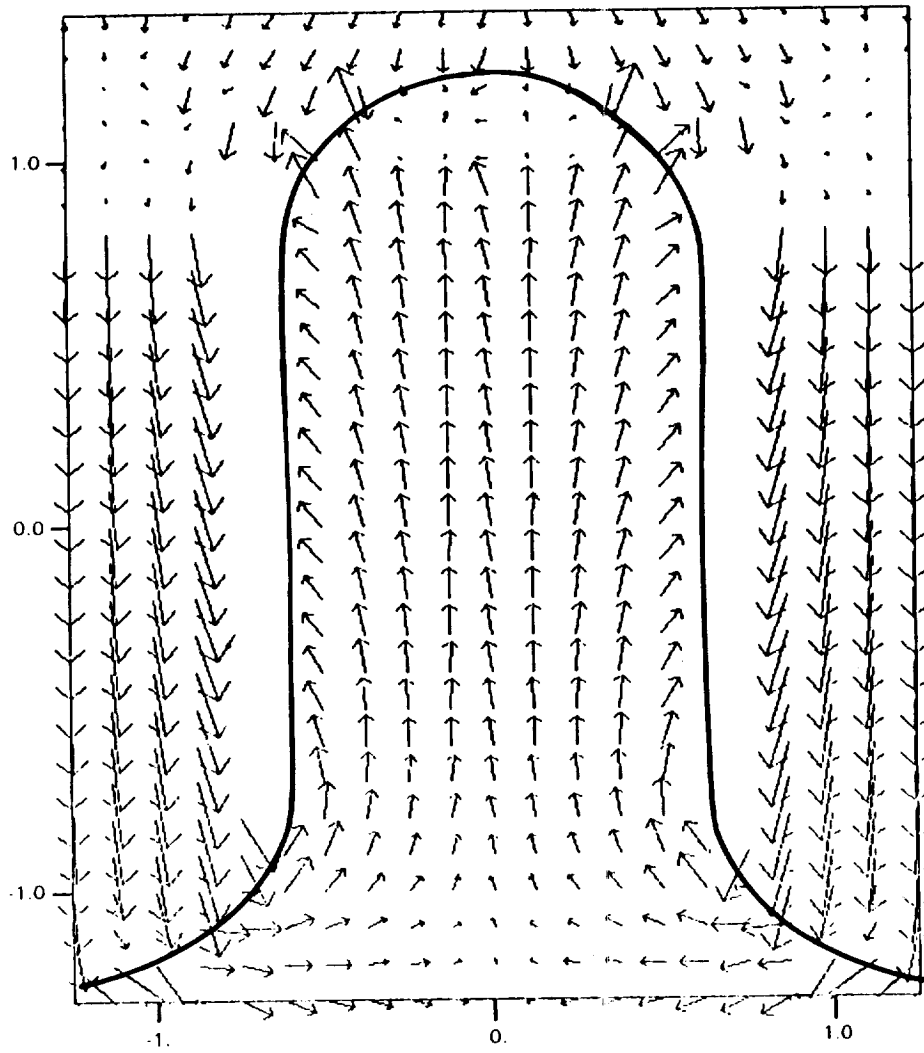


Figure 40 Advanced High Penetration Mixer Exit Plane Secondary Velocity Field

disregarded when making comparisons. Figure 40 shows the same general counter-rotating axial vortex pattern obtained with the sinusoidal models. The resultant vortex circulation is presented in the section, "Circulation Calculations".

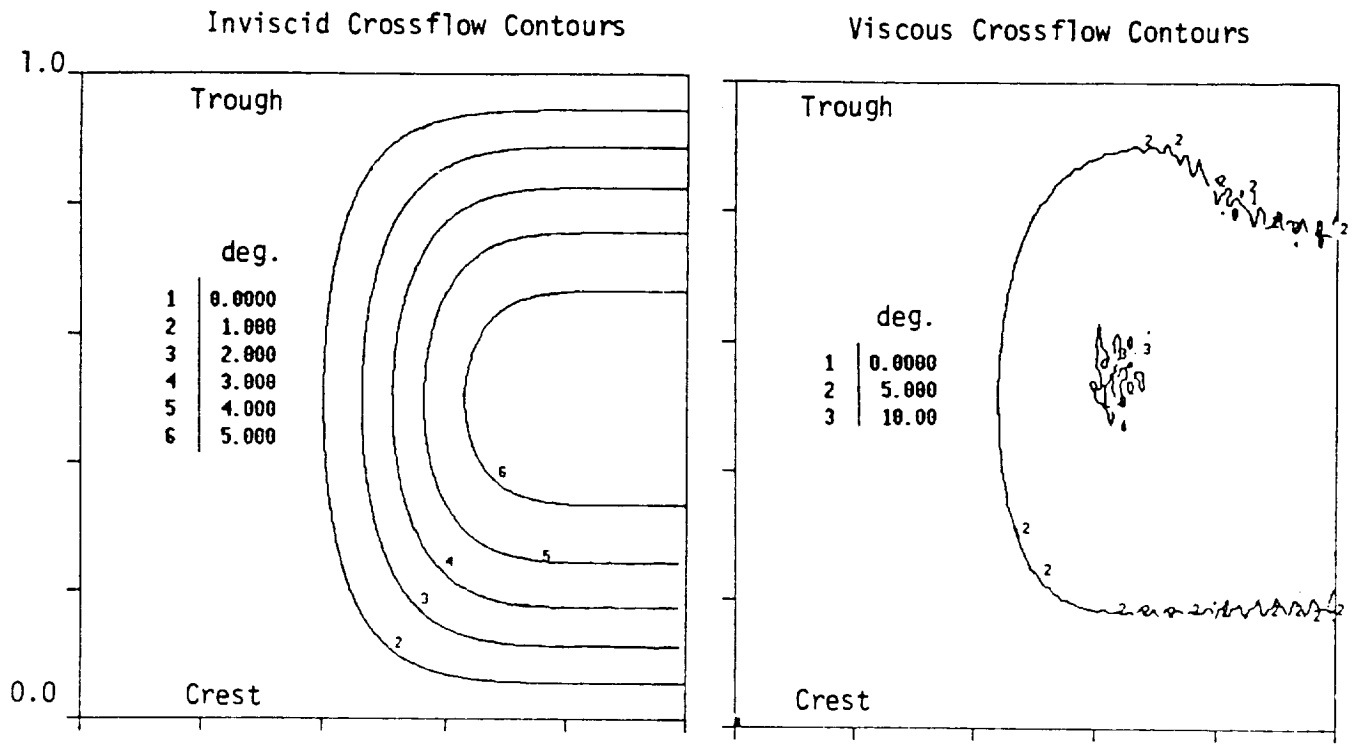
B. Mixer Flow Analysis

In Section III, two inviscid linearized potential flow analyses (PLANMIX and FLOMIX) were used to analyze the flow over the three lobed mixer contours for which experimental measurements were presented in Section IV. The results of these analyses, presented in Figures 6, 11, and 12 show that the lobes induce a spanwise or cross stream pressure gradient that force the flow off the crest and into the trough. The experimental results presented in Section IV furthermore showed that the sinusoidally shaped lobes did not achieve their ideal levels of penetration, based on their lobe height to length ratio, primarily due to a buildup of boundary layer flow in the trough. It was, moreover, observed that the boundary layer distribution at the trailing edge of the advanced high penetration lobe was more evenly distributed over its surface area. An analytical solution of the lobe boundary layer development was therefore made to see if these characteristics could be attributed to the inviscid pressure gradient alone.

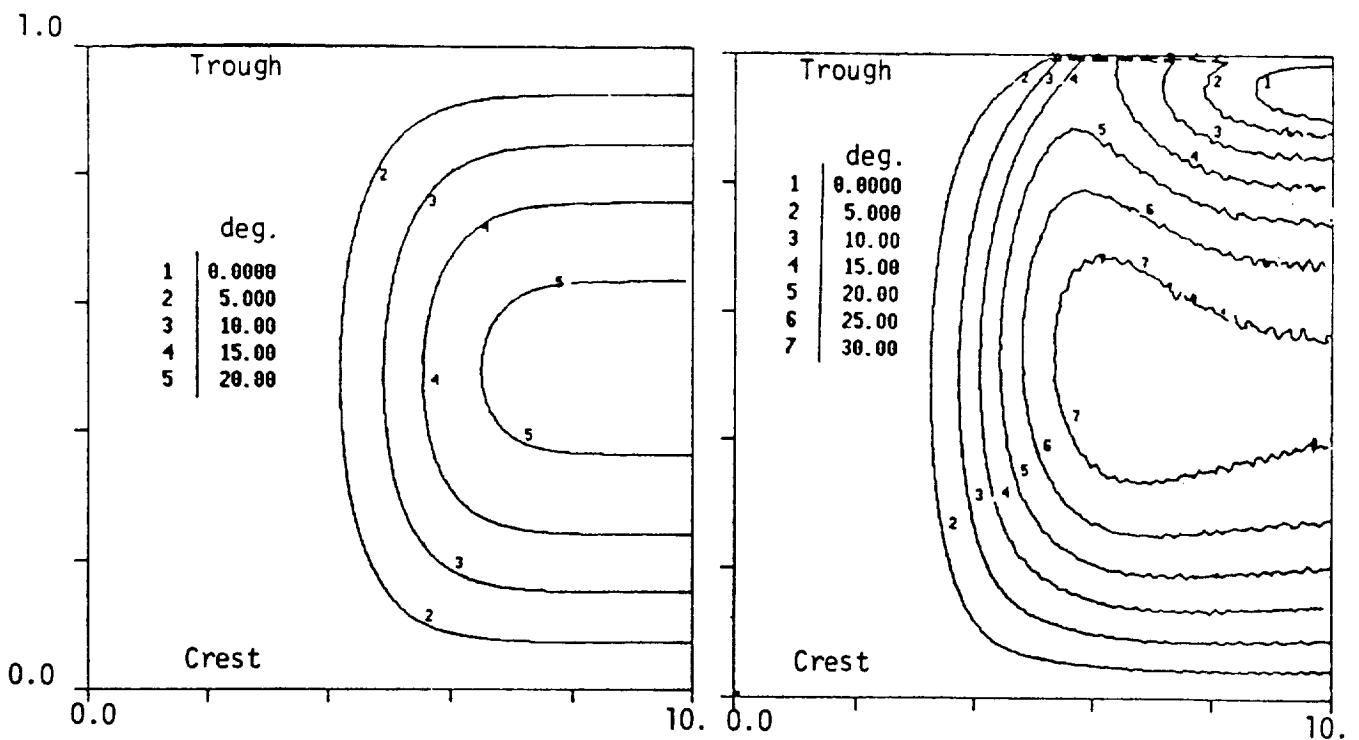
A calculation of the boundary layer development on the surface of the analyzed mixer lobes was made using a three-dimensional turbulent differential method of Vatsa (Ref. 18, 19). This method is based on the two-dimensional concepts of Blottner (Ref. 20) but was extended by developing a more suitable transformation based on the Levy-Lees variables. The method has been used to obtain solutions to a number of complex turbomachinery problems. This procedure has been also modified to treat arbitrary three-dimensional surfaces using a nonorthogonal surface oriented coordinate system (Ref. 21). The inviscid surface flow field obtained from the PLANIX or FLOMIX codes was adapted to this nonorthogonal frame of reference to provide edge conditions for the boundary layer analysis.

The solution procedure is a forward marching algorithm, propagating disturbances according to characteristic zone of influence conditions. The solution was initialized to march from the inlet to lobe exit plane and march off the lobe crest symmetry line to the lobe trough. The calculation was tripped to turbulent close to the inlet or leading edge and an equilibrium turbulent profile was generated substantially upstream of the lobe break location. The boundary layer calculations were made on a 100 by 100 surface grid with 100 points normal to the surface.

The boundary layer results for the low and high penetration sinusoidal lobed mixers are shown in Figures 41-43. Figure 41 shows a contour plot comparison of the cross flow angle at the edge of the boundary layer (inviscid - from the linear analyses) and the cross flow angle along the surface (viscid - from 3D

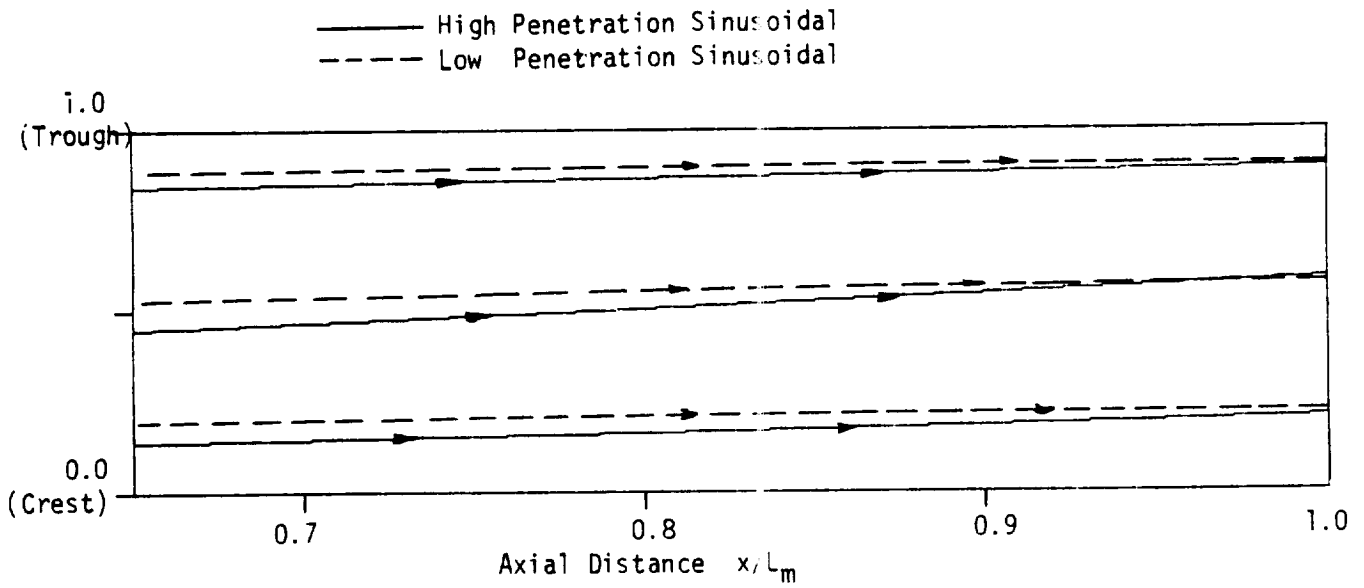


(a) Low Penetration Sinusoidal Mixer Lobe

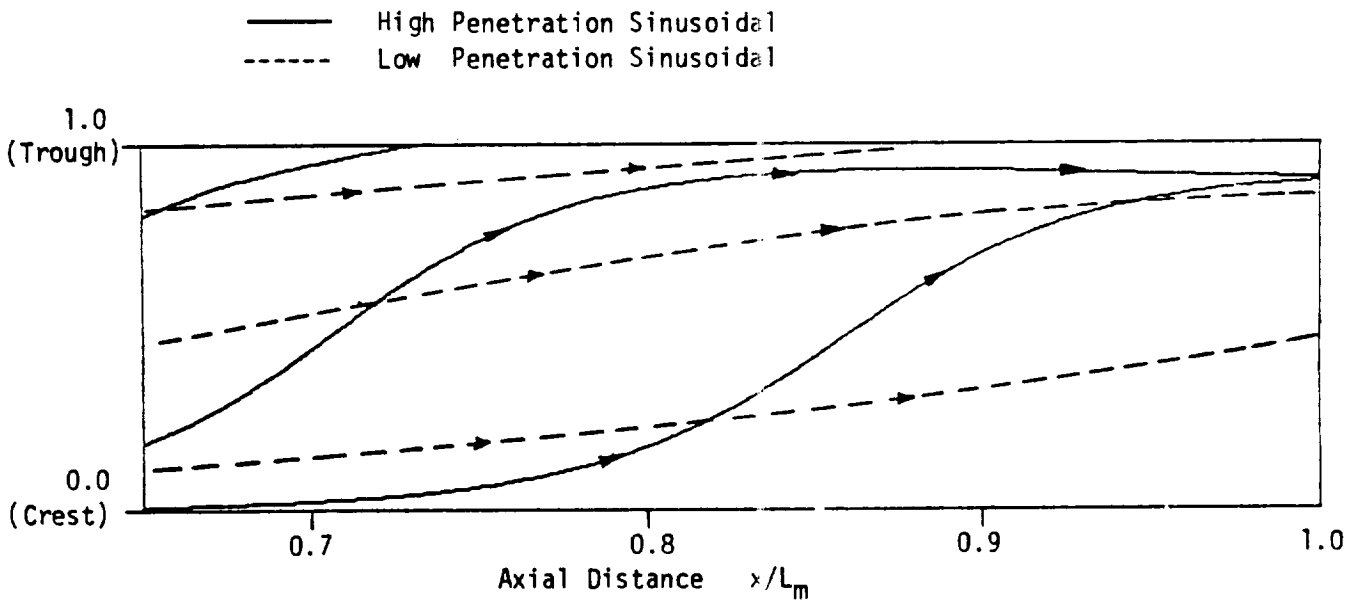


(b) High Penetration Sinusoidal Mixer Lobe

Figure 41 Calculated Surface Inviscid and Viscous Crossflow Angle Contours for Sinusoidal Lobed Mixers



(a) Inviscid Streamlines



(b) Viscous Streamlines

Figure 42 Calculated Streamline Deflections due to Inviscid and Viscous Effects for Sinusoidal Lobed Mixers

boundary layer analysis). The plots have been plotted on an enlarged spanwise scale. One can clearly see that viscous effects have significantly increased the flow skewing on the high penetration mixer, but that the maximum skewing effect still occurs at the trailing edge, midway between the crest and trough. The increase in skewing on the high penetration surface is about 50% over the inviscid level. This trend is seen more clearly in the calculated streamline patterns shown on Figure 42 (a) and (b). The lobe aspect ratio has been maintained here, so only the last third of the lobe surface has been displayed. The effect of the viscous boundary layer on slow skewing is clearly noticeable. The streamline deflection increase on the low penetration surface shown in Figure 42 (a) is very slight, while the increased skewing angle for the high penetration mixer, shown in Figure 42 (b) is so severe that one can visualize the flow being swept off the crest and into the trough.

Finally, Figure 43 shows the trailing edge distribution of δ_{99} , the boundary layer thickness, relative to that on an equivalent length flat plate. The results show the same trends demonstrated experimentally in Section IV, i.e. that the boundary layer is driven from the crest and that the trough boundary layer is significantly increased. Furthermore, the boundary layer buildup effect on the high penetration lobe is larger than that for the low penetration lobe.

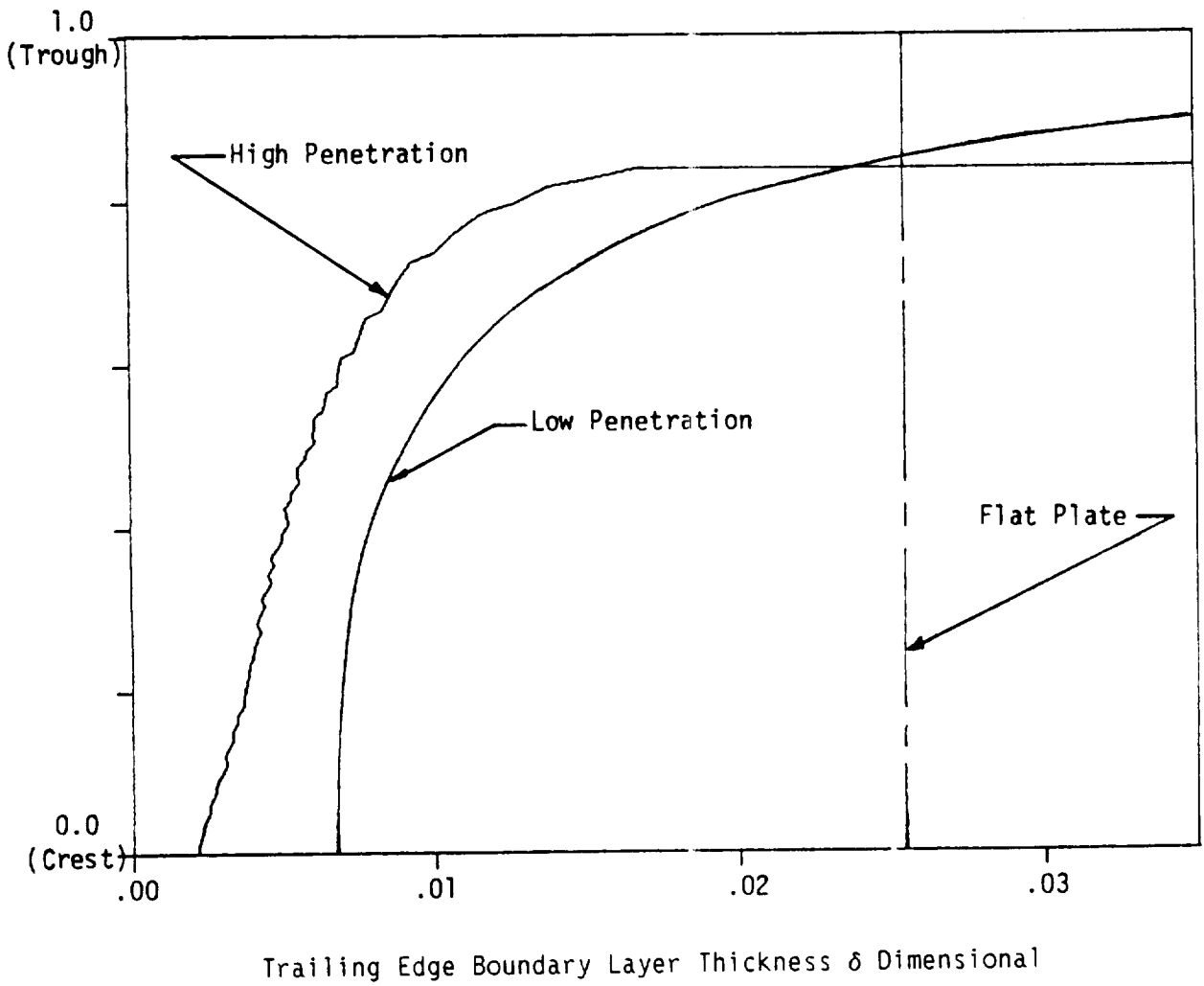


Figure 43 Calculated Lobe Trailing Edge Boundary Layer Thickness Distributions for Sinusoidal Lobed Mixers

C. Mixer Flow Field Model

1. Circulation Calculations

The most important single parameter describing the velocity field shed from the mixer lobe trailing edge is the vortex circulation, Γ produced in each lobe segment and found by performing a contour integration in a plane normal to the axial direction. This circulation is related to downstream mixing rate as discussed in the next section. In this section, vortex circulation is calculated for the three mixer configurations by integrating experimentally determined secondary velocity fields about an appropriate contour. Comparisons are made with estimates derived from the approximate inviscid analysis. Comparisons with FLOMIX results are given in the section titled Flow Analysis.

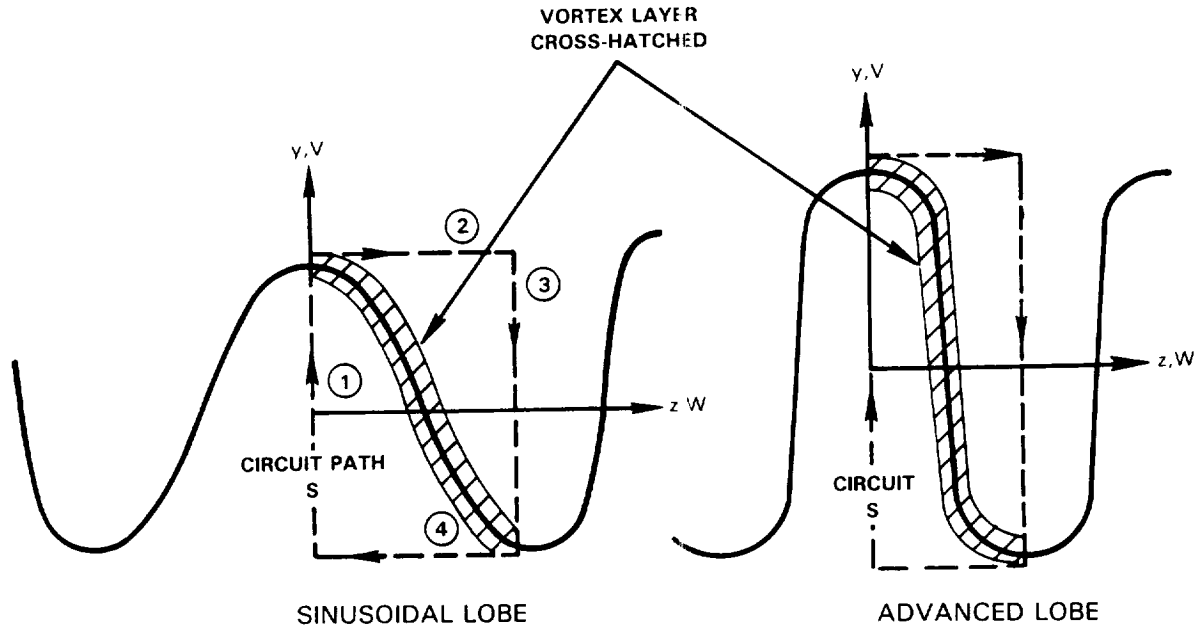
Referring to the integration path sketched below, exit plane circulation is given by:

$$\Gamma = \oint_C \vec{v} \cdot d\vec{s} = \int_1 v dy + \int_2 w dz + \int_3 v dy + \int_4 w dz \quad (9a)$$

$$= \Gamma_v + \Gamma_w \quad (9b)$$

where the numbers refer to the integration paths shown in the sketch.

The quantities Γ_v and Γ_w are the circulation contributions from the two vertical and horizontal legs of the circuit, respectively. The circulation, Γ , represents the strength of the vortex layer (or sheet) which is located along the trailing edge surface and is shed into the wake. This circulation should



be independent of the path chosen for integration if the path encompasses the entire sheet. The above path satisfies this requirement and has been chosen for ease of integration.

Results of the circulation calculation are given in the table below. Row 1 of the table gives absolute values of the circulation, based on experimental data, for all three models in terms of U_∞ (the upstream freestream velocity) and L , the lobe width on mixer centerline. The quantity L appears here, not because it is a circulation parameter, but because it has been used to non-dimensionalize all distances in this report. The value of L for all three models was 2.54 cm. As can be seen, the high penetration sinusoidal mixer had the highest circulation, being 12.2 times larger than the low penetration model. The advanced high penetration mixer was intermediate between these two, being 4.4 times larger than the circulation for the low penetration model. The above has considered absolute levels of circulation per lobe segment for models having significantly different geometries. The next paragraph considers the dependence of circulation on the important geometrical parameters.

TABLE CIRCULATION RESULTS

Quantity	Model		
	Low Penetration	High Penetration	Advanced High Penetration
Γ (exper.)	0.16 $U_\infty L$	1.96 $U_\infty L$	0.7 $U_\infty L$
$C = \frac{\Gamma}{U_{REF} h \tan \epsilon}$ (exper.)	3.3	2.4	3.9
C_1 (from approximate analysis)	2.5	2.5	4.0

Row two of the table addresses circulation scaling in terms of these key parameters. According to the approximate inviscid analysis given in Appendix D.4, the circulation for all models is given approximately by

$$\Gamma = C_1 U_{REF} h \tan \epsilon \quad (10)$$

where C_1 is a numerical constant dependent on lobe geometry. U_{REF} is axial velocity at the lobe trailing edge, which for the sinusoidal models was U_∞ and for the advanced model was $1.49 U_\infty$ due to tunnel wall contraction. The quantities h and ϵ are the lobe amplitude (one-half the peak-to-peak amplitude) and lobe ramp angle, respectively.

As can be seen from the results in the second row, normalization of experimentally derived Γ in the manner suggested by Equation (10) reduces the ratio of high-to-low penetration sinusoidal mixer circulation from 12.2 to 1.4. To first order, therefore, the inviscid scaling is verified for these two geometrically similar mixers.

Some complications ensue in obtaining C_1 for the advanced mixer because the ramp angle was different for adjacent lobes. As discussed in the section titled "Transverse Velocity Field", ramp angles for the two lobes were derived to be 8.2 deg. and 3.5 deg. Use of the average of these angles (5.85 deg) leads to the constant of 3.9 shown. The higher value of the constant relative to the sinusoidal mixers is due to the more effective parallel-wall geometry of the advanced mixer. This circulation enhancement is confirmed in row three where the theoretical constants C_1 , derived in Appendix D.4, are given for sinusoidal and parallel wall geometries. As can be seen, the parallel walled lobe circulation is predicted to be higher than the sinusoidal lobe circulation and is in close agreement with experiment.

Since the approximate analysis is a one-dimensional calculation it can be expected to be most accurate in the limit of large sinusoidal amplitude (high aspect ratio lobes have a flow which is closer to one-dimensional) and this is observed to be the case based on the close agreement of experimental and theoretical C_1 constants for the high penetration sinusoid. As shown in Appendix D.4, the sinusoidal mixer calculation neglects contributions from the horizontal legs of the circuit shown above. Based on data, this contribution to total circulation was negligible for the large aspect ratio sinusoidal mixer (only 2%) but appreciable for the low penetration sinusoid (24%). The more two dimensional flow character of the low penetration sinusoid, therefore, is the reason for the discrepancy between measurement and analysis shown in column 1. The parallel-sided lobe calculation is the most accurate

since there is no horizontal leg contribution and the flow is inherently one-dimensional by virtue of the parallel walls. In summary, for parallel-sided lobes or sinusoidal lobes having the high aspect ratio necessary to produce large circulations, the approximate calculation gives a good estimate of the circulation shed at the mixer trailing edge.

One conclusion resulting from the above is that the approximate circulation scaling given by Equation (10) is supported by the data. A second conclusion is that the advanced mixer, having parallel sidewalls, is inherently superior in terms of circulation, to sinusoidal lobes (that is, for similar ramp angle and lobe amplitude, the ratio of parallel walled to sinusoidal lobe circulations would be 4.0/2.5 or 60% greater). In fact the approximate analysis in Appendix D.4 shows that the more pointed the lobe, the lower the value of C_i , ie. parallel-walled lobes, sinusoidal lobes and triangular lobes have constants of 4, 2.5 and 2, respectively. The relatively high C_i value of 3.3 obtained experimentally for the low penetration sinusoidal is not practically important, because to achieve the C_i benefit for a fixed lobe length L_m , lobe amplitude, h , must be reduced dramatically and the scaling shows circulation is proportional to the square of this amplitude, ie.

$$\Gamma \sim h \tan \epsilon \sim h^2/L_m \quad (11)$$

where L_m is lobe axial Length. A low penetration sinusoidal mixer, such as considered here, therefore, will produce a high C_i constant but poor circulation per lobe segment.

2. Circulation and Mixing

This section discusses the effect of lobe exit circulation and other lobe parameters on downstream mixing. From the standpoint of mixing it is believed that maximizing circulation per lobe segment is advantageous. This is the basic conclusion of Paterson's previous forced mixer nozzle study. As shown by Equation (10), this can be achieved, in part, by using the largest ramp angle, ϵ , that does not cause separation within the lobe. This is a strong effect since circulation is proportional to the square of lobe amplitude. Tapering ramp angles at the trailing edge of a lobe is clearly undesirable. Circulation can also be increased by accelerating flow within the lobes to produce a higher exit plane U_{REF} . Such acceleration is also desirable to thin lobe boundary layers and reduce lobe peak blockage. Circulation can also be enhanced by selecting geometries having high C_l constants. For planar configurations, purely rectangular lobes have the highest theoretical value but rectangular lobes with rounded peaks and troughs may be superior because corner secondary vortices and flow separation off the ramp in the outer flow can be avoided. Such vortices were found by Paterson (Reference 4) in a survey downstream of rectangular lobes.

Lobe segment circulation is not the only parameter affecting downstream mixing. Lobe width is another free and important parameter. It is clear that extremely narrow lobes will behave poorly because sidewall boundary layers will merge on lobe centerline producing viscous losses and reduced circulation due to increased peak region blockage. Very wide lobes, however, are undesirable since the average vorticity per lobe segment is reduced. This can be seen, for example, in the following expression for a rectangular lobe. For such a lobe, average vorticity per lobe, $\bar{\omega}$, is given by:

$$\omega = \frac{\Gamma}{2hL} = + \frac{2U_{REF} \tan \epsilon}{L} \quad (12)$$

Stated in a different manner, vortex sheets (concentrated along the lobe sidewall trailing edges) will roll-up to produce a vortex having some characteristic lateral scale. If this scale is small relative to lobe width, then regions of irrotational flow will exist between adjacent counter rotating vortices. These irrotational flow regions will mix out slower than those regions containing vortices and mixing will be degraded. Improved understanding of the effect of L on mixing can only come from mixing calculations. This is also true of the remaining mixing parameter which is the lobe penetration (ratio of lobe height to mixing duct height).

In summary, this study produced insight into the lobe circulation development process. It now remains to extend the preliminary calculation shown in Appendix A, where the FLOMIX lobe calculation was coupled with a downstream mixing calculation and to perform a comprehensive parameter variation study on the effects of lobe penetration and lobe width for various lobe geometries and selected values of ramp angle and U_{REF} . This should be complemented by experiments in which mixing is measured (eg. using a cold and warm stream configuration to permit temperature to be used to define mixing) at several downstream locations for selected designs. For planar configurations, the prime emphasis should be on the parallel-sided geometry shown here to maximize circulation. For other geometries, such as axisymmetric, the approximate inviscid analysis can be used to identify preferred geometries.

It is also clear that further experimental and analytical research is needed in the area of vortex dynamics. For similar values of lobe segment circulation, different lobe width-to-lobe height ratios would be expected to affect vortex roll-up. Thus while designing lobes to maximize circulation is important, this is not sufficient to maximize downstream mixing ratio.

VI. SUMMARY OF RESULTS

1. Experiments conducted with three planar mixer lobe models confirmed the findings of a previous research program that lobed mixers produce a periodic array of adjacent, contrarotating streamwise vortices downstream of the lobe exit plane. The transverse scale of the vortices is comparable to the lobe-to-peak amplitude and the spanwise scale of each vortex is one-half of the periodic lobe wave length.
2. Planar and axisymmetric linear inviscid analyses were developed to predict the secondary velocity fields and vortex circulations at the exit plane of periodic lobed mixers. A coupled three-dimensional boundary layer analysis was applied to predict exit plane boundary layer characteristics. These analyses were then used to predict flow development for the three mixer configurations studied experimentally. Additionally, an approximate inviscid analysis was developed to identify scaling parameters for lobe circulation and to assess waveform geometry effects on exit plane circulation.

3. Transverse velocity component measurements at the exit plane of the three models tested showed significant cross-stream flows in the direction of the lobe peak on the order of 10 - 30% of the lobe exit axial velocity. Magnitudes were largest for high penetration sinusoidal model which also has the largest lobe amplitude. Transverse velocity magnitudes diminished in the interior lobe peak region of the sinusoidal models whereas the advanced mixer displayed near ideal velocity levels well into the lobe peak.
4. Axial velocity and total pressure measurements at the exit plane of the two sinusoidal waveform mixers indicated significant viscous retardation effects occurred within the peak interior region of the lobes. Similar measurements for the advanced mixer showed much thinner lobe boundary layers with inviscid flow extending well into the rounded lobe peak region.
5. Spanwise velocity component magnitudes at the lobe exit plane were substantially smaller than the transverse component for all three models.
6. Surface flow visualization of the lobes showed skewing of the near surface flow toward the lobe peak and trough regions. As expected, the degree of skewing was greatest for the two high penetration models.

VII. CONCLUSIONS

1. The array of large scale, streamwise vortices shed from the trailing edge of convoluted lobe mixers is a consequence of the combined transverse and spanwise pressure field created by lobe penetration into the approaching stream. Cross-stream pressure gradients in conjunction with a lobe trailing edge Kutta condition create a pressure driven secondary flow field having significant transverse velocity components. Cross-stream pressure gradients also cause skewing of the lobe boundary layer toward the lobe peak and trough regions, the origin of the streamwise vortex array is basically inviscid in nature.
2. Linear inviscid analyses developed in this study, in conjunction with a three-dimensional boundary layer analysis, are capable of predicting lobe streamwise vortex array characteristics. Predicted lobe exit plane streamwise vortex circulations and boundary layer characteristics were found to be in favorable agreement with current experimental results. Since the lobe flow was found to be inviscid, a boundary layer analysis is only needed if details inside the viscous region are needed.
3. An approximate inviscid analysis identified the primary parameters affecting exit plane circulation for straight ramped lobes as the ratio of lobe amplitude squared-to-lobe length, exit plane axial velocity and a lobe shape factor which varies with lobe spanwise waveform. Circulation is found to be equal to the product of these factors, therefore exhibiting a strong dependence on lobe amplitude. Experimental data obtained in the study confirmed the lobe amplitude and axial velocity scaling.

4. The lobe shape factor is highest for parallel-sided lobe configurations (similar to the advance high penetration mixer tested in the study). Such configurations are inherently superior to non-parallel walled configurations such as sinusoidal or triangular. Experimental data obtained in the study confirmed the predictions relative to parallel-sided and sinusoidal configurations.
5. The advanced mixer model tested in the program nearly achieved the ideal exit plane circulation predicted by an inviscid analysis. In addition to an inherently lower circulation geometry, the two sinusoidal mixer models were adversely affected by boundary layer buildup in the interior peak region of the lobes. This reduced the effective lobe amplitude and consequently the circulation shed into the wake.
6. The final conclusion of this study is that future work should be directed toward integration of the linear inviscid analysis into an overall mixer mixing analysis permitting mixing calculations to be performed for a series of lobe geometrical parameters. A complementary experimental study of downstream mixing should also be performed thereby providing a verified overall design analysis system for use in turbofan engine, ejector and other convoluted lobe mixing applications.

REFERENCES

1. Presz, W. M., Jr., Gousy, R., and Morin B., " Forced Mixer Lobes in Ejector Designs," AIAA 86-1614, AIAA/ASME/SAE/ASEE 22nd Joint Propulsion Conference, Huntsville, AL, 1986.
2. Werle, M. J., Paterson, R. W., and Presz W. M., Jr., "Flow Structure in a Periodic Axial Vortex Array," AIAA 87-0610, AIAA 25th Aerospace Sciences Meeting, Reno, NV, 1987.
3. Werle, M. J., Paterson, R. W., and Presz, W. M., Jr., " Trailing-Edge Separation/Stall Alleviation," AIAA Journal, Vol. 25, No. 4, 1987, p. 624.
4. Paterson, R.W., "Turbofan Forced Mixer-Nozzle Internal Flowfield, Part I - A Benchmark Experimental Study," NASA CR 3492, April, 1982. Also ASME Journal of Engineering for Gas Turbines and Power, Vol. 106, July 1984, pp. 692-698.
5. Povinelli, L., Anderson, B., and Gerstenmaier, W., "Computation of the Three-Dimensional Flow in Turbofan Mixers and Comparison With Experimental Data," AIAA Paper 80-0227, Jan. 1980.
6. Anderson, B., Povinelli, L., and Gerstenmaier, W., "Influence of Pressure Driven Secondary Flows on the Behavior of Turbofan Forced Mixers," AIAA Paper 80-1198, AIAA/ASME/SAE 16th Joint Propulsion Conference, July, 1980.
7. Povinelli, L.A., and Anderson, B.H., "Investigation of Mixing in a Turbofan Exhaust Duct, Part II: Computer Code Application and Verification," AIAA J., Vol. 22, No. 4, 1984, p. 518
8. Amiet, R.K., "User's Manual a Laterally Planar Inviscid Mixer Analysis," Pratt & Whitney Report PWA-5904-18, 1983.
9. Barber, T.J., "Turbofan Forced Mixer Lobe Flow Modeling, Part II: - Three-Dimensional Inviscid Mixer Analysis (FLOMIX)," to be published as a NASA CR XXXX, 1986.
10. Barber, T.J., Muller, G.L., Ramsay, S.M., and Murman, E.M., "Three-Dimensional Inviscid Flow in Mixers, Part I: Mixer Analysis Using a Cartesian Grid," AIAA J of Propulsion & Power, Vol. 2, No. 3, 1986, P. 275.
11. Barber,AT.J., Muller, G.L. Ramsay, S.M., and Murman, E.M., "Three-Dimensional Inviscid Flow in Mixers, Part II: Analysis of Turbofan Forced Mixers," AIAA J Propulsion & Power, Vol. 2, No. 4, 1986, p. 339.
12. Larkin, M.J., and Blatt, J.R., "Energy Efficient Engine Exhaust Mixer Model Technology Report Addendum-Phase III Test Report," NASA CR 17499, 1984.
13. Maskew, B. "Prediction of Subsonic Aerodynamic Characteristics: A Case for Low-Order Panel Methods," AIAA J Aircraft, Vol. 19, No. 2, 1982, p.157

14. Clark, D.R., Maskew, B., & Dvorak, F.A., "The Application of a Second Generation Low-Order Panel Method--Program VSAERO-- to Powerplant Installation Studies," AIAA Paper 84-0122, AIAA 22nd Aerospace Sciences Meeting, Reno, NV, 1984.
15. Coles, D. E., "The Turbulent Boundary Layer in a Compressible Fluid," Report R-4-3-PR, Rand Corporation, Santa Monica, CA, September 1962.
16. Paterson, R. W., and Weingold, H. D., " Supercritical Airfoil Technology Program," Pratt & Whitney Aircraft, FR-15859, October 1982.
17. Paterson, R. W., and Weingold, H. D., " Experimental Investigation of a Simulated Compressor Airfoil Trailing Edge Flowfield," AIAA Journal, Vol. 21, No. 5, 1985, p. 768.
18. Vatsa, V. N., "A Three-Dimensional Boundary Layer Analysis Including Heat Transfer and Blade Rotation Effects," Third Symposium on Numerical and Physical Aspects of Aerodynamic Flows, Long Beach, CA, 1985.
19. Vatsa, V. N., "A Three Dimensional Boundary Layer Analysis for Turbomachinery Applications," UTRC Report 84-44, 1984.
20. Blottner, F. G., "Computational Techniques for Boundary Layers AGARD Lecture Series 73, presented at VKI, February 1985.
21. Anderson, O. L., "Assessment of a 3-D Boundary Layer Analysis to Predict Heat Transfer and Flow Field in a Turbine Passage," UTRC Report R85-956834, also NASA CR-174894, 1985.
- A.1 Briley, W.R., and McDonald, H., "Analysis and Computation of Viscous Subsonic Primary and Secondary Flows", AIAA 4th Computational Fluid Dynamics Conference, Williamsburg, VA, 1979.
- A.2 Kreskovsky, J.P., Briley, W.R., and McDonald, H., "Development of a Method for Computing Three-Dimensional Subsonic Turbulent Flows in Turbofan Lobe Mixers", Scientific Research Associates, Inc., R79-300006-F, 1979.

APPENDICES

A. Viscous Marching Analysis

B. Lobed Mixer Coordinates

1. Low Penetration Sinusoidal Lobed Mixer
2. High Penetration Sinusoidal Lobed Mixer
3. Advanced High Penetration Lobed Mixer

C. Code Input Files

1. PLANMIX: Low Penetration, High Penetration
2. FLOWMIX: Low Penetration, High Penetration, Advanced High Penetration

D. Experimental Data Base

1. Low Penetration: U+u,v,w and Pt data
2. High Penetration: U+u, v, w and Pt data
3. Advanced High: U+u,v, w and Pt and Boundary Layer Data
4. Boundary Layers

APPENDIX A
VISCOUS MARCHING ANALYSIS

An analytical study was performed to demonstrate the influence of pressure driven secondary flows on the behavior and performance of turbofan forced mixer nozzles. The viscous marching analysis used in this study was the PEPSIM approach developed by Briley, McDonald and Kerskovsky (Ref. A1, A2). The procedure is based on the decomposition of the velocity field into primary and secondary flow velocities. The governing equations are solved by a forward marching method, where elliptic effects due to curvature and area change are accounted for a priori through the imposed pressure gradients determined from a potential flow solution for the geometry in question. The inflow conditions entering the mixing duct were varied to demonstrate their effect on the mixing rate at the nozzle exit plane. In previous analytical studies, the secondary flow effect was represented as a superimposed radial velocity based on a factor of the local mainstream velocity.

In the present study, the benchmark experimental study of the JT8D-209 forced mixer was considered. Mixing predictions have been made using the PEPSIM analysis for the following inflow profiles:

1. the measured mixer lobe exit plane data,
2. an ideal inflow profile with no cross flow velocity field, and
3. an ideal inflow profile with a superimposed secondary flow field.

The ideal profile consists of a uniform primary and bypass profile separated by an assumed or estimated shear layer interface. In the latter case, a series of calculations were made where the degree of secondary flow was parametrically varied. The primary measure of measuring the mixing effectiveness of a specific input profile was the predicted total temperature profile. Exit plane profile comparisons with the measured traverse data were made at three equally spaced azimuthal cuts. A partial display of the results of this study is presented in Figure A.1. The top comparison indicates that by starting the calculation with the actual mixer lobe exit plane profile, one can obtain a reasonable level of agreement with the measured profiles. In contrast, the ideal profile input case shows very little agreement. At the bottom of the figure, one particular estimated secondary flow case is presented. The magnitude of the superimposed primary and secondary radial flows were estimated from the exit slope of the lobe crest and trough, respectively. The predicted profiles show some disagreement in level, however, they do follow the radial trends of the measured data. The analytical predictions therefore demonstrate that the driving mechanism of the forced mixer is the inflow secondary flow and that this effect can be modeled in an empirical fashion.

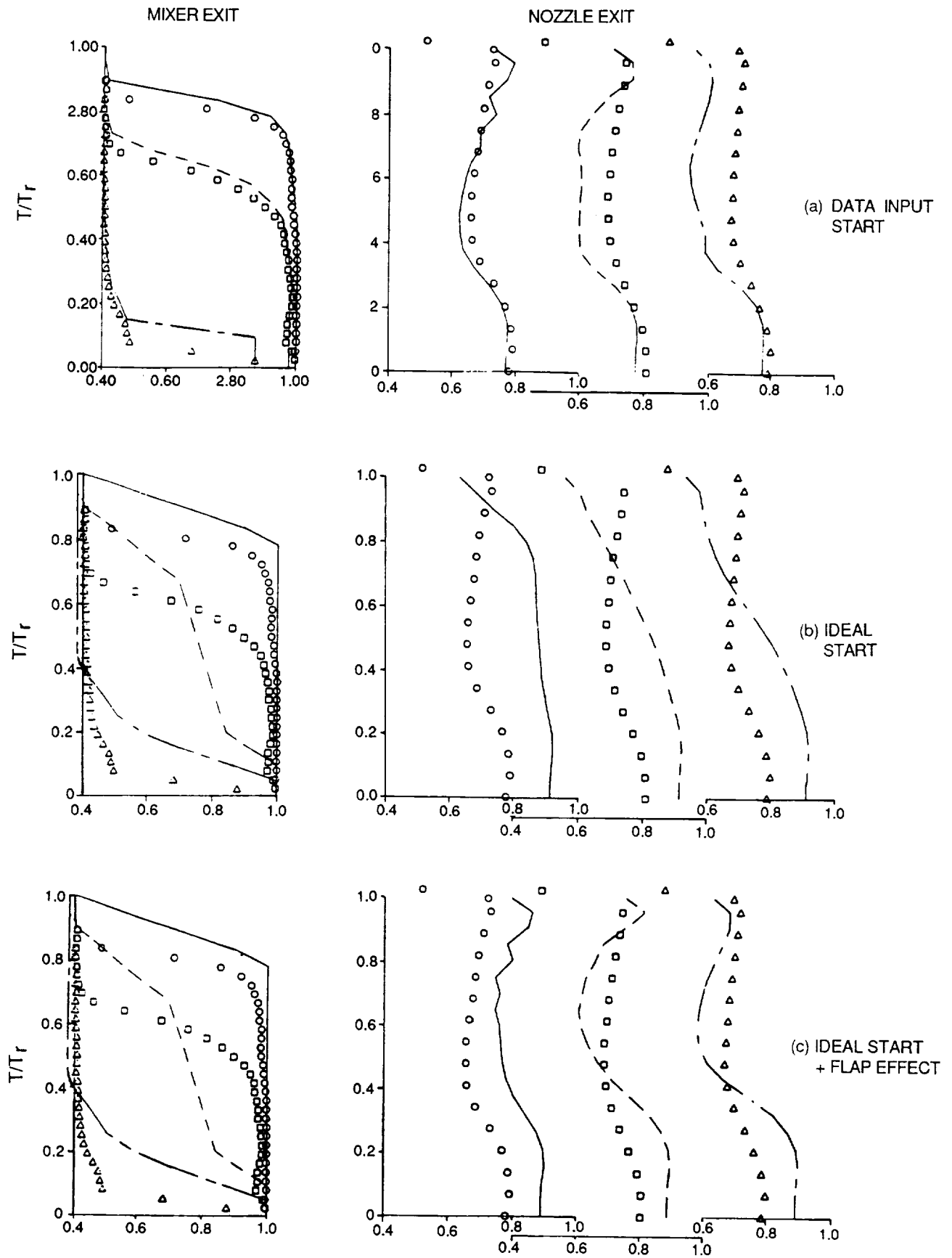


Figure A.1 Effect of Starting Conditions on PEPSI-M Calculated Temperature Ratio Profiles at Inlet and Exit Planes of JT8D-209 Mixing Duct.

(—○—, $\theta' = 0$; ---□---, $\theta' = 0.5$; -·-·-, $\theta' = 1$.)

TABLE B.1
LOW PENETRATION LOBED MIXER COORDINATES

I	AXIAL COORDINATE X(I)	RADIAL COORDINATE YCREST(I)
1	0.00000	0.10014E-04
2	0.51547	0.10014E-04
3	0.92784	0.10014E-04
4	1.44330	0.19997E-04
5	1.95877	0.79989E-04
6	2.47423	0.31999E-03
7	2.98969	0.12100E-02
8	3.50516	0.37900E-02
9	4.02062	0.99900E-02
10	4.43299	0.19290E-01
11	4.94845	0.38440E-01
12	5.46392	0.67200E-01
13	5.97938	0.10506E+00
14	6.49485	0.14986E+00
15	7.01031	0.19891E+00
16	7.52577	0.25000E+00
17	7.93814	0.29148E+00
18	8.55670	0.35398E+00
19	8.96907	0.39570E+00
20	9.48454	0.44785E+00
21	10.00000	0.50000E+00

EQUATION OF LOBE CROSS-SECTION

$$Y(I) = YCREST(I) * \cos \left| \frac{2\pi}{c} Z(I) \right|$$

$$\alpha = \theta = \pi$$

TABLE B.2
HIGH PENETRATION LOBED MIXER COORDINATES

I	AXIAL COORDINATE X(I)	RADIAL COORDINATE YCREST(I)
1	0.00000	0.00000E+00
2	0.51547	0.00000E+00
3	0.92784	0.10002E-03
4	1.44330	0.10002E-03
5	1.95877	0.30005E-03
6	2.47423	0.13000E-02
7	2.98969	0.48000E-02
8	3.50516	0.15200E-01
9	3.91753	0.33400E-01
10	4.53608	0.89600E-01
11	4.94845	0.15380E+00
12	5.46392	0.26880E+00
13	5.97938	0.42020E+00
14	6.49485	0.59940E+00
15	7.01031	0.79560E+00
16	7.52577	0.10000E+01
17	8.04124	0.12075E+01
18	8.55670	0.14159E+01
19	9.07217	0.16245E+01
20	9.58763	0.18331E+01
21	10.00000	0.20000E+01

EQUATION OF LOBE CROSS-SECTION

$$Y(I) = YCREST(I) * \cos \left| \frac{2\pi}{\alpha} Z(I) \right|$$

$$\alpha = Q = \pi$$

TABLE B.3.1
 ADVANCED HIGH PENETRATION
 LOBED MIXER COORDINATES

RADIAL COORDINATES			
I	AXIAL COORDINATE	YCREST(I)*	YTROUGH(I)*
1	46.000	-0.138	0.575
2	47.000	-0.138	0.575
3	48.000	-0.138	0.571
4	49.000	-0.138	0.550
5	50.000	-0.138	0.509
6	51.000	-0.138	0.449
7	52.000	-0.138	0.376
8	53.000	-0.138	0.308
9	54.000	-0.138	0.230
10	54.694	-0.138	0.179
11	55.000	-0.134	0.154
12	55.500	-0.116	0.112
13	55.600	-0.110	0.103
14	55.700	-0.104	-
15	55.800	-0.097	0.085
16	55.900	-0.089	-
17	56.000	-0.081	0.066
18	56.100	-0.071	-
19	56.200	-0.060	0.046
20	56.300	-0.049	-
21	56.400	-0.036	-0.033
22	56.500	0.036	-
23	56.600	0.049	-0.052
24	56.700	0.062	-
25	56.800	0.076	-0.070
26	56.900	0.090	-
27	57.000	0.105	-0.089
28	57.500	0.186	-0.137
29	58.000	0.268	-0.190
30	58.500	0.351	-0.244
31	59.000	0.434	-0.305
32	60.000	0.599	-0.429
33	61.000	0.766	-0.563
34	62.000	0.926	-0.703
35	63.000	1.055	-0.849
36	64.000	1.151	-0.992
37	64.500	1.180	-1.065
38	65.003	1.200	-1.137
39	65.600	1.210	-1.208
40	66.000	1.216	-1.281

* Y +/- 0.020

TABLE B.3.2
 ADVANCED HIGH PENETRATION
 MIXING DUCT COORDINATES

I	AXIAL COORD.	Y NOZZLE	I	AXIAL COORD.	Y CENTERBODY
1	40.000	2.360	1	41.000	-1.630
2	45.664	2.343	2	47.415	-1.630
3	46.493	2.340	3	51.093	-1.631
4	47.276	2.343	4	51.680	-1.632
5	47.735	2.344	5	54.204	-1.638
6	48.096	2.340	6	54.699	-1.637
7	48.497	2.327	7	54.997	-1.633
8	49.068	2.301	8	55.271	-1.623
9	50.406	2.235	9	55.749	-1.597
10	51.631	2.174	10	56.361	-1.560
11	52.497	2.134	11	56.844	-1.534
12	53.164	2.103	12	57.870	-1.484
13	54.000	2.057	13	58.483	-1.461
14	54.640	2.023	14	59.062	-1.446
15	55.320	1.991	15	59.750	-1.436
16	56.049	1.956	16	60.696	-1.427
17	56.685	1.928	17	61.636	-1.426
18	57.477	1.891	18	63.555	-1.427
19	60.402	1.758	19	64.133	-1.429
20	62.402	1.667	20	64.746	-1.437
21	63.201	1.631	21	65.289	-1.450
22	63.741	1.612	22	65.797	-1.468
23	64.320	1.598	23	66.178	-1.488
24	64.921	1.591	24	66.577	-1.516
25	65.724	1.587	25	67.065	-1.556
26	66.371	1.586	26	67.732	-1.618
27	70.354	1.585	27	68.647	-1.708
28	77.187	1.586	28	69.329	-1.771
			29	70.027	-1.828
			30	70.812	-1.886
			31	71.576	-1.935
			32	72.336	-1.976
			33	73.096	-2.011
			34	73.855	-2.037
			35	74.623	-2.058
			36	75.371	-2.070
			37	76.133	-2.075
			38	77.187	-2.076

TABLE C.1

Low Penetration Mixer

```

MIXER TEST CASE
196          0.0      .215  3.14159  .0220977
  81   41     0
    1.0     1.0     0.5     0.0
$VMESH
SXY0=0.,SYZ0=0.,
DSXY=81*.125,
DSYZ=41*.025
$END

```

High Penetration Mixer

```

MIXER TEST CASE
196          0.0      .215  3.14159  .0883908
  41   41     0
    1.0     1.0     2.0     0.0
$VMESH
SXY0=0.,SYZ0=0.,
DSXY=41*.25,
DSYZ=41*.025
$END

```

TABLE C.2

FILE: FLOLS DATA

FLOMIX TEST CASE
LOW PENETRATION PLANAR CASE

420	2	1.4	53.3	14.7
15.063	520.	1.4	53.3	14.7
15.063	520.	1.4	53.3	14.7
129	129 6.0	20.0	129.0	138.0
2	100 50			
1.7	0	.15	1.0	1.0
0	0	0	0	0.
0	20	9		
6.00000	129.69016	133.69014	137.69016	133.69014 .5
6.51547	129.69016	133.69014	137.69016	133.69014 .5
6.92784	129.69016	133.69015	137.69016	133.69013 .5
7.44330	129.69016	133.69016	137.69016	133.69012 .5
7.95877	129.69016	133.69022	137.69016	133.69006 .5
8.47423	129.69016	133.69046	137.69016	133.68982 .5
8.98969	129.69016	133.69135	137.69016	133.68893 .5
9.50516	129.69016	133.69393	137.69016	133.68635 .5
10.02862	129.69016	133.70013	137.69016	133.68015 .5
10.43299	129.69016	133.70943	137.69016	133.67085 .5
10.94845	129.69016	133.72858	137.69016	133.65170 .5
11.46392	129.69016	133.75734	137.69016	133.62294 .5
11.97928	129.69016	133.79520	137.69016	133.58508 .5
12.49485	129.69016	133.84000	137.69016	133.54028 .5
13.01031	129.69016	133.88905	137.69016	133.49123 .5
13.52577	129.69016	133.94014	137.69016	133.44014 .5
13.93814	129.69016	134.04412	137.69016	133.39866 .5
14.55670	129.69016	134.04412	137.69016	133.33616 .5
14.76907	129.69016	134.08584	137.69016	133.29444 .5
15.48454	129.69016	134.13799	137.69016	133.24229 .5
16.00000	129.69016	134.19014	137.69016	133.19014 .5
17.000	129.69016	0.0	137.69016	0.0 .5
18.000	129.69016	0.0	137.69016	0.0 .5
19.000	129.69016	0.0	137.69016	0.0 .5
20.000	129.69016	0.0	137.69016	0.0 .5
21.000	129.69016	0.0	137.69016	0.0 .5
22.000	129.69016	0.0	137.69016	0.0 .5

FILE: FLOHS

FLOMIX TEST CASE
HIGH PENETRATION PLANAR CASE

420	2	1.4	53.3	14.7
15.063	520.	1.4	53.3	14.7
15.063	520.	1.4	53.3	14.7
129	129 6.0	20.0	129.0	138.0
2	100 50			
1.7	0	.15	1.0	1.0
0	0	0	0	0.
0	20	9		
6.00000	129.69016	133.69014	137.69016	133.69014 .5
6.82976	129.69016	133.69014	137.69016	133.69014 .5
7.65953	129.69016	133.69022	137.69016	133.69006 .5
8.45113	129.69016	133.69165	137.69016	133.68855 .5
9.01237	129.69016	133.69585	137.69016	133.68436 .5
9.43681	129.69016	133.70370	137.69016	133.67647 .5
9.77364	129.69016	133.71608	137.69016	133.66409 .5
10.04970	129.69016	133.73230	137.69016	133.64784 .5
10.27374	129.69016	133.75075	137.69016	133.62938 .5
10.46913	129.69016	133.77148	137.69016	133.60869 .5
10.65234	129.69016	133.79536	137.69016	133.58481 .5
10.82722	129.69016	133.82248	137.69016	133.55771 .5
11.00100	129.69016	133.85379	137.69016	133.52638 .5
11.17080	129.69016	133.89046	137.69016	133.48973 .5
11.36720	129.69016	133.93440	137.69016	133.44577 .5
11.56669	129.69016	133.98643	137.69016	133.39371 .5
11.77838	129.69016	134.04747	137.69016	133.33272 .5
12.00577	129.69016	134.11906	137.69016	133.26114 .5
12.26226	129.69016	134.20619	137.69016	133.17401 .5
12.56547	129.69016	134.31604	137.69016	133.06421 .5
12.93913	129.69016	134.45854	137.69016	132.92177 .5
13.41926	129.69016	134.64813	137.69016	132.73221 .5
14.12848	129.69016	134.93307	137.69016	132.44728 .5
15.03447	129.69016	135.29922	137.69016	132.08110 .5
16.00000	129.69016	135.69014	137.69016	131.69014 .5
17.000	129.69016	0.0	137.69016	0.0 .5
18.000	129.69016	0.0	137.69016	0.0 .5
19.000	129.69016	0.0	137.69016	0.0 .5
20.000	129.69016	0.0	137.69016	0.0 .5
21.000	129.69016	0.0	137.69016	0.0 .5
22.000	129.69016	0.0	137.69016	0.0 .5

ORIGINAL PAGE IS
OF POOR QUALITY

ORIGINAL PAGE IS
OF POOR QUALITY

Advanced High-Penetration Mixer

FILE: FLOSH3S

FLOMIX TEST CASE
SWIXER PLANAR CASE- SHIFTED ID WALL - SMOOTHED
240 6
15.063 520. 1.4 53.3 14.7
15.063 520. 1.4 53.3 1.
129 129 46. 72.0 160.00 173.00
3 500 400 300
1.7
0 0 0 .0
2 9 20 1
46.00000 163.37488 166.37769 171.65628 167.78468 0.47800
47.00000 163.37494 166.37761 171.66711 167.79568 0.47800
48.00000 163.37480 166.37755 171.63779 167.77484 0.47800
49.00000 163.37451 166.37752 171.57178 167.72076 0.47800
50.00000 163.37317 166.37738 171.47949 167.63188 0.47800
51.00000 163.37030 166.37697 171.37367 167.51093 0.47800
52.00000 163.36636 166.37650 171.26395 167.36646 0.47800
53.00000 163.36424 166.37714 171.15453 167.20886 0.47800
54.00000 163.36908 166.38142 171.04553 167.04588 0.47800
54.69400 163.38010 166.38870 170.96977 166.93179 0.47800
55.00000 163.38974 166.39542 170.93645 166.88168 0.47800
55.50000 163.42340 166.43161 170.88353 166.79793 0.47800
56.00000 163.47456 166.50946 170.83240 166.70628 0.47800
56.50000 163.53491 166.62613 170.78244 166.60651 0.47800
57.00000 163.59593 166.77397 170.73305 166.50020 0.47800
57.50000 163.65128 166.94260 170.68384 166.38916 0.47800
58.00000 163.69745 167.12248 170.63478 166.27350 0.47800
58.50000 163.73312 167.30766 170.58572 166.15175 0.47800
59.00000 163.75940 167.49449 170.53654 166.02357 0.47800
60.00000 163.79483 167.86079 170.43784 165.75305 0.47800
61.00000 163.81393 168.20750 170.33960 165.46765 0.47800
62.00000 163.82021 168.52548 170.24336 165.16980 0.47800
63.00000 163.81792 168.80206 170.15126 164.86266 0.47800
63.50000 163.81441 168.92041 170.10951 164.70671 0.47800
64.00000 163.80934 169.01595 170.07433 164.55130 0.47800
64.50000 163.79921 169.08305 170.05049 164.39755 0.47800
65.00290 163.77931 169.12567 170.03697 164.24394 0.47800
65.50000 163.74620 169.14842 170.03061 164.09222 0.47800
66.00000 163.69589 169.15468 170.02792 163.93938 0.47800
66.50000 163.62627 0.0 170.02698 0.0 0.47800
67.00000 163.53798 0.0 170.02684 0.0 0.47800
67.50000 163.43597 0.0 170.02701 0.0 0.47800
68.00000 163.32953 0.0 170.02719 0.0 0.47800
69.00000 163.12901 0.0 170.02736 0.0 0.47800
70.00000 162.95023 0.0 170.02742 0.0 0.47800
71.00000 162.79468 0.0 170.02742 0.0 0.47800
72.00000 162.66516 0.0 170.02742 0.0 0.47800
73.00000 162.56242 0.0 170.02742 0.0 0.47800
74.00000 162.48674 0.0 170.02742 0.0 0.47800
75.00000 162.43785 0.0 170.02745 0.0 0.47800
76.00000 162.41566 0.0 170.02750 0.0 0.47800
76.33270 162.41415 0.0 170.02759 0.0 0.47800

END MIXER

TABLE D.1.1
 Low Penetration Lobed Mixer, $(u+U_\infty)/U_\infty$

Normalized Axial Velocity LV Data

Axial Location $\bar{X} = 0.36$

Z	Y=0.72	Z	Y=0.62	Z	Y=0.52	Z	Y=0.42
0.10	0.992	0.00	0.984	0.00	0.572	0.00	0.703
0.20	0.996	0.07	0.986	0.09	0.613	0.09	0.700
		0.13	0.989	0.11	0.613	0.11	0.684
		0.17	0.992	0.14	0.695	0.15	0.620
		0.23	0.993	0.16	0.769	0.17	0.594
		0.27	0.993	0.19	0.868	0.19	0.600
		0.33	0.996	0.21	0.918	0.21	0.593
		0.37	0.996	0.29	0.980	0.24	0.612
		0.43	0.997	0.31	0.984	0.26	0.665
				0.39	0.988	0.29	0.805
				0.41	0.988	0.31	0.878
				0.49	0.990	0.39	0.977
						0.41	0.983
						0.49	0.988
Z	Y=0.32	Z	Y=0.22	Z	Y=0.12	Z	Y=0.08
0.00	0.822	0.00	0.899	0.00	0.956	0.02	0.983
0.09	0.824	0.08	0.901	0.08	0.953	0.08	0.978
0.11	0.807	0.12	0.887	0.12	0.943	0.18	0.957
0.19	0.766	0.18	0.875	0.18	0.936	0.23	0.928
0.21	0.727	0.22	0.852	0.22	0.912	0.28	0.908
0.24	0.687	0.28	0.751	0.28	0.881	0.32	0.834
0.26	0.632	0.32	0.698	0.32	0.844	0.33	0.837
0.28	0.593	0.33	0.616	0.37	0.728	0.38	0.761
0.29	0.592	0.35	0.596	0.38	0.667	0.41	0.628
0.31	0.601	0.36	0.598	0.41	0.586	0.42	0.612
0.34	0.679	0.38	0.620	0.42	0.580	0.43	0.564
0.36	0.764	0.42	0.713	0.43	0.584	0.48	0.624
0.39	0.876	0.48	0.910	0.45	0.593		
0.41	0.922			0.47	0.671		
0.49	0.979			0.48	0.723		
Z	Y=0.02	Z	Y=-0.08	Z	Y=-0.22	Z	Y=-0.32
0.00	0.990	0.00	0.996	0.02	0.994	0.02	0.991
0.08	0.990	0.08	0.990	0.05	0.991	0.08	0.990
0.12	0.985	0.12	0.991	0.08	0.993	0.13	0.990
0.18	0.981	0.18	0.988	0.15	0.989	0.18	0.991
0.22	0.970	0.22	0.988	0.18	0.993	0.23	0.989
0.28	0.954	0.28	0.982	0.25	0.989	0.28	0.989
0.32	0.927	0.32	0.973	0.28	0.991	0.33	0.989
0.38	0.862	0.37	0.948	0.35	0.986	0.38	0.989
0.42	0.781	0.38	0.949	0.38	0.985	0.43	0.988
0.43	0.735	0.42	0.904	0.45	0.973	0.48	0.984
0.46	0.632	0.47	0.837	0.48	0.937		
0.48	0.587	0.48	0.785				
0.50	0.596						

TABLE D.1.1 (Continued)
 Low Penetration Lobed Mixer, $(u+U_\infty)/U_\infty$

Normalized Axial Velocity LV Data

Axial Location $\bar{X} = 0.36$

(Continued)

Z	Y=-0.42	Z	Y=-0.52	Z	Y=-0.62	Z	Y=-0.72
0.00	0.998	0.00	0.998	0.10	1.000	0.10	1.000
0.10	0.998	0.10	1.000	0.30	1.000	0.30	1.000
0.20	0.998	0.20	1.000	0.50	0.998	0.50	0.997
0.30	0.996	0.30	0.999				
0.40	0.996	0.40	0.998				
0.50	0.993	0.50	0.997				
		Y	Z=0.0	Y	Z=1.0		
		0.62	0.984	0.62	1.000		
		0.57	0.902	0.52	1.000		
		0.54	0.646	0.42	0.999		
		0.52	0.572	0.32	0.998		
		0.47	0.625	0.22	0.997		
		0.42	0.703	0.12	0.995		
		0.32	0.822	0.02	0.992		
		0.22	0.899	-0.08	0.976		
		0.12	0.956	-0.18	0.920		
		0.02	0.990	-0.28	0.841		
		-0.08	0.996	-0.38	0.710		
		-0.18	0.997	-0.48	0.567		
		-0.28	0.997	-0.50	0.531		
		-0.38	0.999	-0.53	0.566		
		-0.48	1.000	-0.58	0.931		
		-0.58	1.000	-0.68	0.988		
		-0.68	1.000				

TABLE D.1.2
 Low Penetration Lobed Mixer (v/U_∞)
 Normalized Transverse Velocity LV Data
 Axial Location $\bar{x} = 0.36$

Z (IN)		0.0	0.1	0.2	0.3	0.4	0.5
J	Y (IN)						
1	2.00	-0.0071	-0.0057	-0.0057	-0.0034	-0.0019	-0.0026
2	1.50	-0.0057	-0.0063	-0.0072	-0.0032	-0.0029	-0.0042
3	1.00	-0.0042	-0.0045	-0.0059	-0.0038	-0.0059	-0.0070
4	0.90	-0.0013	-0.0037	-0.0052	-0.0038	-0.0070	-0.0088
5	0.80	0.0027	0.0016	-0.0029	-0.0029	-0.0065	-0.0105
6	0.70	0.0099	0.0068	0.0002	-0.0027	-0.0094	-0.0137
7	0.60	0.0268	0.0223	0.0062	-0.0040	-0.0134	-0.0185
8	0.50	0.0425	0.0291	0.0042	-0.0072	-0.0206	-0.0249
9	0.40	0.0750	0.0784	0.0426	-0.0126	-0.0366	-0.0351
10	0.30	0.0846	0.0868	0.0774	0.0411	-0.0387	-0.0455
11	0.20	0.0835	0.0854	0.0845	0.0749	0.0086	-0.0533
12	0.10	0.0794	0.0805	0.0802	0.0822	0.0573	-0.0375
13	0.00	0.0739	0.0728	0.0740	0.0779	0.0729	0.0181
14	-0.10	0.0653	0.0643	0.0649	0.0691	0.0704	0.0547
15	-0.20	0.0594	0.0589	0.0583	0.0604	0.0625	0.0653
16	-0.30	0.0513	0.0516	0.0511	0.0532	0.0544	0.0594
17	-0.40	0.0454	0.0453	0.0451	0.0465	0.0466	0.0509
18	-0.50	0.0392	0.0382	0.0380	0.0403	0.0401	0.0433
19	-0.60	0.0332	0.0333	0.0323	0.0348	0.0332	0.0366
20	-0.70	0.0290	0.0284	0.0275	0.0302	0.0295	0.0314
21	-0.80	0.0247	0.0239	0.0239	0.0272	0.0256	0.0281
22	-0.90	0.0210	0.0211	0.0204	0.0225	0.0216	0.0253
23	-1.00	0.0182	0.0180	0.0165	0.0196	0.0191	0.0224
24	-1.50	0.0081	0.0079	0.0077	0.0117	0.0118	0.0159
25	-2.00	0.0050	0.0048	0.0040	0.0082	0.0080	0.0116
26	-2.50	0.0026	0.0029	0.0034	0.0059	0.0070	0.0109

TABLE D.1.2 (Continued)
 Low Penetration Lobed Mixer (v/U_∞)
 Normalized Transverse Velocity LV Data
 Axial Location $\bar{X} = 0.36$

Z (IN)		0.6	0.7	0.8	0.9	1.0
J	Y (IN)					
1	2.00	-0.0047	-0.0059	-0.0056	-0.0053	-0.0051
2	1.50	-0.0055	-0.0099	-0.0096	-0.0096	-0.0105
3	1.00	-0.0102	-0.0174	-0.0185	-0.0193	-0.0198
4	0.90	-0.0124	-0.0208	-0.0210	-0.0230	-0.0228
5	0.80	-0.0151	-0.0232	-0.0264	-0.0270	-0.0261
6	0.70	-0.0182	-0.0285	-0.0303	-0.0317	-0.0313
7	0.60	-0.0232	-0.0336	-0.0361	-0.0369	-0.0368
8	0.50	-0.0293	-0.0400	-0.0415	-0.0426	-0.0418
9	0.40	-0.0363	-0.0483	-0.0481	-0.0482	-0.0500
10	0.30	-0.0462	-0.0552	-0.0554	-0.0551	-0.0560
11	0.20	-0.0554	-0.0623	-0.0624	-0.0627	-0.0634
12	0.10	-0.0605	-0.0723	-0.0684	-0.0693	-0.0692
13	0.00	-0.0596	-0.0808	-0.0788	-0.0749	-0.0738
14	-0.10	-0.0213	-0.0753	-0.0847	-0.0838	-0.0838
15	-0.20	0.0378	-0.0460	-0.0857	-0.0872	-0.0856
16	-0.30	0.0534	0.0179	-0.0651	-0.0872	-0.0912
17	-0.40	0.0471	0.0381	0.0100	-0.0693	-0.0787
18	-0.50	0.0369	0.0284	0.0196	0.0071	-0.0076
19	-0.60	0.0306	0.0203	0.0094	-0.0022	-0.0108
20	-0.70	0.0258	0.0154	0.0091	0.0019	0.0001
21	-0.80	0.0213	0.0132	0.0090	0.0048	0.0028
22	-0.90	0.0182	0.0116	0.0076	0.0060	0.0046
23	-1.00	0.0178	0.0105	0.0074	0.0055	0.0056
24	-1.50	0.0114	0.0058	0.0050	0.0055	0.0059
25	-2.00	0.0077	0.0042	0.0028	0.0047	0.0039
26	-2.50	0.0061	0.0034	0.0015	0.0027	0.0041

TABLE D.1.2 (Continued)

Low Penetration Lobed Mixer (v/U_∞)

Normalized Transverse Velocity LV Data

Axial Location $\bar{X} = 0.36$

	z	0.0	0.1	0.2	0.3	0.4	0.5
J	Y						
1	2.00	-0.0070	-0.0050	-0.0040	-0.0030	-0.0050	-0.0030
2	1.50	-0.0060	-0.0050	-0.0060	-0.0040	-0.0070	-0.0040
3	1.00	-0.0040	-0.0050	-0.0060	-0.0070	-0.0120	-0.0070
4	0.90	-0.0010	-0.0050	-0.0060	-0.0080	-0.0120	-0.0090
5	0.80	0.0030	-0.0020	-0.0060	-0.0080	-0.0140	-0.0100
6	0.78		-0.0010	-0.0030	-0.0080	-0.0120	
7	0.70	0.0100	0.0020	-0.0040	-0.0080	-0.0170	-0.0140
8	0.68		0.0060	-0.0020	-0.0070	-0.0140	
9	0.62		0.0260	0.0380	-0.0100	-0.0180	-0.0240
10	0.60	0.0270	0.0120	-0.0070	-0.0120	-0.0220	-0.0190
11	0.58	0.0170	0.0140	0.0000	-0.0110	-0.0170	
12	0.52	0.0210	0.0200	0.0370	-0.0140	-0.0230	-0.0280
13	0.50	0.0430	0.0110	-0.0080	-0.0170	-0.0290	-0.0250
14	0.48	0.0480	0.0170	-0.0190	-0.0160	-0.0210	
15	0.42	0.0690	0.0720	0.0340	-0.0270	-0.0310	-0.0350
16	0.40	0.0750	0.0740	0.0160	-0.0250	-0.0420	-0.0350
17	0.38	0.0760	0.0700	0.0530	-0.0280	-0.0350	
18	0.32	0.0800	0.0780	0.0770	0.0300	-0.0440	-0.0440
19	0.30	0.0850	0.0870	0.0710	0.0120	-0.0460	-0.0460
20	0.28	0.0780	0.0780	0.0690	0.0370	-0.0510	
21	0.22	0.0770	0.0790	0.0780	0.0660	-0.0070	-0.0490
22	0.20	0.0840	0.0860	0.0850	0.0600	-0.0130	-0.0530
23	0.18	0.0790	0.0770	0.0740	0.0590	0.0120	
24	0.12	0.0750	0.0740	0.0760	0.0700	0.0390	-0.0380
25	0.10	0.0790	0.0820	0.0820	0.0790	0.0390	-0.0380
26	0.08	0.0750	0.0750	0.0750	0.0660	0.0430	
27	0.02	0.0680	0.0690	0.0700	0.0710	0.0640	0.0010
28	0.00	0.0740	0.0740	0.0760	0.0790	0.0670	0.0180
29	-0.02	0.0700	0.0680	0.0680	0.0700	0.0560	
30	-0.08	0.0610	0.0600	0.0600	0.0610	0.0630	0.0530
31	-0.10	0.0650	0.0660	0.0660	0.0700	0.0650	0.0550
32	-0.12	0.0590	0.0590	0.0570	0.0560	0.0570	
33	-0.18	0.0530	0.0530	0.0520	0.0490	0.0500	0.0500
34	-0.20	0.0590	0.0610	0.0600	0.0610	0.0590	0.0650
35	-0.22	0.0540	0.0530	0.0520	0.0500	0.0520	
36	-0.28	0.0470	0.0460	0.0450	0.0430	0.0430	0.0440
37	-0.30	0.0510	0.0530	0.0530	0.0540	0.0500	0.0590
38	-0.32	0.0490	0.0480	0.0460	0.0440	0.0440	
39	-0.38	0.0420	0.0410	0.0410		0.0350	0.0330

TABLE D.1.2 (Continued)
 Low Penetration Lobed Mixer (v/U_∞)
 Normalized Transverse Velocity LV Data
 Axial Location $\bar{x} = 0.36$

(Continued)

		z	0.0	0.1	0.2	0.3	0.4	0.5
J	Y							
40	-0.40		0.0450	0.0460	0.0460	0.0470	0.0410	0.0510
41	-0.42		0.0450	0.0440	0.0410	0.0410	0.0380	
42	-0.48		0.0380	0.0370	0.0360		0.0300	0.0260
43	-0.50		0.0390	0.0400	0.0400	0.0400	0.0340	0.0430
44	-0.52		0.0390	0.0380	0.0360	0.0330	0.0310	
45	-0.58		0.0320	0.0320	0.0310		0.0250	0.0220
46	-0.60		0.0330	0.0350	0.0340	0.0340	0.0280	0.0370
47	-0.62		0.0350	0.0340	0.0320	0.0300	0.0260	
48	-0.68		0.0280	0.0290	0.0270		0.0210	0.0180
49	-0.70		0.0290	0.0300	0.0290	0.0290	0.0240	0.0310
50	-0.78		0.0240	0.0240	0.0220	0.0170	0.0180	0.0150
51	-0.80		0.0250	0.0250	0.0250	0.0230	0.0200	0.0280
52	-0.90		0.0210	0.0220	0.0200	0.0210	0.0170	0.0250
53	-1.00		0.0180	0.0180	0.0180	0.0170	0.0140	0.0220
54	-1.50		0.0080	0.0090	0.0090	0.0100	0.0090	0.0160
55	-2.00		0.0050	0.0050	0.0050	0.0060	0.0070	0.0120
56	-2.50		0.0030	0.0030	0.0030	0.0060	0.0070	0.0110

TABLE D.1.3
 Low Penetration Lobed Mixer (w/U_∞)
 Normalized Spanwise Velocity LV Data
 Axial Location $\bar{X} = 0.36$

		z	0.0	0.1	0.2	0.3	0.4	0.5
J	Y							
1	0.00	0.0000	-0.0010	-0.0050	-0.0110	-0.0120	0.0000	
2	0.10	0.0010	-0.0010	-0.0100	-0.0140	-0.0020	0.0060	
3	0.20	0.0000	-0.0040	-0.0080	-0.0030	0.0080	0.0120	
4	0.30	0.0020	-0.0010	-0.0040	0.0060	0.0170	0.0180	
5	0.40	0.0000	0.0010	-0.0040	0.0230	0.0250	0.0200	
6	0.50	0.0000	0.0130	0.0270	0.0300	0.0230	0.0200	
7	0.60	0.0010	0.0120	0.0230	0.0230	0.0210	0.0190	
8	0.70	0.0000	0.0060	0.0120	0.0160	0.0150	0.0140	

		z	0.6	0.7	0.8	0.9
J	Y					
1	0.00	0.0120	0.0110	0.0050	0.0010	
2	0.10	0.0140	0.0070	0.0020	0.0000	
3	0.20	0.0120	0.0070	0.0030	0.0000	
4	0.30	0.0130	0.0090	0.0060	0.0010	
5	0.40	0.0150	0.0110	0.0080	0.0050	
6	0.50	0.0150	0.0130	0.0080	0.0050	
7	0.60	0.0160	0.0130	0.0100	0.0080	
8	0.70	0.0130	0.0110	0.0080	0.0060	

TABLE D.1.4

Low Penetration Lobed Mixer (\overline{PT})

Normalized Total Pressure Data

Axial Location $\bar{X} = 0.01$

		z	0.00	0.05	0.10	0.15	0.20	0.25
J	Y							
1	0.70		0.9990	1.0000	1.0000	1.0000	1.0000	1.0000
2	0.60		0.9640	0.9670	0.9830	0.9940	0.9980	1.0000
3	0.50		0.3010	0.2870	0.2800	0.7270	0.8430	0.9290
4	0.40		0.5150	0.5070	0.4710	0.4160	0.3550	0.4400
5	0.30		0.6900	0.6810	0.6610	0.6210	0.5700	0.4900
6	0.20		0.8370	0.8180	0.8030	0.7790	0.7460	0.6930
7	0.10		0.9500	0.9370	0.9260	0.9040	0.8840	0.8470
8	0.00		0.9940	0.9890	0.9850	0.9780	0.9690	0.9480
9	-0.10		0.9990	0.9990	0.9990	0.9980	0.9970	0.9940
10	-0.20		0.9990	0.9990	0.9990	0.9990	0.9990	0.9990
11	-0.30		0.9990	1.0000	1.0000	1.0000	1.0000	1.0000
12	-0.40		0.9990	0.9990	1.0000	0.9990	1.0000	0.9990
13	-0.50		0.9990	0.9990	1.0000	0.9990	1.0000	0.9990
14	-0.60		0.9990	0.9990	1.0000	0.9990	1.0000	0.9990
		z	0.30	0.35	0.40	0.45	0.50	
J	Y							
1	0.70		1.0000	1.0000	1.0000	1.0000	1.0000	
2	0.60			0.9990	0.9990	0.9990	0.9990	
3	0.50		0.9760	0.9920	0.9970	0.9990	0.9990	
4	0.40		0.7680	0.8940	0.9540	0.9850	0.9960	
5	0.30		0.3770	0.5920	0.7440	0.8670	0.9410	
6	0.20		0.6040	0.4880	0.1280	0.5920	0.7700	
7	0.10		0.7830	0.6540	0.5690	0.1910	0.5330	
8	0.00		0.9150	0.8520	0.7710	0.6460	0.4780	
9	-0.10		0.9850	0.9640	0.9170	0.8260	0.6740	
10	-0.20		0.9990	0.9960	0.9890	0.9640	0.8970	
11	-0.30		1.0000	1.0000	0.9990	0.9980	0.9890	
12	-0.40		1.0000	0.9990	0.9990	0.9990	0.9890	
13	-0.50		1.0000	0.9990	0.9990	0.9990	0.9890	
14	-0.60		1.0000	0.9990	0.9990	0.9990	0.9890	

TABLE D.2.1
 High Penetration Lobed Mixer, $(u+U_\infty)/U_\infty$

Normalized Axial Velocity LV Data

Axial Location $\bar{X} = 0.36$

		z	0.0	0.1	0.2	0.3	0.4	0.5
J	Y							
1	2.10		0.9820	0.9850	0.9880	0.9992	0.9960	
2	2.00		0.4010	0.5020	0.9820	0.9890	0.9940	
3	1.90		0.5310	0.4970	0.8460	0.9870	0.9920	
4	1.80		0.6270	0.6170	0.6060	0.9900	0.9960	
5	1.70		0.7110	0.7140	0.5440	0.9870	0.9930	
6	1.60		0.7530	0.7530	0.6480	0.9790	0.9930	
7	1.50		0.8110	0.8090	0.7360	0.8360	0.9910	
8	1.40		0.8650	0.8640	0.8090	0.7080	0.9940	
9	1.30		0.9080	0.9010	0.8570	0.6450	0.9890	
10	1.20		0.9550	0.9490	0.9200	0.6560	0.9890	
11	1.10		0.9740	0.9730	0.9540	0.7130	0.9840	
12	1.00		0.9790	0.9770	0.9660	0.7810	0.9230	
13	0.90		0.9820	0.9800	0.9740	0.9160	0.8360	
14	0.70		0.9860	0.9850	0.9830	0.9730	0.7050	
15	0.50		0.9940	0.9920	0.9900	0.9870	0.8060	
16	0.30		1.0000	0.9980	0.9970	0.9930	0.9800	
17	0.10		1.0000	1.0000	1.0000	0.9950	0.9880	
18	-0.10		1.0000	0.9950	0.9920	0.9850	0.9850	0.7840
19	-0.30		1.0000	0.9980	0.9960	0.9900	0.9870	0.8500
20	-0.50		1.0000	0.9980	0.9980	0.9930	0.9910	0.9770
21	-0.70		1.0000	1.0000	0.9990	0.9970	0.9940	0.9900
22	-0.90		1.0000	1.0000	1.0000	0.9970	0.9940	0.9910
23	-1.00		1.0000	1.0000	1.0000	1.0000	0.9960	0.9930
24	-1.10		1.0000	1.0000	1.0000	1.0000	0.9950	0.9930
25	-1.20		1.0000	1.0000	1.0000	1.0000	0.9980	0.9940
26	-1.30		1.0000	1.0000	1.0000	1.0000	0.9960	0.9930
27	-1.40		1.0000	1.0000	1.0000	1.0000	0.9990	0.9970
28	-1.50		1.0000	1.0000	1.0000	1.0000	1.0000	0.9970
29	-1.60		1.0000	1.0000	1.0000	1.0000	1.0000	0.9970
30	-1.70		1.0000	1.0000	1.0000	1.0000	1.0000	0.9970
31	-1.80		1.0000	1.0000	1.0000	1.0000	1.0000	0.9970
32	-1.90		1.0000	1.0000	1.0000	1.0000	1.0000	0.9980
33	-2.00		1.0000	1.0000	1.0000	1.0000	1.0000	0.9960
34	-2.10		1.0000	1.0000	1.0000	1.0000	1.0000	0.9980

TABLE D.2.2
 High Penetration Lobed Mixer (v/U_∞)
 Normalized Spanwise Velocity LV Data
 Axial Location $\bar{X} = 0.36$

	Z	0.6	0.7	0.8	0.9	1.0
J	Y					
1	-2.2	0.0050	0.0210	-0.0460	-0.0610	-0.0740
2	-2.0	0.0280	0.0170	-0.0150	-0.0920	-0.1520
3	-1.8	0.0670	0.0830	0.0210	-0.2750	-0.2810
4	-1.6	0.0910	0.0960	-0.0630	-0.3200	-0.3120
5	-1.4	0.1030	0.0650	-0.2730	-0.3240	-0.3120
6	-1.2	0.1170	0.0210	-0.3100	-0.3210	-0.3150
7	-1.0	0.1260	-0.0610	-0.3280	-0.3180	-0.3130
8	-0.8	0.0850	-0.2170	-0.3150	-0.3040	-0.3020
9	-0.6	0.0080	-0.2930	-0.3030	-0.2940	-0.2920
10	-0.4	-0.0280	-0.2940	-0.2930	-0.2840	-0.2820
11	-0.2	-0.1130	-0.2830	-0.2830	-0.2730	-0.2720
12	-0.0	-0.2360	-0.2690	-0.2670	-0.2580	-0.2590
13	0.2	-0.2500	-0.2520	-0.2510	-0.2420	-0.2440
14	0.4	-0.2380	-0.2350	-0.2350	-0.2280	-0.2320
15	0.6	-0.2180	-0.2180	-0.2180	-0.2100	-0.2120
16	0.8	-0.2020	-0.2010	-0.2010	-0.1970	-0.1990
17	1.0	-0.1900	-0.1840	-0.1820	-0.1750	-0.1780
18	1.2	-0.1660	-0.1640	-0.1610	-0.1550	-0.1560
19	1.4	-0.1440	-0.1410	-0.1470	-0.1330	-0.1340
20	1.6	-0.1190	-0.1160	-0.1170	-0.1090	-0.1110
21	1.8	-0.0910	-0.0910	-0.0930	-0.0870	-0.0890
22	2.0	-0.0620	-0.0660	-0.0690	-0.0660	-0.0690
23	2.2	-0.0340	-0.0470	-0.0560	-0.0480	-0.0520

TABLE D.2.3

High Penetration Lobed Mixer (w/U_{∞})

Normalized Spanwise Velocity LV Data

Axial Location $\bar{X} = 0.36$

		z	0.0	0.1	0.2	0.3	0.4	0.5
J	Y							
1	0.00		0.0020	-0.0030	-0.0100	-0.0190	-0.0390	0.0050
2	0.20		0.0030	-0.0020	-0.0100	-0.0080	-0.0490	0.0190
3	0.40		0.0040	-0.0010	-0.0080	-0.0620	-0.0280	0.0200
4	0.60		0.0030	-0.0020	-0.0080	-0.0400	0.0070	0.0160
5	0.80		0.0040	0.0010	-0.0070	-0.0650	0.0210	0.0180
6	1.00		0.0010	0.0060	-0.0020	-0.0660	0.0270	0.0200
7	1.20		0.0030	-0.0030	-0.0040	0.0140	0.0360	0.0270
8	1.40		-0.0010	0.0000	-0.0310	0.0500	0.0390	0.0300
9	1.60		-0.0030	-0.0040	-0.0170	0.0580	0.0460	0.0360
10	1.80		0.0030	-0.0010	0.0910	0.0760	0.0600	0.0440
11	2.00		0.0200	0.0100	0.1080	0.0880	0.0660	0.0520
12	2.20		0.0080	0.0060	0.0310	0.0390	0.0370	0.0330
13	2.40		0.0030	0.0030	0.0110	0.0170	0.0190	0.0190
		z	0.6	0.7	0.8	0.9	1.0	
J	Y							
1	0.00		0.0040	0.0050	0.0000	-0.0020	0.0060	
2	0.20		0.0140	0.0070	0.0010	-0.0030	0.0030	
3	0.40		0.0120	0.0070	0.0010	-0.0030	0.0040	
4	0.60		0.0100	0.0050	0.0000	-0.0040	0.0030	
5	0.80		0.0120	0.0060	0.0010	-0.0040	0.0040	
6	1.00		0.0140	0.0090	0.0030	-0.0040	0.0040	
7	1.20		0.0200	0.0130	0.0040	-0.0030	0.0030	
8	1.40		0.0220	0.0130	0.0050	-0.0030	0.0040	
9	1.60		0.0250	0.0180	0.0080	-0.0030	0.0030	
10	1.80		0.0340	0.0230	0.0110	0.0020	-0.0020	
11	2.00		0.0380	0.0280	0.0190	0.0090	0.0000	
12	2.20		0.0250	0.0190	0.0140	0.0040	0.0000	
13	2.40		0.0160	0.0140	0.0110	0.0060	0.0000	

TABLE D.2.4

High Penetration Lobed Mixer (\overline{PT})

Normalized Total Pressure Data

Axial Location $\bar{X} = 0.07$

	Z	0.0	0.1	0.2	0.3	0.4	0.5
J	Y						
1	2.20	1.0000	1.0000	1.0000	1.0000	1.0000	1.0000
2	2.10	1.0000	1.0000	1.0000	1.0000	1.0000	1.0000
3	2.00	0.1470	0.2030	1.0000	1.0000	1.0000	1.0000
4	1.90	0.2950	0.3590	0.9170	1.0000	1.0000	1.0000
5	1.80	0.4430	0.5080	0.0360	1.0000	1.0000	1.0000
6	1.70	0.5630	0.6320	0.3620	1.0000	1.0000	1.0000
7	1.60	0.6620	0.7320	0.5040	1.0000	1.0000	1.0000
8	1.50	0.7500	0.8190	0.6270	1.0000	1.0000	1.0000
9	1.40	0.8410	0.9050	0.7540	0.2830	1.0000	1.0000
10	1.30	0.9400	0.9720	0.8660	0.0220	1.0000	1.0000
11	1.20	0.9930	0.9950	0.9420	0.5470	1.0000	1.0000
12	1.10	1.0000	1.0000	0.9790	0.6700	1.0000	1.0000
13	1.00	1.0000	1.0000	0.9930	0.7900	1.0000	1.0000
14	0.90	1.0000	1.0000	1.0000	0.9000	0.9750	1.0000
15	0.80	1.0000	1.0000	1.0000	0.9710	0.5380	1.0000
16	0.70	1.0000	1.0000	1.0000	1.0000	0.0000	1.0000
17	0.60	1.0000	1.0000	1.0000	1.0000	0.4020	1.0000
18	0.50	1.0000	1.0000	1.0000	1.0000	0.6680	1.0000
19	0.40	1.0000	1.0000	1.0000	1.0000	0.9450	1.0000
20	0.30	1.0000	1.0000	1.0000	1.0000	0.9520	0.9780
21	0.20	1.0000	1.0000	1.0000	1.0000	0.9930	0.7140
22	0.10	1.0000	1.0000	1.0000	1.0000	1.0000	0.0220
23	0.00	1.0000	1.0000	1.0000	1.0000	1.0000	-0.0400
24	-0.10	1.0000	1.0000	1.0000	1.0000	1.0000	-0.0400
25	-0.20	1.0000	1.0000	1.0000	1.0000	1.0000	0.7140
26	-0.30	1.0000	1.0000	1.0000	1.0000	1.0000	0.9890
27	-0.40	1.0000	1.0000	1.0000	1.0000	1.0000	1.0000
28	-0.50	1.0000	1.0000	1.0000	1.0000	1.0000	1.0000
29	-0.60	1.0000	1.0000	1.0000	1.0000	1.0000	1.0000
30	-0.80	1.0000	1.0000	1.0000	1.0000	1.0000	1.0000
31	-1.00	1.0000	1.0000	1.0000	1.0000	1.0000	1.0000
32	-1.50	1.0000	1.0000	1.0000	1.0000	1.0000	1.0000
33	-2.00	1.0000	1.0000	1.0000	1.0000	1.0000	1.0000
34	-2.50	1.0000	1.0000	1.0000	1.0000	1.0000	1.0000

TABLE D.3.1
 ADVANCED HIGH PENETRATION
 Lobed Mixer ($u+U_{\infty}/U_{\infty}$)
 Normalized Axial Velocity LV Data
 Axial Location $\bar{X} = 0.05$

	z	0.0	0.1	0.2	0.3	0.4	0.5
J	Y						
1	1.40	1.4862	1.5098	1.4853	1.4678	1.4280	1.3977
2	1.30	1.4937	1.5098	1.5170	1.5064	1.4963	1.4813
3	1.20	0.8334	0.6550	0.2084	1.4399	1.5064	1.4942
4	1.10	1.0074	1.1527	1.1828	0.7170	1.3338	1.5008
5	1.00	1.3215	1.3321	1.4209	1.2326	0.4931	1.4915
6	0.90	1.4303	1.4408	1.4680	1.3610	1.1013	1.0953
7	0.80	1.4783	1.4833	1.4851	1.4165	1.1767	0.7839
8	0.70	1.4809	1.4860	1.4864	1.4316	1.1800	0.7012
9	0.60	1.4788	1.4870	1.4872	1.4467	1.1956	0.6560
10	0.50	1.4775	1.4858	1.4861	1.4664	1.2045	0.6310
11	0.40	1.4789	1.4834	1.4844	1.4751	1.2308	0.6472
12	0.30	1.4771	1.4831	1.4878	1.4845	1.2216	0.6799
13	0.20	1.4627	1.4858	1.4875	1.4861	1.2446	0.6877
14	0.10	1.4796	1.4859	1.4895	1.4941	1.2761	0.7060
15	0.00	1.4817	1.4877	1.5059	1.4875	1.3168	0.7257
16	-0.10	1.4799	1.4849	1.4909	1.4775	1.2997	0.7373
17	-0.20	1.4788	1.4858	1.4908	1.4704	1.2850	0.7420
18	-0.30	1.4799	1.4854	1.4903	1.4705	1.2547	0.7449
19	-0.40	1.4742	1.4835	1.4875	1.4716	1.2504	0.7685
20	-0.50	1.4723	1.4808	1.4849	1.4842	1.2569	0.7518
21	-0.60	1.4669	1.4725	1.4825	1.4957	1.3025	0.7652
22	-0.70	1.4549	1.4599	1.4781	1.4963	1.3626	0.6190
23	-0.80	1.4335	1.4390	1.4579	1.4892	1.4326	0.9049
24	-0.90	1.4108	1.4121	1.4411	1.4765	1.4924	0.9664
25	-1.00	1.3694	1.3755	1.4015	1.4163	1.4935	1.4816
26	-1.10	1.3188	1.3250	1.3503	1.4016	1.4618	0.8909
27	-1.20	1.2357	1.2345	1.2752	1.3339	1.3937	1.3771
28	-1.30	1.1019	1.1061	1.1475	1.2115	1.3554	1.3771

TABLE D.3.1 (Continued)

ADVANCED HIGH PENETRATION

Lobed Mixer ($u+U_{\infty}/U_{\infty}$)

Normalized Axial Velocity LV Data

Axial Location $\bar{X} = 0.05$

	z	0.6	0.7	0.8	0.9	1.0
J	Y					
1	1.40	1.3724	1.3448	1.3177	1.3147	1.2961
2	1.30	1.4541	1.4255	1.4039	1.3982	1.3877
3	1.20	1.4850	1.4711	1.4562	1.4492	1.4431
4	1.10	1.4870	1.4789	1.4801	1.4760	1.4762
5	1.00	1.4877	1.4820	1.4778	1.4768	1.4750
6	0.90	1.4875	1.4804	1.4777	1.4740	1.4774
7	0.80	1.4835	1.4789	1.4783	1.4761	1.4752
8	0.70	1.4807	1.4787	1.4790	1.4748	1.4770
9	0.60	1.4736	1.4746	1.4751	1.4739	1.4765
10	0.50	1.4630	1.4759	1.4736	1.4720	1.4777
11	0.40	1.4534	1.4690	1.4743	1.4746	1.4787
12	0.30	1.4451	1.4690	1.4733	1.4758	1.4769
13	0.20	1.4432	1.4719	1.4719	1.4729	1.4784
14	0.10	1.4452	1.4740	1.4730	1.4735	1.4813
15	0.00	1.4476	1.4761	1.4727	1.4745	1.4809
16	-0.10	1.4396	1.4772	1.4724	1.4750	1.4816
17	-0.20	1.4405	1.4773	1.4779	1.4785	1.4848
18	-0.30	1.4350	1.4736	1.4787	1.4769	1.4880
19	-0.40	1.4342	1.4762	1.4769	1.4804	1.4893
20	-0.50	1.4159	1.4768	1.4835	1.4816	1.4922
21	-0.60	1.4111	1.4787	1.4835	1.4842	1.4924
22	-0.70	1.3791	1.4765	1.4814	1.4797	1.4792
23	-0.80	1.3217	1.4526	1.4458	1.4276	1.4243
24	-0.90	1.2010	1.4019	1.3998	1.3669	1.3578
25	-1.00	0.9248	1.2639	1.3346	1.2879	1.2666
26	-1.10	0.4463	0.7879	1.0597	1.0487	0.8842
27	-1.20	1.0587	0.8479	0.8632	0.1615	0.9435
28	-1.30	1.3858	1.4392	1.4751	1.4452	0.8920

TABLE D.3.2
ADVANCED HIGH PENETRATION

Lobed Mixer (v/U_∞)

Normalized Transverse Velocity LV Data

Axial Location $\bar{X} = 0.05$

	Z	0.0	0.1	0.2	0.3	0.4	0.5
J	Y						
1	1.34	-0.0535	-0.0503	-0.0499	-0.0512	-0.0522	-0.0512
2	1.30	-0.0875	-0.0818	-0.0761	-0.0659	-0.0653	-0.0649
3	1.20	-0.0304	-0.0223	-0.0355	-0.1132	-0.0931	-0.0984
4	1.10	0.0046	0.0295	0.0134	0.1900	-0.1448	-0.1235
5	1.00	0.0038	0.0137	0.0077	0.1113	0.1060	-0.1840
6	0.90	0.1114	0.0972	0.1028	0.1002	0.1484	0.0182
7	0.80	0.0910	0.1004	0.1066	0.1086	0.0484	0.0007
8	0.70	0.1010	0.1027	0.1031	0.1078	0.0712	0.0122
9	0.60	0.1015	0.1021	0.1021	0.1054	0.0574	-0.0018
10	0.50	0.1010	0.1032	0.1014	0.1029	0.0651	0.0022
11	0.40	0.1018	0.1036	0.1008	0.1025	0.0735	-0.0066
12	0.30	0.1018	0.1027	0.1009	0.1034	0.0790	0.0097
13	0.20	0.1023	0.1037	0.1017	0.1023	0.0825	0.0189
14	0.10	0.1036	0.1041	0.1025	0.1010	0.0753	0.0235
15	0.00	0.1035	0.1037	0.1035	0.1021	0.0798	0.0283
16	-0.10	0.1032	0.1053	0.1044	0.1057	0.0821	-0.0176
17	-0.20	0.1036	0.1039	0.1063	0.1099	0.0787	-0.0296
18	-0.30	0.1040	0.1032	0.1058	0.1106	0.0778	-0.0309
19	-0.40	0.1009	0.1028	0.1048	0.1111	0.0919	-0.0458
20	-0.50	0.0980	0.0998	0.1006	0.1080	0.0965	-0.0536
21	-0.60	0.0941	0.0950	0.0960	0.1056	0.1075	-0.0486
22	-0.70	0.0860	0.0872	0.0899	0.1020	0.1218	-0.0537
23	-0.80	0.0754	0.0793	0.0820	0.0947	0.1279	-0.0434
24	-0.90	0.0643	0.0675	0.0696	0.0799	0.1119	0.1019
25	-1.00	0.0492	0.0503	0.0490	0.0570	0.0785	0.1177
26	-1.10	0.0266	0.0130	0.0176	0.0305	0.0272	0.0358
27	-1.20	0.0127	0.0105	0.0048	0.0072	-0.0010	-0.0031
28	-1.30	-0.0059	-0.0093	-0.0149	-0.0192	-0.0208	-0.0379

TABLE D.3.2 (Continued)

ADVANCED HIGH PENETRATION

Lobed Mixer (v/U_∞)

Normalized Transverse Velocity LV Data

Axial Location $\bar{X} = 0.05$

z		0.6	0.7	0.8	0.9	1.0
J	Y					
1	1.34	-0.0482	-0.0190	-0.0549	-0.0421	-0.0508
2	1.30	-0.0557	-0.0632	-0.0205	-0.0283	-0.0256
3	1.20	-0.0187	-0.0876	0.0180	0.0034	0.0017
4	1.10	-0.1150	-0.0176	0.0118	0.0114	-0.0087
5	1.00	-0.1465	-0.0388	0.0077	-0.0160	-0.0301
6	0.90	-0.1758	-0.0391	-0.0247	-0.0119	-0.0227
7	0.80	-0.2053	-0.1791	-0.1624	-0.1590	-0.1589
8	0.70	-0.1987	-0.1880	-0.1758	-0.1711	-0.1713
9	0.60	-0.1561	-0.1898	-0.1836	-0.1796	-0.1802
10	0.50	-0.1537	-0.1924	-0.1893	-0.1872	-0.1875
11	0.40	-0.1508	-0.1975	-0.1928	-0.1894	-0.1927
12	0.30	-0.1719	-0.2033	-0.1979	-0.1966	-0.1974
13	0.20	-0.1131	-0.2047	-0.2003	-0.1998	-0.2001
14	0.10	-0.1699	-0.2063	-0.2042	-0.2026	-0.2033
15	0.00	-0.1688	-0.2090	-0.2052	-0.2055	-0.2059
16	-0.10	-0.1613	-0.2087	-0.2070	-0.2051	-0.2075
17	-0.20	-0.1595	-0.2103	-0.2101	-0.2089	-0.2105
18	-0.30	-0.1539	-0.2137	-0.2120	-0.2106	-0.2129
19	-0.40	-0.1776	-0.2162	-0.2133	-0.2126	-0.2140
20	-0.50	-0.1687	-0.2192	-0.2161	-0.2138	-0.2155
21	-0.60	-0.1830	-0.2225	-0.2187	-0.2160	-0.2159
22	-0.70	-0.1788	-0.2274	-0.2224	-0.2177	-0.2192
23	-0.80	-0.1789	-0.2293	-0.2255	-0.2187	-0.2179
24	-0.90	-0.1767	-0.2273	-0.2279	-0.2163	-0.2124
25	-1.00	-0.0023	-0.2173	-0.1855	-0.0693	-0.2019
26	-1.10	-0.0010	-0.0176	-0.0755	-0.0638	-0.2076
27	-1.20	-0.0262	-0.0177	-0.1700	-0.2169	-0.2193
28	-1.30	-0.0484	-0.0605	-0.0856	-0.1189	0.0016

Table D.3.3 (Continued)

ADVANCED HIGH PENETRATION

Lobed Mixer (w/U_∞)

Normalized Spanwise Velocity LV Data

Axial Location $\bar{X} = 0.05$

	Z (IN)	0.07	0.17	0.27	0.37	0.47
J	Y (IN)					
1	1.40	0.0028	0.0157	0.0233	0.0271	0.0285
2	1.30	0.0001	0.0158	0.0271	0.0375	0.0349
3	1.20	-0.0089	-0.0079	-0.0251	0.0323	0.0370
4	1.10	-0.0097	0.0159	0.0660	0.2186	0.0048
5	1.00	-0.0057	0.0088	0.0469	0.1004	-0.1818
6	0.90	-0.0050	0.0172	0.0346	0.0771	0.1912
7	0.80	-0.0016	0.0180	0.0345	0.0737	0.1745
8	0.70	0.0026	0.0185	0.0318	0.0614	0.1453
9	0.60	-0.0011	0.0120	0.0268	0.0657	0.1454
10	0.50	-0.0017	0.0157	0.0243	0.0527	0.1344
11	0.40	-0.0026	0.0138	0.0251	0.0606	0.1571
12	0.30	-0.0028	0.0157	0.0231	0.0549	0.1478
13	0.20	-0.0008	0.0151	0.0253	0.0614	0.1574
14	0.10	-0.0004	0.0121	0.0256	0.0641	0.1453
15	0.00	0.0002	0.0146	0.0292	0.0654	0.1066
16	-0.10	-0.0033	0.0143	0.0253	0.0654	0.1589
17	-0.20	-0.0027	0.0086	0.0222	0.0525	0.1471
18	-0.30	-0.0027	0.0116	0.0201	0.0580	0.1609
19	-0.40	-0.0034	0.0057	0.0173	0.0491	0.1069
20	-0.50	-0.0072	0.0050	0.0094	0.0513	0.1795
21	-0.60	-0.0031	-0.0010	0.0037	0.0336	0.1305
22	-0.70	-0.0108	-0.0057	-0.0061	0.0220	0.1056
23	-0.80	-0.0157	-0.0124	-0.0150	-0.0065	0.0295
24	-0.90	-0.0179	-0.0230	-0.0271	-0.0373	-0.0594
25	-1.00	-0.0174	-0.0323	-0.0423	-0.0528	-0.0751
26	-1.10	-0.0215	-0.0357	-0.0506	-0.0647	-0.0853
27	-1.20	-0.0228	-0.0498	-0.0574	-0.0734	-0.0807
28	-1.30	-0.0355	-0.0578	-0.0655	-0.0804	-0.0912

Table D.3.3 (Continued)

ADVANCED HIGH PENETRATION

Lobed Mixer (w/U_∞)

Normalized Spanwise Velocity LV Data

Axial Location $\bar{X} = 0.05$

Z (IN)		0.57	0.67	0.77	0.87	0.97
J	Y (IN)					
1	1.40	0.0171	0.0142	0.0080	-0.0019	-0.0056
2	1.30	0.0253	0.0231	0.0153	0.0012	-0.0070
3	1.20	0.0271	0.0217	0.0165	0.0079	-0.0004
4	1.10	0.0230	0.0176	0.0168	0.0093	0.0035
5	1.00	0.0032	0.0097	0.0122	0.0100	0.0029
6	0.90	-0.0302	-0.0022	0.0072	0.0028	0.0020
7	0.80	-0.0662	-0.0247	-0.0034	0.0028	0.0033
8	0.70	-0.0917	-0.0360	-0.0133	-0.0007	0.0018
9	0.60	-0.1084	-0.0468	-0.0180	-0.0063	0.0002
10	0.50	-0.1207	-0.0496	-0.0226	-0.0088	-0.0004
11	0.40	-0.1236	-0.0515	-0.0241	-0.0104	-0.0015
12	0.30	-0.1243	-0.0544	-0.0270	-0.0122	-0.0031
13	0.20	-0.1193	-0.0518	-0.0291	-0.0124	-0.0029
14	0.10	-0.1064	-0.0517	-0.0277	-0.0180	-0.0016
15	0.00	-0.1158	-0.0560	-0.0300	-0.0157	-0.0031
16	-0.10	-0.1198	-0.0588	-0.0288	-0.0153	-0.0021
17	-0.20	-0.1114	-0.0647	-0.0290	-0.0186	-0.0006
18	-0.30	-0.1131	-0.0619	-0.0312	-0.0194	-0.0031
19	-0.40	-0.1093	-0.0621	-0.0330	-0.0190	-0.0025
20	-0.50	-0.1151	-0.0619	-0.0316	-0.0191	-0.0055
21	-0.60	-0.1132	-0.0562	-0.0319	-0.0193	-0.0031
22	-0.70	-0.0997	-0.0518	-0.0316	-0.0244	-0.0061
23	-0.80	-0.0962	-0.0548	-0.0333	-0.0247	-0.0101
24	-0.90	-0.0753	-0.0574	-0.0317	-0.0229	-0.0039
25	-1.00	-0.0460	-0.0564	-0.0428	-0.0173	-0.0193
26	-1.10	-0.1147	-0.1478	-0.0599	-0.0321	-0.0349
27	-1.20	-0.0890	-0.0998	-0.0978	-0.2672	-0.2096
28	-1.30	-0.0865	-0.0910	-0.0675	-0.0308	-0.0186

TABLE D.3.4
 ADVANCED HIGH PENETRATION
 Lobed Mixer (PT/PT_∞)
 Normalized Total Pressure Data
 Axial Location $\bar{X} = 0.05$

Y		0.0	-0.1	-0.2	-0.3	-0.4	-0.5
K	Z						
1	1.00	0.9987	0.9986	0.9981	0.9977	0.9977	0.9972
2	0.90	0.9987	0.9986	0.9984	0.9976	0.9977	0.9974
3	0.80	0.9991	0.9988	0.9984	0.9977	0.9982	0.9975
4	0.70	0.9989	0.9987	0.9984	0.9974	0.9969	0.9958
5	0.60	0.9050	0.8968	0.8851	0.8706	0.8480	0.8437
6	0.55	0.6994	0.6942	0.6894	0.6840	0.6646	0.6725
7	0.53	0.6593	0.6546	0.6495	0.6468	0.6300	0.6353
8	0.51	0.6199	0.6173	0.6145	0.6091	0.5975	0.6000
9	0.50	0.5079	0.4912	0.4953	0.5054	0.4537	0.4569
10	0.49	0.4329	0.4241	0.3937	0.4004	0.3815	0.3802
11	0.47	0.5887	0.5898	0.5692	0.5610	0.5639	0.5620
12	0.45	0.6774	0.6788	0.6630	0.6457	0.6417	0.6465
13	0.43	0.7121	0.7091	0.6956	0.6769	0.6664	0.6718
14	0.41	0.7381	0.7388	0.7183	0.7018	0.6954	0.7023
15	0.40	0.7668	0.7643	0.7451	0.7277	0.7230	0.7365
16	0.39	0.7973	0.7893	0.7701	0.7563	0.7529	0.7714
17	0.37	0.8991	0.8852	0.8666	0.8629	0.8784	0.9015
18	0.30	0.9868	0.9823	0.9787	0.9784	0.9802	0.9801
19	0.20	0.9962	0.9955	0.9932	0.9898	0.9857	0.9793
20	0.10	0.9965	0.9951	0.9927	0.9887	0.9839	0.9779
21	0.00	0.9961	0.9953	0.9923	0.9889	0.9840	0.9776

TABLE D.3.4 (Continued)

ADVANCED HIGH PENETRATION

Lobed Mixer ($P_T/P_{T\infty}$)

Normalized Total Pressure Data

Axial Location $\bar{X} = 0.05$

	Y	-0.6	-0.7	-0.8	-0.9	-1.0	-1.1
K	Z						
1	1.00	0.9980	0.9826	0.9186	0.8438	0.7621	0.6152
2	0.90	0.9985	0.9850	0.9306	0.8678	0.7982	0.6466
3	0.80	0.9983	0.9882	0.9460	0.8956	0.8212	0.6246
4	0.70	0.9944	0.9771	0.9369	0.8684	0.7338	0.5229
5	0.60	0.8608	0.7765	0.7318	0.6543	0.5186	0.8779
6	0.55	0.6936	0.6189	0.5891	0.4271	0.7953	0.9528
7	0.53	0.6542	0.5881	0.5594	0.3361	0.8719	0.9586
8	0.51	0.6207	0.5586	0.4616	0.5633	0.9233	0.9587
9	0.50	0.4352	0.3777	0.3772	0.7214	0.9376	0.9551
10	0.49	0.4292	0.4726	0.5828	0.7829	0.9525	0.9544
11	0.47	0.5902	0.6285	0.6736	0.8222	0.9636	0.9478
12	0.45	0.6638	0.6977	0.7340	0.8663	0.9642	0.9387
13	0.43	0.6938	0.7326	0.7949	0.8978	0.9597	0.9306
14	0.41	0.7311	0.7767	0.8370	0.9239	0.9549	0.9200
15	0.40	0.7671	0.8160	0.8727	0.9419	0.9473	0.9153
16	0.39	0.8079	0.8561	0.9040	0.9527	0.9470	0.9084
17	0.37	0.9325	0.9534	0.9667	0.9651	0.9403	0.9039
18	0.30	0.9800	0.9733	0.9606	0.9417	0.9141	0.8775
19	0.20	0.9744	0.9617	0.9470	0.9217	0.8911	0.8492
20	0.10	0.9695	0.9550	0.9384	0.9121	0.8808	0.8365
21	0.00	0.9696	0.9580	0.9401	0.9120	0.8784	0.8385

TABLE D.3.4 (Continued)

ADVANCED HIGH PENETRATION

Lobed Mixer (PT/PT_∞)

Normalized Total Pressure Data

Axial Location $\bar{X} = 0.05$

	Y	0.00	0.10	0.20	0.30	0.40	0.50
K	Z						
1	0.00	0.9964	0.9973	0.9978	0.9982	1.0003	1.0135
2	0.10	0.9967	0.9974	0.9976	0.9989	0.9997	1.0126
3	0.20	0.9966	0.9977	0.9985	0.9993	0.9995	1.0119
4	0.30	0.9879	0.9952	0.9976	0.9986	0.9989	1.0121
5	0.35	0.9718	0.9835	0.9905	0.9886	0.9894	0.9978
6	0.38	0.9425	0.9494	0.9521	0.9462	0.9474	0.9505
7	0.40	0.9002	0.8887	0.8927	0.8890	0.8911	0.8921
8	0.41	0.8810	0.8697	0.8805	0.8768	0.8783	0.8814
9	0.42	0.8678	0.8550	0.8682	0.8650	0.8673	0.8695
10	0.43	0.8487	0.8305	0.8552	0.8521	0.8542	0.8561
11	0.44	0.7755	0.7875	0.8392	0.8385	0.8421	0.8434
12	0.45	0.7436	0.6686	0.7901	0.7836	0.8173	0.8220
13	0.46	0.7586	0.6901	0.7523	0.7588	0.7466	0.7507
14	0.47	0.8492	0.8262	0.7641	0.7654	0.7554	0.7461
15	0.48	0.8660	0.8433	0.8357	0.8375	0.8172	0.7827
16	0.49	0.8821	0.8638	0.8637	0.8624	0.8544	0.8493
17	0.50	0.8994	0.8764	0.8829	0.8824	0.8766	0.8766
18	0.55	0.9764	0.9630	0.9716	0.9729	0.9713	0.9865
19	0.60	0.9981	0.9977	0.9997	0.9989	0.9983	1.0118
20	0.70	0.9971	0.9981	1.0000	0.9991	0.9997	1.0117
21	0.80	0.9974	0.9987	1.0002	0.9989	0.9990	1.0123
22	0.90	0.9978	0.9990	1.0008	0.9993	0.9982	1.0121
23	1.00	0.9974	0.9992	1.0008	0.9994	0.9986	1.0123

TABLE D.3.4 (Continued)

ADVANCED HIGH PENETRATION

Lobed Mixer (FT/PT_∞)

Normalized Total Pressure Data

Axial Location $\bar{x} = 0.05$

	Y	0.60	0.70	0.80	0.85	0.90	0.95
K	Z						
1	0.00	0.9988	0.9978	0.9904	0.9782	0.9615	0.9471
2	0.10	0.9988	0.9980	0.9898	0.9778	0.9593	0.9406
3	0.20	0.9979	0.9983	0.9936	0.9835	0.9686	0.9515
4	0.30	0.9977	0.9977	0.9943	0.9885	0.9738	0.9558
5	0.35	0.9827	0.9854	0.9792	0.9743	0.9557	0.9359
6	0.38	0.9399	0.9468	0.9436	0.9405	0.9197	0.9015
7	0.40	0.8880	0.8972	0.8976	0.8962	0.8756	0.8560
8	0.41	0.8761	0.8877	0.8870	0.8852	0.8655	0.8369
9	0.42	0.8677	0.8760	0.8765	0.8749	0.8545	0.7532
10	0.43	0.8569	0.8656	0.8646	0.8629	0.8333	0.7423
11	0.44	0.8468	0.8544	0.8524	0.8480	0.7362	0.7875
12	0.45	0.8328	0.8383	0.8206	0.7807	0.7381	0.8855
13	0.46	0.7630	0.7808	0.7599	0.7604	0.8117	0.9111
14	0.47	0.7312	0.7616	0.7752	0.7907	0.8966	0.9372
15	0.48	0.7614	0.7810	0.8555	0.8812	0.9188	0.9597
16	0.49	0.8580	0.8586	0.8984	0.9163	0.9404	0.9769
17	0.50	0.8805	0.8929	0.9262	0.9417	0.9609	0.9881
18	0.55	0.9746	0.9884	0.9984	0.9989	0.9976	0.9985
19	0.60	0.9961	0.9989	0.9990	0.9996	0.9973	0.9986
20	0.70	0.9959	0.9994	0.9999	0.9999	0.9979	0.9986
21	0.80	0.9957	0.9988	1.0000	1.0010	0.9972	0.9985
22	0.90	0.9956	0.9987	0.9999	1.0008	0.9977	0.9980
23	1.00	0.9959	0.9988	1.0001	1.0006	0.9973	0.9984

TABLE D.3.4 (Continued)

ADVANCED HIGH PENETRATION

Lobed Mixer (PT/PT_∞)

Normalized Total Pressure Data

Axial Location $\bar{X} = 0.05$

	Y	1.00	1.05
K	Z		
1	0.00	0.9322	0.9181
2	0.10	0.9208	0.8982
3	0.20	0.9326	0.9093
4	0.30	0.9333	0.9038
5	0.35	0.9108	0.8774
6	0.38	0.8762	0.8574
7	0.40	0.8657	0.7498
8	0.41	0.8539	0.7302
9	0.42	0.8400	0.7501
10	0.43	0.7581	0.8677
11	0.44	0.7374	0.9029
12	0.45	0.7554	0.9241
13	0.46	0.8643	0.9456
14	0.47	0.9044	0.9635
15	0.48	0.9242	0.9790
16	0.49	0.9503	0.9882
17	0.50	0.9673	0.9958
18	0.55	0.9830	1.0001
19	0.60	0.9982	0.9997
20	0.70	0.9983	0.9998
21	0.80	0.9984	0.9996
22	0.90	0.9980	1.0003
23	1.00	0.9987	1.0000

TABLE D.4
 SINUSOIDAL LOBE MIXERS
 LOBE TRAILING EDGE BOUNDARY LAYER

LOW PENETRATION

I	CREST OUTER		CREST INNER		
	Z = 0.0	Y = 0.5	I	Z = 0.0	Y = 0.5
	NORMAL	U / U _∞		NORMAL	U / U _∞
1	0.02	0.327	1	0.03	0.625
2	0.04	0.417	2	0.08	0.703
3	0.07	0.814	3	0.18	0.822
4	0.12	0.968	4	0.28	0.899
5	0.15	0.982	5	0.38	0.956
6	0.200	0.999	6	0.48	0.990
			7	0.58	0.996
			8	0.68	0.997
			9	0.78	0.997
			10	0.88	0.999
			11	0.98	1.000

PARAMETER	INLET	FLAT PLATE EXIT	CREST EXIT OUTER LOW	CREST EXIT INNER LOW
δ^{*+}	= 0.024		= 0.04	= 0.0867
θ	= 0.017		= 0.021	= 0.0587
H	= 1.41		= 2.29	= 1.48
δ	= 0.145		= 0.15	= 0.48

TABLE D.4 (Continued)
 SINUSOIDAL LOBED MIXERS
 LOBE TRAILING EDGE BOUNDARY LAYER

HIGH PENETRATION

	CREST OUTER		CREST INNER		
	Z = 0.0	Y = 2.0	Z = 0.0	Y = 2.0	
	NORMAL	U / U _∞	NORMAL	U / U _∞	
I			I		
1	0.025	0.650	1	0.05	0.466
2	0.050	0.800	2	0.10	0.531
3	0.075	0.940	3	0.20	0.627
4	0.100	0.982	4	0.30	0.711
5	0.125	0.990	5	0.40	0.753
			6	0.50	0.811
			7	0.60	0.865
			8	0.70	0.908
			9	0.80	0.955
			10	0.90	0.974
			11	1.00	0.979
			12	1.10	0.982
			13	1.30	0.986
			14	1.50	0.994
			15	1.70	1.000

PARAMETER	INLET	FLAT PLATE EXIT	CREST EXIT OUTER HIGH	CREST EXIT INNER HIGH
δ^*	= 0.039		= 0.0280	= 0.235
θ	= 0.028		= 0.0146	= 0.148
H	= 1.39		= 1.92	= 1.59
δ	= 0.240		= 0.125	= 1.40

TABLE D.4 (Continued)
 ADVANCED HIGH PENETRATION MIXER
 TRAILING EDGE BOUNDARY LAYER

1 OUT			2 OUT			3 OUT		
Z = 0.0 Y = 1.22			Z = 0.053 Y = 0.75			Z = 0.053 Y = 0.0		
I	NORMAL	PT/PT _∞	I	NORMAL	PT/PT _∞	I	NORMAL	PT/PT _∞
1	0.010	0.578	1	0.010	0.562	1	0.010	0.603
2	0.016	0.702	2	0.015	0.630	2	0.020	0.665
3	0.020	0.752	3	0.020	0.681	3	0.030	0.738
4	0.024	0.795	4	0.026	0.732	4	0.040	0.792
5	0.028	0.835	5	0.030	0.767	5	0.050	0.840
6	0.034	0.891	6	0.036	0.809	6	0.060	0.885
7	0.042	0.950	7	0.040	0.848	7	0.070	0.926
8	0.050	0.984	8	0.046	0.884	8	0.080	0.957
9	0.058	0.997	9	0.050	0.916	9	0.090	0.980
10	0.066	1.000	10	0.056	0.944	10	0.100	0.992
			11	0.060	0.964	11	0.110	0.996
			12	0.070	0.991	12	0.160	1.000
			13	0.080	1.000			
δ*	=	0.0098		=	0.0118		=	0.0138
θ	=	0.0055		=	0.0071		=	0.0091
H	=	1.78		=	1.65		=	1.52
δ	=	0.049		=	0.056		=	0.090

4 OUT			5 OUT			6 OUT		
Z = 0.053 Y = -0.75			Z = 1.000 Y = -1.22			Z = 0.000 Y = 1.59		
I	NORMAL	PT/PT _∞	I	NORMAL	PT/PT _∞	I	NORMAL	PT/PT _∞
1	0.010	0.500	1	0.010	0.339	1	0.010	0.548
2	0.020	0.582	2	0.030	0.455	2	0.020	0.626
3	0.030	0.626	3	0.050	0.517	3	0.030	0.684
4	0.050	0.700	4	0.070	0.566	4	0.042	0.743
5	0.070	0.775	5	0.090	0.610	5	0.050	0.772
6	0.110	0.890	6	0.110	0.651	6	0.062	0.822
7	0.160	0.964	7	0.130	0.686	7	0.070	0.846
8	0.210	0.989	8	0.150	0.719	8	0.080	0.872
9	0.260	0.984	9	0.170	0.745	9	0.090	0.893
10	0.310	0.976	10	0.190	0.779	10	0.100	0.919
11	0.360	0.969	11	0.210	0.787	11	0.110	0.933
12	0.410	0.960	12	0.260	0.828	12	0.150	0.982
13	0.450	0.951	13	0.310	0.866	13	0.190	0.999
			14	0.410	0.940			
			15	0.510	0.993			
			16	0.610	1.000			
δ*	=	0.0283		=	0.0652		=	0.0187
θ	=	0.0214		=	0.0489		=	0.0130
H	=	1.32		=	1.33		=	1.44
δ	=	(undefined)		=	0.475		=	0.150

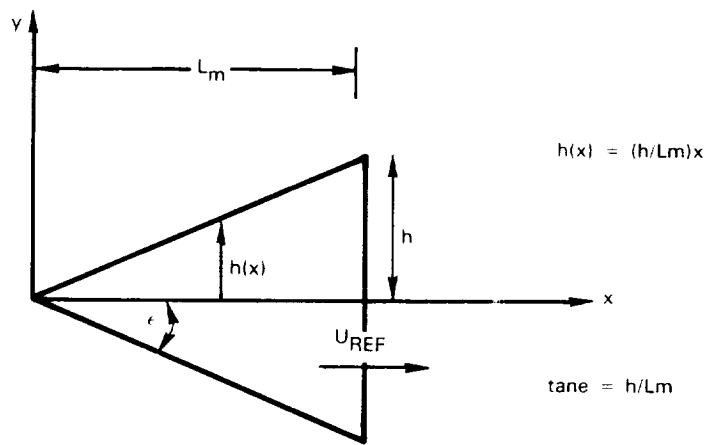
TABLE D.4 (Continued)
 ADVANCED HIGH PENETRATION MIXER
 TRAILING EDGE BOUNDARY LAYER

1 IN			2 IN			3 IN		
z = 0.0 y = 1.16			z = 0.47 y = 0.69			z = 0.47 y = 0.0		
I	NORMAL	PT/PT _∞	I	NORMAL	PT/PT _∞	I	NORMAL	PT/PT _∞
1	0.010	0.590	1	0.010	0.543	1	0.010	0.510
2	0.030	0.617	2	0.030	0.638	2	0.020	0.651
3	0.050	0.644	3	0.050	0.697	3	0.030	0.707
4	0.070	0.669	4	0.070	0.748	4	0.050	0.787
5	0.090	0.689	5	0.090	0.797	5	0.070	0.850
6	0.110	0.743	6	0.110	0.841	6	0.100	0.917
7	0.130	0.755	7	0.160	0.931	7	0.110	0.936
8	0.150	0.789	8	0.210	0.987	8	0.160	0.982
9	0.170	0.808	9	0.260	0.998	9	0.210	0.996
10	0.190	0.837	10	0.310	1.000	10	0.260	0.999
11	0.210	0.860						
12	0.310	0.968						
13	0.410	1.000						
δ*	= 0.0411			= 0.0262			= 0.0190	
θ	= 0.0322			= 0.0193			= 0.0131	
H	= 1.28			= 1.36			= 1.45	
δ	= 0.348			= 0.203			= 0.161	

4 IN			5 IN			6 IN		
z = 0.47 y = -0.75			z = 1.000 y = -1.28			z = 1.000 y = -1.47		
I	NORMAL	PT/PT _∞	I	NORMAL	PT/PT _∞	I	NORMAL	PT/PT _∞
1	0.010	0.609	1	0.010	0.370	1	0.010	0.484
2	0.020	0.720	2	0.020	0.402	2	0.020	0.657
3	0.026	0.776	3	0.030	0.463	3	0.030	0.744
4	0.030	0.808	4	0.042	0.563	4	0.042	0.808
5	0.040	0.869	5	0.050	0.639	5	0.054	0.850
6	0.050	0.917	6	0.062	0.772	6	0.062	0.875
7	0.060	0.947	7	0.070	0.853	7	0.070	0.899
8	0.070	0.971	8	0.080	0.936	8	0.080	0.921
9	0.080	0.983	9	0.090	0.982	9	0.090	0.945
10	0.090	0.991	10	0.100	0.999	10	0.100	0.963
11	0.100	0.998				11	0.110	0.978
12	0.110	1.000				12	0.130	0.997
δ*	= 0.0113			= 0.0229			= 0.0147	
θ	= 0.0070			= 0.0137			= 0.0092	
H	= 1.61			= 1.67			= 1.60	
δ	= 0.078			= 0.090			= 0.112	

APPENDIX E
APPROXIMATE ANALYSIS

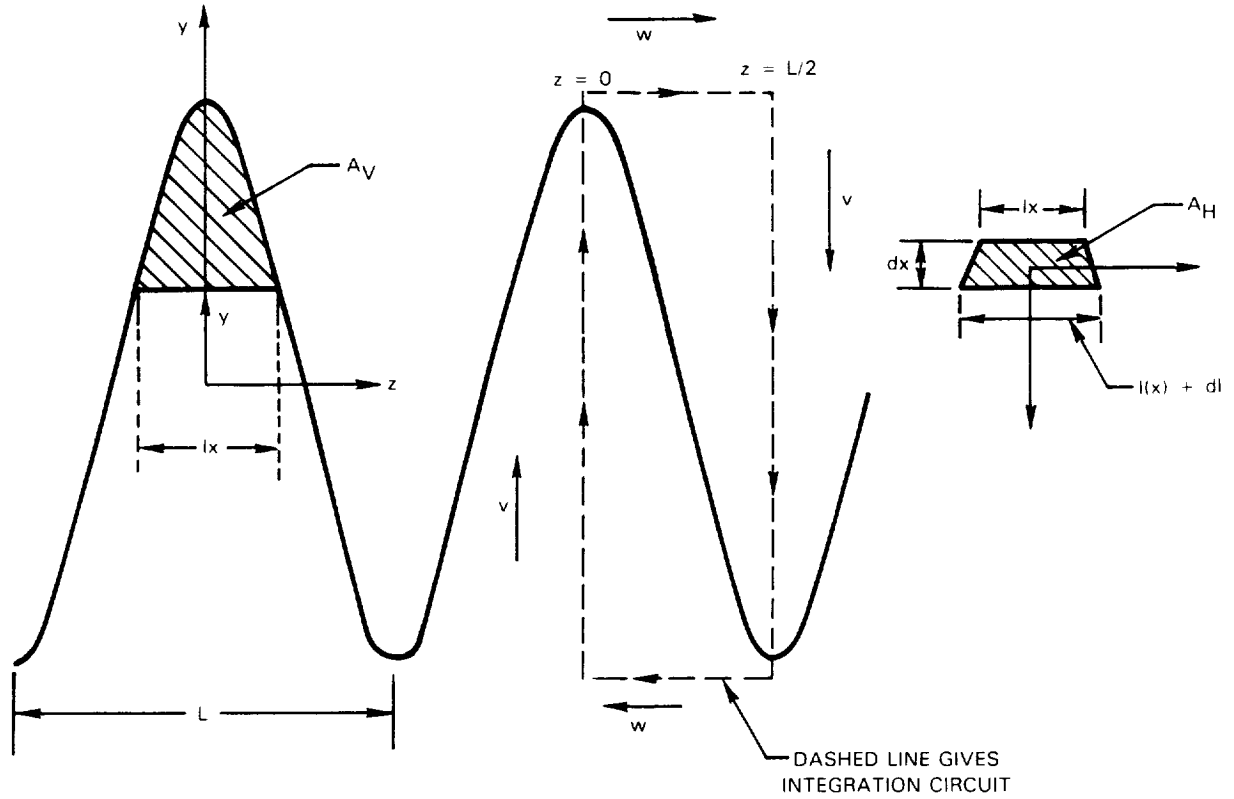
This appendix describes an approximate, one-dimensional inviscid analysis for calculating exit plane transverse velocity components and circulation for straight-ramped lobes, such as sketched below:



where U_{REF} is the lobe exit plane axial velocity component, $H(x)$ is the lobe peak height, L_m is lobe length and ϵ is the ramp angle.

The sketch below shows a cross-hatched area A_v which is the area in a vertical plane ($x=\text{constant}$) bounded on the top by the lobe contour and on the bottom by the line $y=\text{constant}$. Since this area increases with axial distance, the mass flux passing through this region also increases with x . To the right is a second cross-hatched area A_h which is the area in a horizontal plane ($y=\text{constant}$) defined by the intersection of the lobe contour with the plane. By continuity, the vertical velocity component mass flux through this plane is equal to the increase in axial component mass flux in the distance dx , or:

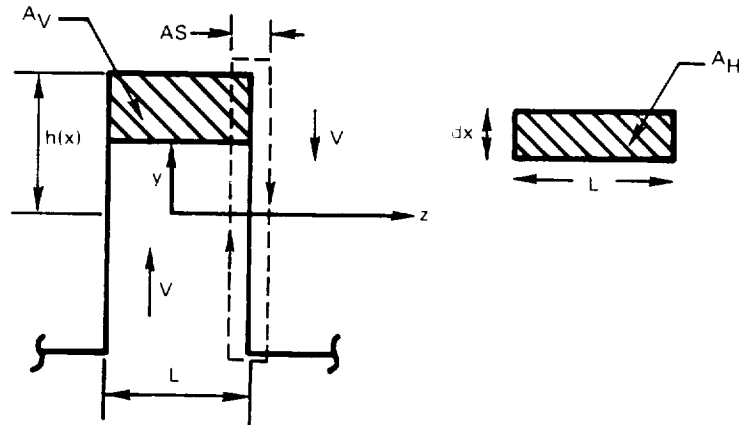
$$V \frac{dA_H}{dx} = U_{REF} \frac{dA_V}{dx} \quad (E.1)$$



constant density conditions. Since U_{REF} is known and the areas are functions of lobe waveform, y and x , the vertical velocity component can be determined as a function of x and y and lobe shape.

In the following, the exit plane velocity was calculated as well as the contribution of this component to circulation, Γ . As sketched above, the circulation path includes both vertical and horizontal legs. The present analysis cannot treat the horizontal leg contribution, however, the section titled "Circulation Calculations" in the main text shows this contribution is negligibly small for large amplitude mixer lobes. Calculations are performed for rectangular lobes, parallel sided lobes with peak regiond rounds, triangular lobes and sinusoidal lobes.

Rectangular Lobes - Referring to the sketch below which shows the geometrical parameters and circulation integration path (shown dashed), the areas, transverse velocity and circulation are given by:



$$\frac{dA_V}{dx} = b \frac{dh}{dx} = \frac{bh}{Lm} \quad (E.2)$$

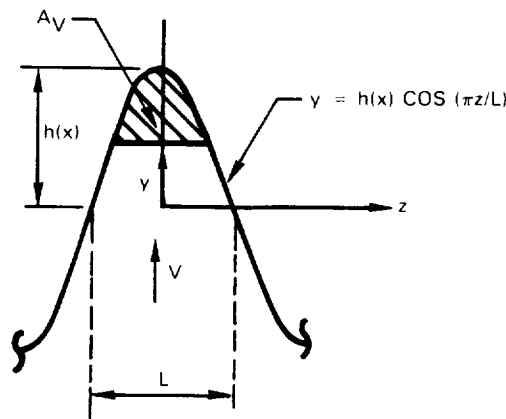
$$\frac{dA_H}{dx} = L \quad (E.3)$$

$$V = \frac{U_{REF} h}{Lm} \quad (E.4)$$

$$\Gamma = 2 \int_{-h}^{+h} V dy + \lim_{\Delta S \rightarrow 0} 2 W \Delta S = \frac{4 U_{REF} h^2}{Lm} \quad (E.5)$$

Since the spanwise component, W , is finite, the horizontal leg contribution for this lobe is zero. Vertical component magnitude within the lobe is constant and directly dependent on the amplitude-to-length ratio (tangent of the ramp angle ϵ). Circulation is dependent on the second power of lobe amplitude.

Sinusoidal Lobes - Similar quantities for a sinusoidal lobe geometry are given below:



$$\frac{dA_v}{dx} = \frac{2L}{\pi} \frac{dh}{dx} \frac{h^2 - y^2}{h} \quad (E.6)$$

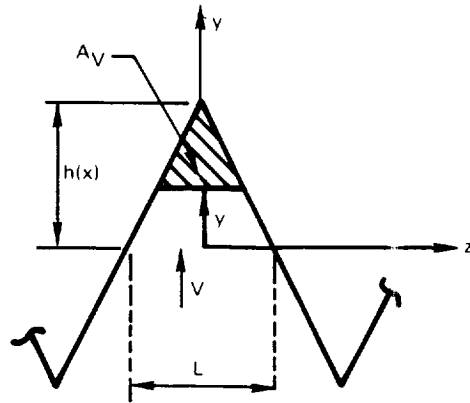
$$\frac{dA_H}{dx} = \frac{2L}{\pi} \cos^{-1}(y/h) \quad (E.7)$$

$$V = \frac{U_{REF} h}{L} \frac{\sqrt{1 - (y/h)^2}}{\cos^{-1}(y/h)} \quad (E.8)$$

$$\Gamma = \frac{2.46 U_{REF} h^2}{L} \quad (E.9)$$

This calculation neglects the horizontal leg contribution to Γ .

Triangular lobes -- Triangular results are:




$$\frac{dA_V}{dx} = \frac{L}{2h} \frac{dh}{dx} \left[(h-y) \left(1 + \frac{y}{h} \right) \right] \quad (\text{E.10})$$

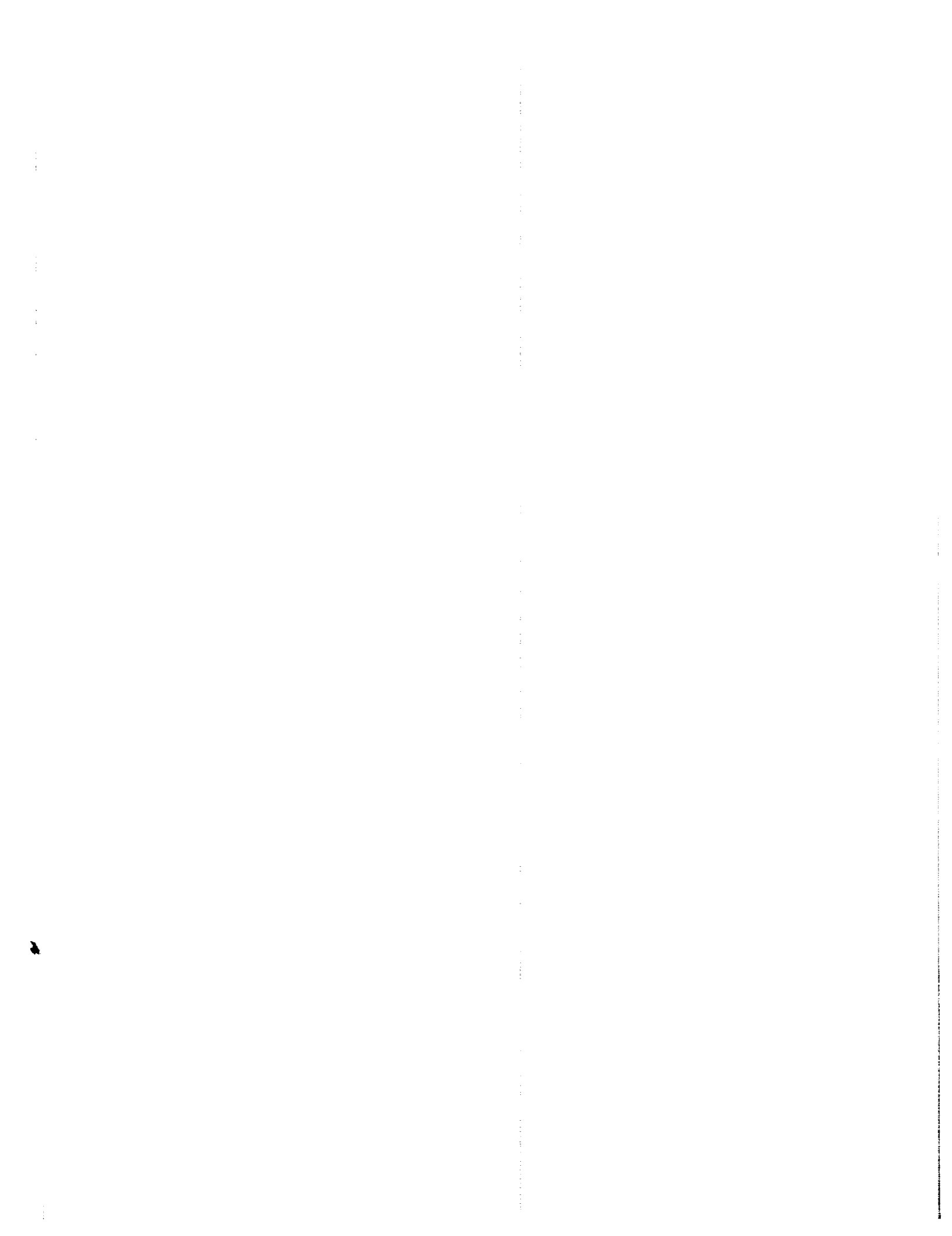
$$\frac{dA}{dx} = \frac{L}{h} (h-y) \quad (\text{E.11})$$

$$V = \frac{U_{REF}^2}{2L} \left(1 + \frac{y}{h} \right) \quad (\text{E.12})$$

$$\Gamma = \frac{2 U_{REF}^2}{L} \quad (\text{E.13})$$

This calculation neglects the horizontal leg contributions to Γ .

		Report Documentation Page	
1. Report No. NASA CR-4147		2. Government Accession No.	3. Recipient's Catalog No.
4. Title and Subtitle Turbofan Forced Mixer Lobe Flow Modeling I - Experimental and Analytical Assessment		5. Report Date October 1988	
		6. Performing Organization Code	
7. Author(s) T. Barber, R.W. Paterson, and S.A. Skebe		8. Performing Organization Report No. None (E-4083)	
		10. Work Unit No. 505-62-21	
9. Performing Organization Name and Address United Technologies Corporation Pratt & Whitney Engineering Division East Hartford, Connecticut		11. Contract or Grant No. NAS3-23039	
		13. Type of Report and Period Covered Contractor Report Final	
12. Sponsoring Agency Name and Address National Aeronautics and Space Administration Lewis Research Center Cleveland, Ohio 44135-3191		14. Sponsoring Agency Code	
		15. Supplementary Notes Project Manager, Allan R. Bishop, Internal Fluid Mechanics Division, NASA Lewis Research Center.	
16. Abstract This report describes a joint analytical and experimental investigation of three-dimensional flowfield development within the lobe region of turbofan forced mixer nozzles. The objective of the current study was to develop a method for predicting the lobe exit flowfield. In the analytical approach, a linearized inviscid aerodynamic theory was used for representing the axial and secondary flows within the three-dimensional convoluted mixer lobes and three-dimensional boundary layer analysis was applied thereafter to account for viscous effects. The experimental phase of the program employed three planar mixer lobe models having different waveform shapes and lobe heights for which detailed measurements were made of the three-dimensional velocity field and total pressure field at the lobe exit plane. Velocity data was obtained using Laser Doppler Velocimetry (LDV) and total pressure probing and hot wire anemometry were employed to define exit plane total pressure and boundary layer development. Comparison of data and analysis was performed to assess analytical model prediction accuracy. As a result of this study both a planar mixer geometry inverse analysis (PLANMIX) and a more general (planar or axisymmetric) direct analysis have been developed. A principal conclusion resulting from this study is that the global mixer lobe flowfield is inviscid and can be predicted from an inviscid analysis and Kutta condition.			
17. Key Words (Suggested by Author(s)) Mixers Lobe flow modeling Three-dimensional flows		18. Distribution Statement Unclassified - Unlimited Subject Category 02	
19. Security Classif. (of this report) Unclassified	20. Security Classif. (of this page) Unclassified	21. No of pages 156	22. Price* A08



Aeronautics and
Administration
Washington, D.C.

**SPECIAL FOURTH-CLASS RATE
POSTAGE & FEES PAID
NASA
Permit No. G-27**



**POSTMASTER: If Undeliverable (Section 158
Postal Manual) Do Not Return**
